



Searches for Di-Higgs Production in the $b\bar{b}\gamma\gamma$ Final State with the CMS Run-2 Dataset

Rafael Teixeira de Lima

Northeastern University

Boston - Massachusetts

A thesis submitted for the degree of

Doctor of Philosophy

April, 2017

This thesis is dedicated to
someone
for some special reason

Acknowledgements

plenty of waffle, plenty of waffle.

Abstract

plenty of waffle, plenty of waffle.

Contents

1	Introduction	1
1.1	The Standard Model of Particle Physics	1
1.2	The Electroweak Theory of Glashow-Weinberg-Salam	2
1.2.1	Spontaneous Symmetry Breaking and Mass Generation	3
1.2.2	Fermion Masses	6
1.3	Higgs Boson Phenomenology	7
1.4	Higgs Physics Current Status	8
1.5	Higgs as a Probe of New Physics	10
2	The Large Hadron Collider and the Compact Muon Solenoid Experiment	14
2.1	The LHC Accelerator Complex	14
2.2	The CMS Experiment	14
2.2.1	The CMS Tracking Detectors	14
2.2.2	The CMS Calorimetry Detectors	14
2.2.3	The CMS Muon Detectors	14
2.2.4	The CMS Trigger and Data Acquisition Systems	14
2.2.5	Object Reconstruction at CMS	14
3	The CMS Electromagnetic Calorimeter	15
3.1	PbWO ₄ Crystals and In-detector Electronics	16
3.2	Trigger and Data Acquisition Systems	18
3.2.1	Data Flow	18
3.2.2	Timing and Control Distribution	20
3.2.3	Software Architecture	21
3.3	Electron and Photon Energy Reconstruction	24
3.3.1	Online Reconstruction	24
3.3.2	Response Monitoring	25

3.3.3	Intercalibration	27
3.3.4	Absolute Calibration	28
3.3.5	High Level Calibrations	29
3.4	ECAL Energy Resolution	29
3.4.1	Energy Resolution of a Calorimeter	29
3.4.2	ECAL Energy Resolution with Run II data	30
3.5	The CMS ECAL Barrel Upgrade	32
3.5.1	The High Luminosity LHC	32
3.5.2	ECAL Electronics Upgrade	32
4	Higgs Exotic Decays with Photons and Missing Energy	35
4.1	Introduction	35
4.2	Event selection	36
4.3	Background estimation	40
4.3.1	Background estimates from MC simulation	41
4.3.2	Jets Identified as Photons Background	42
4.3.3	Electrons Identified as Photons Background	43
4.3.4	Non-collision background estimates from data	52
4.3.5	Background modeling validation	52
4.4	Systematic uncertainties	53
4.5	Results	54
4.5.1	Model-independent limits	54
4.5.2	Model-specific limits	56
4.6	Higgs Exotic Decays to Photons and MET Projection Studies	57
4.6.1	Introduction	57
4.6.2	Methodology	58
4.6.3	Results	63
5	HH searches with photons and b-jets at CMS Run 2	67
5.1	Introduction	67
5.1.1	Strategy Summary	68
5.2	Samples	69
5.2.1	Signal MC: resonant production	70
5.2.2	Signal MC: nonresonant production	70
5.2.3	Background MC	74
5.2.4	Data	75
5.3	Analysis objects and selection	75

5.3.1	Triggers And Pre-Selection	75
5.3.2	Photons	76
5.3.3	Jets	79
5.4	Categorization	82
5.4.1	MVA Categorization	85
5.5	\tilde{M}_X and Mass Window Selection	94
5.6	Selection Efficiencies	97
5.7	Control Plots	103
5.8	Statistical Modeling and Limit Extraction	106
5.8.1	Signal Model	106
5.8.2	Background Model	108
5.8.3	Single Higgs Background Modeling	116
5.9	Systematics	122
5.9.1	Signal shape smearings	123
5.10	Results	125
5.11	BSM Nonresonant Results	128
5.12	Summary	131
6	Conclusions	132

Chapter 1

Introduction

1.1 The Standard Model of Particle Physics

The Standard Model of particles and fields (SM) describes the most basic constituents of matter and their dynamics, as currently known. It is built upon the hypothesis that fundamental, point-like particles exist (fermions) and that their interactions, via bosonic fields, can be described in a quantum field theoretical framework. Fundamental interactions are described in the SM by the gauge invariance principle, meaning that interactions will appear in the framework as gauge fields after when imposing local and continuous (gauge) symmetries. An early example of this principle is the emergence of electromagnetism on the Schrödinger equation by imposing a local and continuous $U(1)$ symmetry.

As of today, the SM described three types of interactions:

The Strong Interaction Also known as quantum chromodynamics or QCD. It appears in the SM via an $SU(3)$ gauge symmetry. This gauge group implies the existence of 8 gauge bosons, called gluons. Fermions particles that interact via QCD are called **quarks**, and are organized in triplets of a "color" charge. Fermions that do not interact via QCD are called **leptons**.

The Electromagnetic Interaction It appears in the SM via an $U(1)$ gauge symmetry, with one gauge boson associated to it (photon). The particles that interact via the electromagnetic interaction have electric charge.

The Weak Interaction Appears in the SM via an $SU(2)$ gauge symmetry. It has three different gauge bosons associated to it, two have electric charge: W^+ and W^- , while one is neutral: Z^0 . The weak interaction charge is commonly called weak hypercharge.

The two last interactions have been further combined in a single theoretical model, called the electroweak interaction [?, ?, ?]. It is based on the fact that, before a spontaneous symmetry breaking occurs, both interactions can be described by a single gauge group, namely $SU(2) \otimes U(1)$. A main ingredient of this unification process is the spontaneous symmetry breaking mechanism based on the Higgs field [?, ?, ?].

The field content of the SM was completed with the observation that both quarks and leptons are organized into three generations. The first generation of leptons contains the electron (e) and the electron neutrino (ν_e), while the first generation of quarks contains the up quark (u) and the down quark (d). The second generation of leptons contains the muon (μ) and the mu neutrino (ν_μ), while the second generation of quarks contains the charm quark (c) and the strange quark (s). The third generation of leptons contains the tau (τ) and the tau neutrino (ν_τ), while the third generation of quarks contains the top quark (t) and the bottom quark (b). The generation structure is particularly important by noting that particles of the same family, with left-handed chirality, form a weak isospin doublet, while the right-handed fermions are weak singlets:

$$L_l = \begin{pmatrix} \nu_e \\ e \end{pmatrix}_L, \quad \begin{pmatrix} \nu_\mu \\ \mu \end{pmatrix}_L, \quad \begin{pmatrix} \nu_\tau \\ \tau \end{pmatrix}_L; \quad (1.1)$$

$$L_q = \begin{pmatrix} u \\ d \end{pmatrix}_L, \quad \begin{pmatrix} c \\ s \end{pmatrix}_L, \quad \begin{pmatrix} t \\ b \end{pmatrix}_L;$$

$$R_l = e_R, \mu_R, \tau_R; \quad R_q = u_R, d_R, c_R, s_R, t_R, b_R. \quad (1.2)$$

1.2 The Electroweak Theory of Glashow-Weinberg-Salam

Through observations that date back to the early XX century, the electroweak interactions were built upon a set of experimental fundaments:

Universality The weak interactions are blind with respect to quarks and leptons generations. This means that the coupling strength is the same to any of the three families described previously.

Massless and Left-Handed Neutrinos For the energy regime to which the SM addresses, the neutrinos are idealized as massless (even though experiments have proved that they do have mass, even if below eV scale), and they only exist (or only interact with the SM) in their left-handed chirality.

Chirality The electroweak interactions are not chiral, i.e., the structure of the theory should treat right-handed and left-handed particles differently.

Mixing The electroweak eigenstates of quarks is not the same as their mass eigenstates. Therefore, the electroweak interaction acts on mixed states of quarks mass eigenstates. This quark mixing is described by the CKM matrix.

The unified electroweak theory is based on the $SU(2)_L \otimes U(1)_Y$ gauge group. The indices L and Y address the fact that the $SU(2)$ gauge bosons (\vec{B}_μ) will only act upon left-handed particles, while the $U(1)$ gauge boson (A_μ) will couple to particles that contain weak hypercharge. After the spontaneous symmetry breaking, these four gauge bosons will become the three weak bosons and the photon. We can write a lagrangean, symmetric under this gauge group, as:

$$\begin{aligned}\mathcal{L}_{GWS} &= \mathcal{L}_{Fermions} + \mathcal{L}_{Gauge} \\ &= \left\{ \bar{R}i\gamma^\mu \left(\partial_\mu + i\frac{a}{2}A_\mu Y \right) R + \bar{L}i\gamma^\mu \left(\partial_\mu + i\frac{a}{2}A_\mu Y + i\frac{b}{2}\vec{\sigma} \cdot \vec{B}_\mu \right) L \right\} (1.3) \\ &\quad - \frac{1}{4} \left\{ F_{\mu\nu}^M F_M^{\mu\nu} + f_{\mu\nu} f^{\mu\nu} \right\},\end{aligned}$$

where R and L represents the right-handed and left-handed fermions, respectively; a and b represents the coupling constants of the model; γ and σ represent the Dirac and Pauli matrices, respectively; and F and f are the field strengths tensors of the electroweak bosons.

1.2.1 Spontaneous Symmetry Breaking and Mass Generation

One important detail of the lagrangean in Equation 1.3 is the fact that mass terms to the electroweak bosons are forbidden by gauge invariance. Particularly, classical mass terms such as $m_B^2 \vec{B}_\mu \cdot \vec{B}^\mu$ violate the model's gauge symmetry given that \vec{B}_μ transforms as:

$$B_\mu^M \rightarrow B_\mu^M + \frac{1}{b} \partial_\mu \alpha^M(x) + \epsilon_{NO}^M B_\mu^N B_\mu^O. \quad (1.4)$$

The Higgs mechanism is the way the SM generates these mass terms while keeping the gauge invariance intact. In its non-Abelian form, it adds an $SU(2)_L$ scalar doublet field Φ and a quartic potential $V(\Phi)$ to the SM lagrangean described previously:

$$\Phi = \begin{pmatrix} \phi^+ \\ \phi^0 \end{pmatrix}, \quad (1.5)$$

$$V(\Phi) = \mu^2 \Phi^\dagger \Phi + \lambda (\Phi^\dagger \Phi)^2, \quad (1.6)$$

with ϕ^+ e ϕ^0 as complex scalar fields.

As a doublet, the covariant derivative that acts upon Φ is similar to the one that acts on left-handed leptons:

$$D_\mu = \partial_\mu + i\frac{a}{2}A_\mu Y + i\frac{b}{2}\vec{\sigma} \cdot \vec{B}_\mu. \quad (1.7)$$

Therefore, we can write the final SM lagrangean, including the Higgs mechanism, as:

$$\mathcal{L}_{Higgs+GSW} = (D\Phi)^\dagger (D\Phi) + \mu^2 \Phi^\dagger \Phi + \lambda (\Phi^\dagger \Phi)^2 + \mathcal{L}_{GSW}. \quad (1.8)$$

The shape of $V(\Phi)$ depends on the values of μ and λ . Therefore, we can place bounds on these parameters based on the role $V(\Phi)$ must perform. First, $V(\Phi)$ must not have a global minimum at $|\Phi| \rightarrow \infty$, which means $\lambda > 0$. Second, in order to properly generate the gauge boson masses, the $V(\Phi)$ minimum must not be at zero. This is accomplished by setting $\mu^2 < 0$, which creates a $V(\Phi)$ minimum at $|\Phi| = \sqrt{-\frac{\mu^2}{\lambda}} \equiv v$, also known as the electroweak vacuum expectation value. The found vacuum is spherically symmetric, meaning it remains unchanged by rotations such as $\Phi_{min} \rightarrow \exp\left(i\frac{\vec{\sigma}}{2} \cdot \vec{\xi}\right) \Phi_{min}$. With this fact, we can expand the Higgs field around its vacuum as:

$$\Phi \rightarrow \frac{1}{\sqrt{2}} \begin{pmatrix} 0 \\ v + H(x) \end{pmatrix}, \quad (1.9)$$

Writing this expression explicitly in the covariant derivative definition, calculating $(D\Phi)^\dagger (D\Phi)$ and gathering the terms involving the Higgs vacuum perturbation, we have:

$$\left[\frac{1}{4} (aA_\mu - bB_\mu^3)^2 + \frac{b^2}{4} (B_\mu^1 - iB_\mu^2)(B_\mu^1 + iB_\mu^2) \right] \left(\frac{1}{\sqrt{2}} (v + H(x)) \right)^2 \quad (1.10)$$

We can simplify this equation with the following redefinitions:

$$W_\mu^\pm = \frac{1}{\sqrt{2}} (B_\mu^1 \pm i B_\mu^2), \quad (1.11)$$

$$Z_\mu^0 = \frac{b B_\mu^3 - a A_\mu}{\sqrt{b^2 + a^2}}, \quad (1.12)$$

$$\mathcal{A}_\mu = \frac{b B_\mu^3 + a A_\mu}{\sqrt{b^2 + a^2}}. \quad (1.13)$$

Using these new field definitions, we can expand $(v + H(x))^2$ in equation 1.10 to obtain their couplings to the Higgs vacuum and the Higgs perturbation:

$$\begin{aligned} & \frac{v^2}{8} (b^2 + a^2) Z_\mu^0 Z^{0\mu} + \frac{v^2 b^2}{8} W_\mu^+ W^{-\mu} + \\ & \frac{v}{8} (b^2 + a^2) Z_\mu^0 Z^{0\mu} H(x) + \frac{vb^2}{8} W_\mu^+ W^{-\mu} H(x) + \\ & \frac{1}{8} (b^2 + a^2) Z_\mu^0 Z^{0\mu} H^2(x) + \frac{b^2}{8} W_\mu^+ W^{-\mu} H^2(x). \end{aligned} \quad (1.14)$$

The first two terms in the equation above are canonical mass terms to the Z^0 and W^\pm fields, but the field \mathcal{A} remains massless. This takes the model back exactly to standard views on the weak interactions, with one massive neutral boson and two massive charged bosons, and on the electromagnetic interaction, with one massless neutral boson. The mass of the Z^0 and W^\pm bosons can then be expressed based on the electroweak vacuum expectation value and on the electroweak couplings, the latter being well known experimentally, as: $m_W^2 = \frac{v^2 b^2}{4}$ and $m_Z^2 = \frac{v^2}{4} (b^2 + a^2)$. We can express v^2 as a function of m_W and related it to the Fermi coupling constant (G_F), such that $v = \sqrt{\frac{-\mu^2}{\lambda}} = (\sqrt{2} G_F)^{1/2} \approx 246 \text{ GeV}$ [?], where G_F is precisely obtained through muon lifetime measurements.

We can also investigate the shape of the Higgs potential after the vacuum has been fixed. Using the previous definition of v , we have:

$$V(\Phi) = \frac{-v\lambda}{2} (v + H(x))^2 + \frac{\lambda}{4} (v + H(x))^4 \quad (1.15)$$

$$= -\frac{\lambda v^4}{2} + \lambda v^2 H^2(x) + \lambda v H^3(x) + \frac{\lambda}{4} H^4(x). \quad (1.16)$$

The first important term in the equation above can be interpreted as a mass term for a scalar field. This means that perturbations on the Higgs field around the vacuum will be realized as a scalar boson, the Higgs boson, with mass equal to $m_H^2 = 2\lambda v^2$.

The following terms describe how the Higgs boson interacts with itself via tertiary and quartic couplings. It is interesting to note that the Higgs boson can be understood as an excitation on a transversal section of the original potential. The other degrees of freedom present in the theory, namely the longitudinal excitations along the direction in which the vacuum is symmetric, were "eaten" by the massless fields \vec{B} e A , as new degrees of freedom related to their masses.

1.2.2 Fermion Masses

In the previous section, the Higgs mechanism was used to break electroweak symmetry and give mass to three of the four gauge bosons present in the theory. However, the fermion sector of the theory also presents problems when dealing with canonical mass terms. Namely, knowing that left-handed and right-handed fermions are, respectively, doubles and singlets under the electroweak interaction, their gauge transformations will be different, and terms such as $m_f \bar{f} f = m_f (\bar{f}_L f_R + \bar{f}_R f_L)$ will break the gauge invariance.

However, we can note that terms such as $\bar{f}_L \Phi$ are an electroweak singlet and $\bar{f}_R \Phi^\dagger$ are a doublet (meaning that the Higgs interaction with fermions changes their chirality). Therefore, one can construct a new type of mass term based on fermionic Yukawa interactions with the Higgs field:

$$g_f [\bar{f}_L \Phi f_R + \bar{f}_R \Phi^\dagger f_L] \quad (1.17)$$

which preserves the $SU(2)$ gauge invariance.

Using the choice of vacuum from the previous section, we can write an example of this mass term applied to the bottom quark:

$$\mathcal{L}_{\text{Yukawa}} = g_b \left[\gamma^0 \begin{pmatrix} t_L^\dagger & b_L^\dagger \end{pmatrix} \frac{1}{\sqrt{2}} \begin{pmatrix} 0 \\ v + H(x) \end{pmatrix} b_R + \text{c.c.} \right] \quad (1.18)$$

$$= \frac{g_b}{\sqrt{2}} (\bar{b}_L b_R + \bar{b}_R b_L) \left(1 + \frac{H(x)}{v} \right) \quad (1.19)$$

$$= \frac{g_b v}{\sqrt{2}} \bar{b} b + \frac{g_b}{\sqrt{2}} \bar{b} b H(x). \quad (1.20)$$

The first term in the last step of the equation above is a canonical term for the b quark mass, while the second term dictates the b quark coupling to the Higgs boson.

In order to give mass also to the top quark, we must use the charge conjugate to the Higgs doublet:

$$\Phi^c = i\sigma^2 \Phi^* = \frac{1}{\sqrt{2}} \begin{pmatrix} v + H(x) \\ 0 \end{pmatrix}, \quad (1.21)$$

which rotates the original Higgs doublet preserving the vacuum symmetry.

The same mechanism can be applied to the leptons. However, due to the non-existence of right-handed neutrinos, it cannot be applied to give mass to the left-handed neutrinos. As of today, we know neutrinos indeed have mass, albeit small, and specific mechanisms have been developed to address this issue. But, given that the neutrino masses are several orders of magnitude smaller than the characteristic scale of the electroweak interactions (vacuum expectation value), the approximation that the neutrinos are massless is well justified.

1.3 Higgs Boson Phenomenology

An important aspect of the Higgs mechanism is the prediction of a new mass eigenstate, the Higgs boson, with couplings to fermions and electroweak bosons completely defined by the model. The only free parameter present is the Higgs boson mass, $m_H^2 = 2\lambda v^2$, that dictates both the branching fraction of the Higgs decays, and its cross section at colliders. These two quantities, as a function of the Higgs mass, can be seen in Figure 1.1.

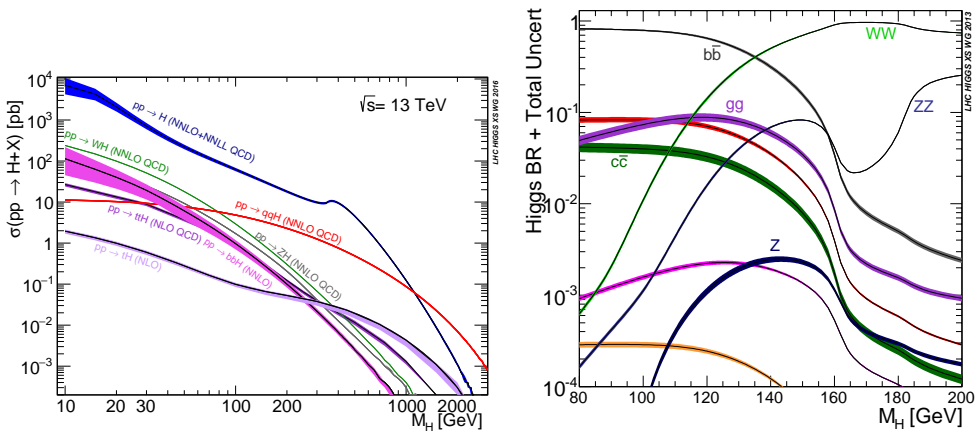


Figure 1.1: (Left) The Higgs production cross section, as a function of the Higgs boson mass, for proton-proton colliders at 13 TeV. (Right) The Higgs branching fractions to SM particles, as a function of the Higgs boson mass.

Even though the Higgs boson only directly couples to massive particles, processes via loops allow decays such as $H \rightarrow \gamma\gamma$ and production mechanisms such as $gg \rightarrow H$, where g are gluons. The latter example is particularly important, since it is the production mechanism with highest cross section at the Large Hadron Collider, a proton-proton collider. For other types of colliders might be different, such as for the Tevatron (proton-antiproton), in which the main production mechanism was through associated production with an electroweak boson.

1.4 Higgs Physics Current Status

While the Higgs boson, and the electroweak symmetry breaking mechanism applied to the SM itself, was predicted in the 60s, it wasn't until 2012 that it was experimentally verified. The CMS and ATLAS experiments, working at the Large Hadron Collider at CERN, detected statistically significant signals compatible with the SM predictions for the Higgs boson, using approximately 5 fb^{-1} of 7 TeV and 8 TeV data.

In 2012, it was not possible to say with certainty that this anomaly was, without a doubt, the SM Higgs. However, five years later, the data that has been analyzed by the LHC experiments has confirmed the SM predictions for this new particle, with a mass measured as about 125 GeV, including its spin (scalar) and CP eigenvalue (even).

The Higgs boson decays to electroweak bosons, $H \rightarrow WW$, $H \rightarrow ZZ$ and $H \rightarrow \gamma\gamma$, have been measured and these branching fractions, assuming SM-like cross section, match the expected values. The Higgs decay modes to pairs of fermions have yet to be detected with the statistical significance seen in its bosonic modes. However, decays involving the third generation of quarks and leptons, $H \rightarrow b\bar{b}$ and $H \rightarrow \tau\tau$, have seen evidence of such processes when combining searches in different production channels. The latest results summary published by CMS and ATLAS can bee seen in Figure 1.2 in terms of signal strengths (μ), defined as the ratio of the measured Higgs boson rate to its SM prediction.

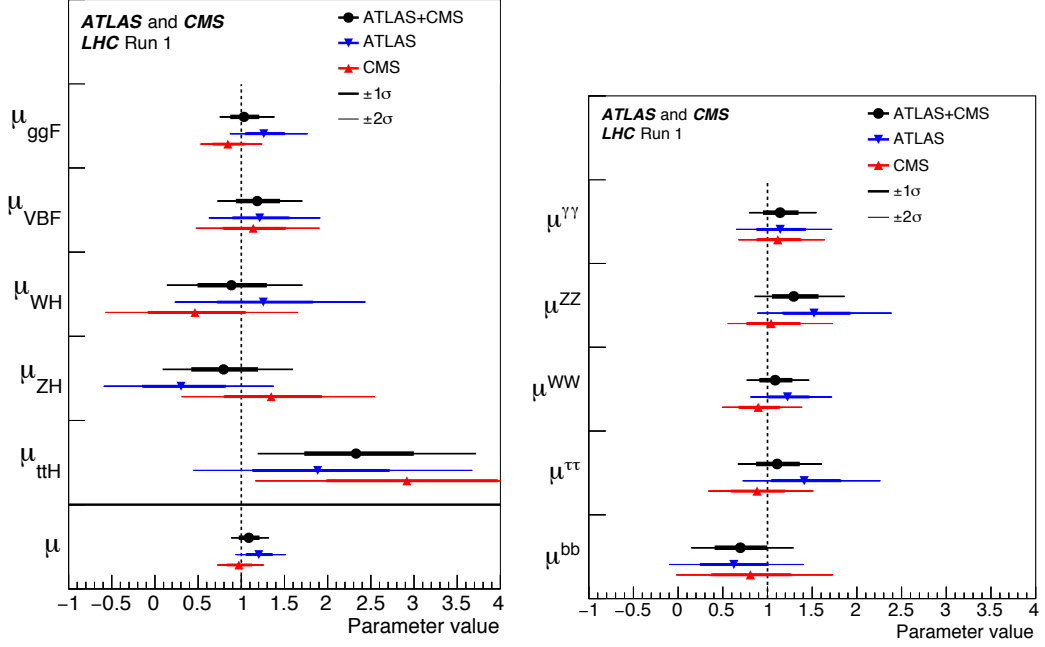


Figure 1.2: (Left) The signal strength measured for the five main Higgs boson production mechanisms, assuming SM branching fractions. (Right) The signal strength measured for the three bosonic Higgs decays and the two third family fermionic decays, assuming SM production.

Other than measuring signal strengths, an important part of studying the Higgs boson is understanding its differential properties. Measuring kinematic distributions related to the Higgs candidates, such as the transverse momentum and pseudo-rapidity profiles, can indicate possible corrections and beyond the SM contributions to the production mechanisms. For example, new particles appearing in the gluon fusion loop can have different coupling structures that induce kinematic correlations not present in the SM. In Figure 1.3, the CMS differential Higgs boson measurements using the $H \rightarrow \gamma\gamma$ channel in terms of the Higgs transverse momentum and rapidity using 8 TeV data.

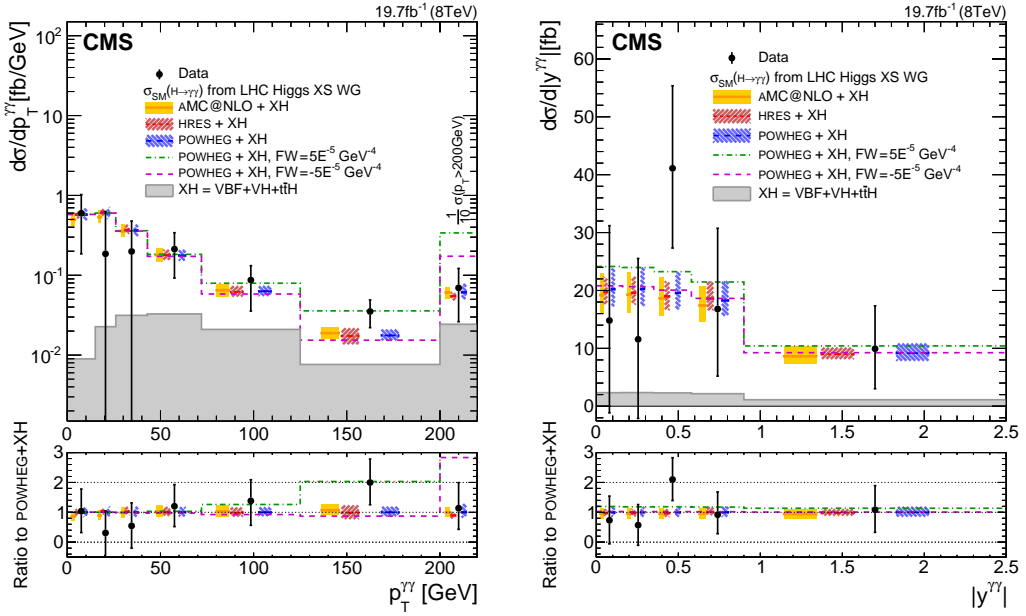


Figure 1.3: CMS differential Higgs boson measurements using the $H \rightarrow \gamma\gamma$ channel in terms of the Higgs transverse momentum (left) and rapidity (right) using 8 TeV data. The measurements are compared to different Monte Carlo generators.

1.5 Higgs as a Probe of New Physics

The experimental confirmation of the Higgs boson marks another success of the SM. However, the measured mass of the Higgs boson poses a naturalness conundrum: being a scalar, the Higgs mass is subject to higher order corrections from loops that contain spin 0, 1/2 and 1 particles, which diverge as a function of the energy scale. If the SM is valid for all energy scales, these corrections would take the Higgs mass to its highest possible energy scale, the Planck scale ($\approx 10^{19}$ GeV), which is in clear contrast with the Higgs mass value known today. In principle, it is possible that the higher order corrections to the Higgs mass cancel out in a way to leave $m_H = 125$ GeV, however, such an "accidental" fine tuning is not well motivated within the theory. The presence of these two distinct and far apart energy scales in the electroweak theory (Higgs mass and electroweak vacuum versus the Planck scale) is called the Hierarchy problem.

Several models and extensions to the SM have been proposed to solve the Hierarchy problem. Among them, and perhaps the most famous, is Supersymmetry (SUSY). SUSY explains the higher order cancellations by postulating a new symmetry of nature that correlates bosons and fermions. By symmetrizing the bosonic and fermionic

contributions to the Higgs mass corrections, the higher order terms are canceled out naturally (since fermion loops contribute with an overall minus sign relative to boson loops).

The existence of SUSY implies that, for every elementary fermion in nature, there must exist a boson superpartner with the same mass (same applies to bosons and fermion superpartners). However, this has not been observed, which means that, if SUSY exists, it must be a broken symmetry. In order to still address the Hierarchy problem, the SUSY breaking scale must be such that the superpartner masses should not exceed $\mathcal{O}(1 \text{ TeV})$. This requirement also has the feature that it unifies the QCD and electroweak coupling constants at $\mathcal{O}(10^{16} \text{ GeV})$.

The simplest supersymmetric extension of the SM, known as the Minimal Supersymmetric SM (MSSM), adds the minimal amount of extra fields to the current model to realize SUSY - in the MSSM, each SM fermion/boson will have one boson/fermion superpartner. It also introduces changes to the Higgs sector: two Higgs doublets are required in order to perform the electroweak symmetry breaking, and give masses to both up and down type quarks and leptons. The existence of this extra doublet now implies that, instead of one Higgs boson mass state, five new bosons exist: two neutral CP-even bosons: h, H (one of which is usually identified as the particle discovered in 2012); one neutral CP-odd boson (pseudoscalar): A ; and two charged bosons: H^\pm .

The MSSM is one example of model that adds to the Higgs sector of the SM an extra scalar doublet. Models with this characteristic are generally referred as Two-Higgs Doublet Models (2HDM). These models are also characterized by new phenomena related to the SM-like Higgs boson, either by exotic production or decay. For the first case to happen, at least one of the new resonances in the model, H for example, must be heavier than the SM-like Higgs (h), which then allows decays such as $H \rightarrow h + X$, where X can either be a Z , an A or even another h . Alternatively, if A , for example, is lighter than $m_h/2 \approx 62.5 \text{ GeV}$, decays such as $h \rightarrow AA$ become possible.

These specific models serve as illustrations of how a modification to the SM can lead to exotic physics to appear in the Higgs sector. More generally, looking for new physics with the Higgs boson is a justifiable ansatz in both phenomenological terms - most extensions to the SM predict specific modifications of the Higgs sector - and in theoretical terms - the Higgs sector is intimately tied to some of the most undesirable features of the SM. Another one of these undesirable features is the electroweak vacuum stability problem.

The electroweak vacuum in the SM is defined as the vacuum expectation value given by the Higgs potential minimum: $v \approx 246$ GeV. Even though the Higgs potential has one global minimum associated to this vacuum, higher order corrections change the shape of this potential and can turn this global minimum into a local minimum. The impact of these corrections are mostly dominated by the Higgs-top quark Yukawa coupling, and so, the stability of the electroweak vacuum depends on the Higgs mass and on the top quark mass, as seen in Figure 1.4.

Given the current values for the Higgs boson and the top quark masses, our universe currently lies at a meta-stable point. These instabilities in the electroweak vacuum can have catastrophic consequences to the fate of the universe, since the vector boson masses, and therefore the strength of the weak interactions, are tied to this value. If it is indeed confirmed that we live in such a state, with more precise measurements for the mass parameters, new mechanisms must be in place to guard the universe against these features.

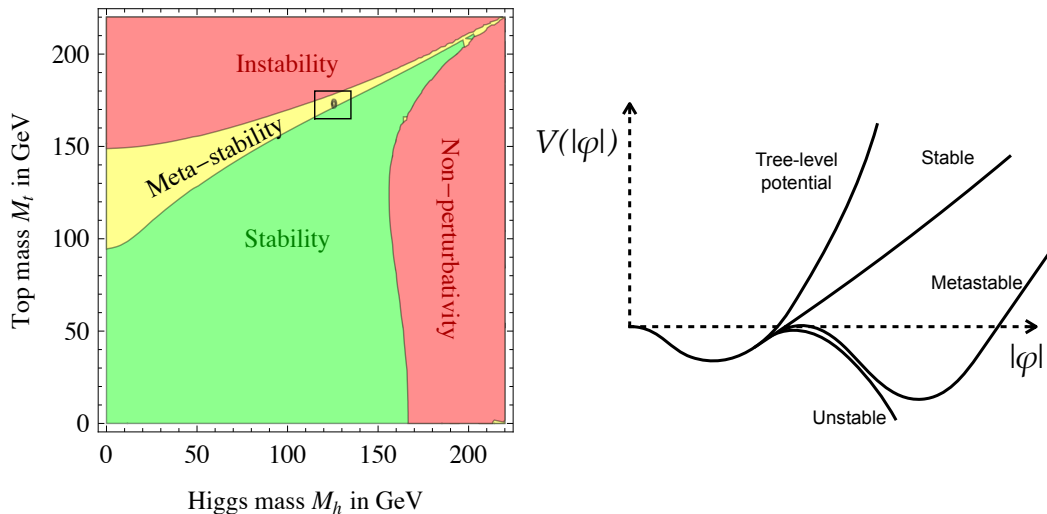


Figure 1.4: CMS differential Higgs boson measurements using the $H \rightarrow \gamma\gamma$ channel in terms of the Higgs transverse momentum (left) and rapidity (right) using 8 TeV data. The measurements are compared to different Monte Carlo generators.

One important caveat of this stability analysis is the assumption that the tree-level Higgs potential has the quartic shape described in Equation 1.6. However, there are no strong indications that $V(|\Phi|)$ must have this exact shape. Theoretically, the SM $V(|\Phi|)$ is the simplest potential that correctly breaks the electroweak symmetry within theoretical constraints, such as unitarity and renormalizability.

Experimentally, in order to probe its shape, the $V(|\Phi|)$ potential parameters must be measured directly. Through the detection of the Higgs boson and its mass measure-

ment, the parameter μ in $V(|\Phi|)$ is determined, since $m_h = |\mu|$. As seen in Equation 1.16, the higher order terms of $V(|\Phi|)$ are related to Higgs self-interaction terms. It's important to note that, even if the *true* Higgs potential (the one that correctly breaks the electroweak symmetry and brings stability to the SM) is not $V(|\Phi|)$, an expansion of this general potential around the vacuum will generally create higher order terms with respect to H . Therefore, directly measuring the Higgs self-interaction terms, such as the Higgs triple coupling, is a crucial step towards understanding the SM.

Chapter 2

The Large Hadron Collider and the Compact Muon Solenoid Experiment

Lorem ipsum dolor sit amet, consectetur adipiscing elit, sed do eiusmod tempor incididunt ut labore et dolore magna aliqua. Ut enim ad minim veniam, quis nostrud exercitation ullamco laboris nisi ut aliquip ex ea commodo consequat. Duis aute irure dolor in reprehenderit in voluptate velit esse cillum dolore eu fugiat nulla pariatur. Excepteur sint occaecat cupidatat non proident, sunt in culpa qui officia deserunt mollit anim id est laborum.

2.1 The LHC Accelerator Complex

2.2 The CMS Experiment

2.2.1 The CMS Tracking Detectors

2.2.2 The CMS Calorimetry Detectors

2.2.3 The CMS Muon Detectors

2.2.4 The CMS Trigger and Data Acquisition Systems

2.2.5 Object Reconstruction at CMS

2.2.5.1 Photons and Electrons

2.2.5.2 Jets

2.2.5.3 Muons

2.2.5.4 Identification of b-quark jets

Einstein's paper: [?]

Chapter 3

The CMS Electromagnetic Calorimeter

The CMS ECAL is a high-resolution, hermetic, and homogeneous electromagnetic calorimeter made of 75,848 scintillating lead tungstate crystals divided among a barrel ($|\eta| < 1.48$) and two endcaps ($1.48 < |\eta| < 3.0$) [?], as shown in Figure ???. The light emitted by these crystals is detected with avalanche photodiodes (APDs) in the barrel and vacuum phototriodes (VPTs) in the endcaps. The signal readout is performed with two avalanche photodiodes (APDs) per crystal in the barrel, and one vacuum phototriode (VPT) in the endcaps. These characteristics, translated into precise energy and timing resolutions, are an invaluable tool for the CMS physics program.

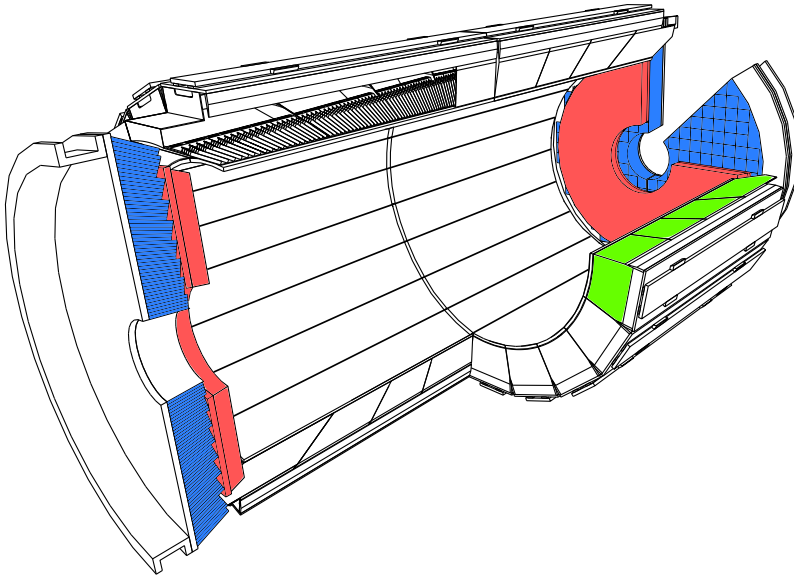


Figure 3.1: The CMS ECAL scheme highlighting a barrel supermodule (green), the ECAL endcaps (blue) and the ECAL preshower (red).

Completing the CMS electromagnetic calorimeter system is a preshower detector (ES), based on lead absorbers equipped with silicon strip sensors. It is installed in front of the ECAL endcaps, covering the region $1.65 < |\eta| < 2.6$. The fine granularity of the ES strips (2 mm wide) can resolve the signals of high-energy photons from the decays of neutral pions into two photons, when the separation angle between the photons is small, and can determine precisely the position of the electromagnetic deposits.

During the first year of Run II data taking at 13 TeV, the LHC provided a challenging environment, with one bunch crossing every 25 ns and an average of 10 interactions per crossing (pile up). This is expected to be even more challenging in 2016, with up to 40 pile up interactions. In the 2015 data taking period, the CMS ECAL operated with more than 98% of its channels active, and was responsible for less than 7% of CMS downtime during physics runs.

3.1 PbWO₄ Crystals and In-detector Electronics

The main component of the ECAL are the lead tungstate crystals, that serve as both active material and absorber, constituting a homogeneous calorimeter. The barrel and endcap crystals are shaped as trapezoidal prisms, with 23 and 22 cm of length, respectively. The crystal's front face (facing the interaction point) has an area of approximately $22 \times 22 \text{ mm}^2$ (about $\Delta\eta \times \Delta\phi = 0.0175 \times 0.0175$) for the barrel and $25 \times 25 \text{ mm}^2$ (about $\Delta\eta \times \Delta\phi = 0.02 \times 0.02$). Examples of such crystals are seen in Figure 3.2.

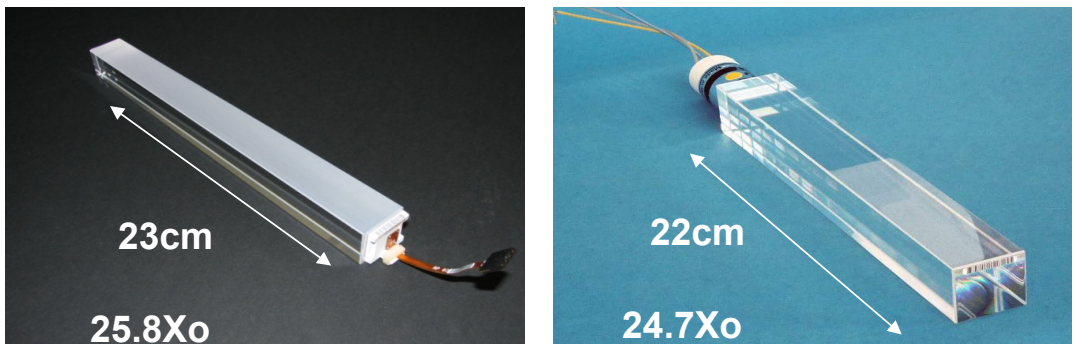


Figure 3.2: Example of lead tungstate crystals as present on the ECAL barrel (left) and on the ECAL endcap (right).

The ECAL crystals are arranged to provide an off-pointing, pseudo-projective geometry, shown in the left of Figure 3.3. In the barrel, the crystals are mounted

in submodules (2×5 crystals in $\phi \times \eta$), which are then mounted into modules and grouped into supermodules. Each supermodule contains 4 modules, three with 10×4 submodules in $\phi \times \eta$ and one with 10×5 . An ECAL supermodule is shown on the right of Figure 3.3.

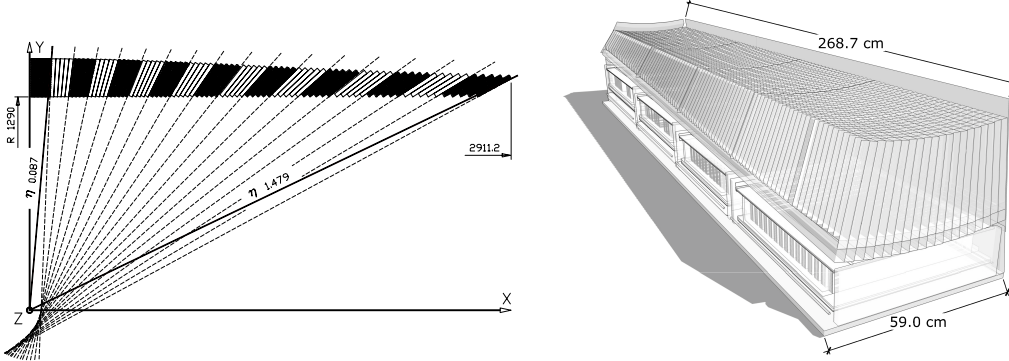


Figure 3.3: On the left, the CMS ECAL scheme highlighting a barrel supermodule (green), the ECAL endcaps (blue) and the ECAL preshower (red). On the right, the details of a barrel supermodule structure.

An energy deposit is measured in the crystal through a scintillation process, in which the lattice atoms are excited and de-excite by the emission of photons. The emission scintillation peak for the ECAL crystals is at about 425 nm, with 80% of the light emission happening within 25 ns. The PbWO_4 crystals are also characterized by a small radiation length ($X_0 = 0.89$ cm), the mean length of that path that takes a high energy electron to lose $(1 - 1/e)$ of its energy in that medium, and a small Molière radius ($R_M = 2.19$ cm), the radius of a cylinder that contains 90% of the shower energy.

On the other hand, the ECAL crystals have a low light output yield (about 10 photo-electrons per MeV), and therefore must be coupled to high gain light detectors. These detectors must also be radiation hard, to cope with the LHC environment, and be stable under a 4T magnetic field (the CMS solenoid magnet). For the ECAL barrel, avalanche photodiodes (APDs) were chosen due to their high gain (50), despite their temperature dependence, which requires ECAL to have a temperature control with a precision better than 0.1°C (the PbWO_4 crystals light yield is also dependent on temperature, with lower light yields for lower temperatures). The ECAL APDs are also characterized by their fast, 2 ns rise time, which allows time measurement with the crystals scintillation pulse shape. By the time of the ECAL construction, APDs were generally produced in small sizes in comparison to the crystal's rear side area, where they must be attached. For this, two APDs were used for each crystal.

On the endcaps, the radiation dose incoming is much higher than in the barrel, which does not allow the usage of APDs in the high η region. For this reason, vacuum photo-triodes (VPTs) are used instead. While more resistant to radiation, these light detectors have generally a smaller gain (8-10).

3.2 Trigger and Data Acquisition Systems

The ECAL trigger and data acquisition system (Trigger and DAQ) takes care of the the entire data flow from the crystals to the central CMS Trigger and DAQ systems, a schematic version of the system is shown in Figure 3.7.

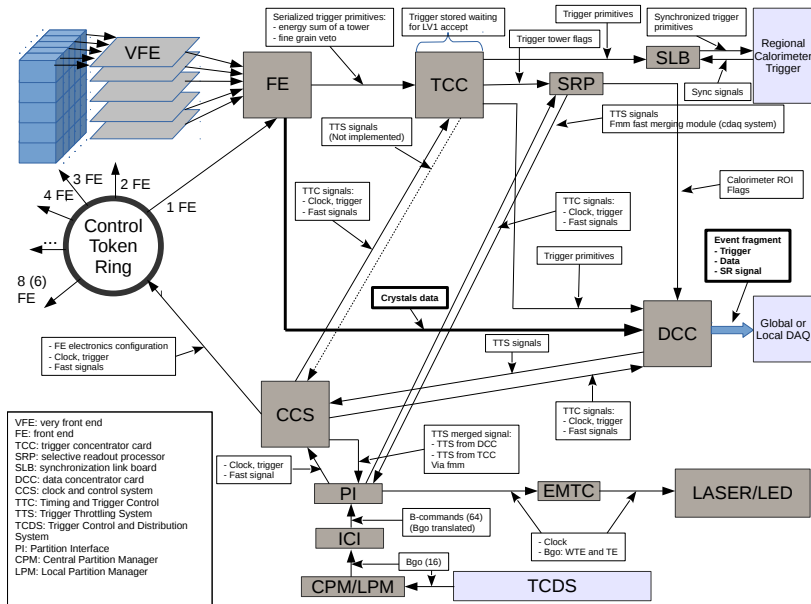


Figure 3.4: ECAL DAQ simplified scheme.

3.2.1 Data Flow

The ECAL data flow starts right after the signal is detected by the photo detectors attached to the crystals. The first step in the chain is the amplification and digitization of the analog signal coming from the APDs and VPTs. This is performed with multi-gain pre-amplifiers (MGPA). The ECAL MGPA work with amplification gains: gain-12, gain-6 and gain-1. The shaping time associated with this amplification process is of about 40 ns. The signal is then sampled and digitized at a rate of 40 MHz. One pulse shape is then reconstructed using 10 of these samples. The

electronics responsible for the amplification and digitization step is generally called very-front-end electronics (VFE).

The VFE sends information to the front-end electronics (FE) at the sampling rate. The FE is responsible for creating trigger primitives, basic information such as energy and position, from arrays of 5×5 crystals (trigger towers). The trigger primitives are sent from the FE to the trigger concentrator cards (TCCs) at sampling rate, and passed to the CMS Level-1 trigger (L1A signal). The VFE and the FE, known as the in-detector electronics, are placed right at the detector, close to the crystals, which is schematically shown in Figure 3.5. In Figure 3.5, the chips dedicated to generating and transmitting the serialized trigger primitives (FENIX chips) are shown, along with the gigabit optical hybrids (GOH) chips dedicated to data transmission and the chips dedicated to receiving and distributing timing and control data (CCU).

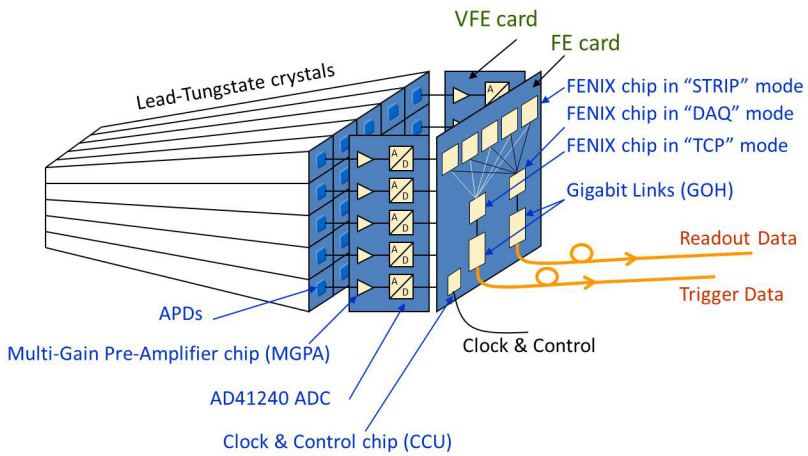


Figure 3.5: ECAL in-detector electronics simplified scheme.

During the time it takes for a decision to be made by the L1 trigger, the trigger primitives are stored at the TCCs. In case the event is not accepted, these trigger primitives and the full crystal information stored at the FE are flushed from memory. If an event is accepted, the FE sends the serialized full individual crystals information to the data concentrator cards (DCCs), that will pack the event in a format readable by the CMS central DAQ.

In parallel, the TCC sends the trigger primitive information to the selective read-out units (SRPs) after an L1A arrives. The SRP selects which portions of the detector should be unpacked by the DCCs based on an algorithm called Selective Readout (SR), reducing the load of processing by the DCCs. The DCCs load is limited by the current electronics architecture and can be trespassed when the average activity per event is increased, such as in high pile up LHC runs. The SR algorithm classifies

trigger towers as low interest ($E_{TT} < 1.5$ GeV), medium interest ($1.5 < E_{TT} < 2.5$ GeV) or high interest ($E_{TT} > 2.5$ GeV). If a trigger tower is classified as low interest, only the crystals with energy higher than 4.5 (6.5) ADC in the barrel (endcap). If a trigger tower is classified as medium interest, all crystals are unpacked, regardless of their energies. If a trigger tower is classified as high interest, all crystals in that trigger tower, and the 8 trigger towers around it are fully read.

3.2.2 Timing and Control Distribution

In order to ensure a synchronized working of all different parts of the ECAL DAQ system, a precise distribution of clock and control signals must be achieved. This is performed via a combination of different ECAL and central CMS electronics. For Run 2, CMS installed a new subsystem dedicated to distributing these signals among all CMS partitions, the Timing and Control Distribution System (TCDS). TCDS communicates timing/synchronization signals coming from the LHC and CMS (clock), L1As coming from the CMS Level-1 trigger, and configuration and control commands synchronously to all CMS components. These signals are then distributed among ECAL components via the clock and control system (CCS), including to the front-end electronics (through control token rings).

3.2.2.1 TCDS

The TCDS subsystem was installed on CMS during the Long Shutdown 1 in order to cope with the new running conditions for Run 2. Specifically, new detector subsystems were being installed in the experiment (such as the new pixel inner tracker layers). Instead of expanding the old system, a choice was made to construct a new infrastructure with updated hardware, firmware and software. The TCDS system consists on three types of boards: the Central Partition Manager (CPM), the CMS Interface boards (iCI) and the Partition Interface boards (PI).

The TCDS CPM is fully controlled by the central TCDS system, and has information regarding the type of runs to be started by the central DAQ. This information defines, for example, at which point of the LHC orbit to send specific signals to the subdetectors. The iCIs must work as a library that translates the CPM signals into specific actions to be taken by the different subdetectors. This means that the iCIs must be configured properly and individually by each subdetector. In order to achieve that on ECAL, a new software interface to TCDS was written to configure and monitor the ECAL iCIs. The PIs act as fan-out boards to distribute the iCI messages among different subdetector components.

3.2.3 Software Architecture

The ECAL DAQ software architecture controls, configures and monitors the readout and trigger electronics described in the previous sections. The framework implementation is based on a CMS common framework developed by the central Trigger and DAQ group, mostly consisting of C++ xDAQ framework [?], while the top layer of the system is based on the JAVA RCMS [?] framework.

The overall system accomplishes several different tasks. It configures and monitors the different components of the FE and off-detector electronics. It communicates with the central CMS TCDS, both sending the correct configuration parameters for the dedicated TCDS ECAL boards and receiving and translating these commands to the off-detector electronics. It is also able to perform different types of runs dedicated to calibration and detector developments, such as "MiniDAQ" and "local" runs.

With the xDAQ framework, the ECAL software communicates to the ECAL boards through SOAP (Simple Object Access Protocol) messages. SOAP messages are also used to communicate issues with the off-detector electronics directly to the central DAQ system.

There are five main components to the ECAL DAQ software architecture:

ECAL Function Manager Function managers (FM) work as the overall controller of actions happening to the ECAL software. It has the power to send commands to the ECAL supervisor to cause state transitions, triggering actions such as the beginning of a run. During global CMS runs, the central DAQ function communicates such actions to the ECAL function manager. In specific runs in which ECAL controls its own sequence, the ECAL function manager works by itself.

ECAL Supervisor The ECAL supervisor is at the top of software control and coordinates all other working pieces. It receives the commands from the ECAL function manager and, to any given command, proceeds with the specific steps to ensure the state transitions of the different com ECAL components.

Services Supervisors For each different services described in the previous sections (TCC, DCC, DCS and SRP), a dedicated software exists in order to perform the actions related to specific state transitions.

TCDS Supervisor A specific supervisor was developed to communicate with the central TCDS service. It sends the proper configuration parameters to the TCDS ECAL boards, with the list of commands to be passed to the ECAL

electronics when certain state transitions happen and during specific run conditions.

Monitoring Services In order to retrieve and display information about the status of the off-detector electronics, specific services based on xDAQ capabilities are used. These services also monitor the ECAL DAQ computing capabilities to make sure all machines are working properly. Depending on what type of error is detected by the monitoring services, SMS's and e-mails are sent to ECAL DAQ experts.

3.2.3.1 ECAL DAQ Finite State Machine

One of the main goals of the ECAL Supervisor is to ensure the proper state transitions of the different DAQ components through the allowed states of the ECAL DAQ Finite State Machine (FSM), summarized in Figure 3.6.

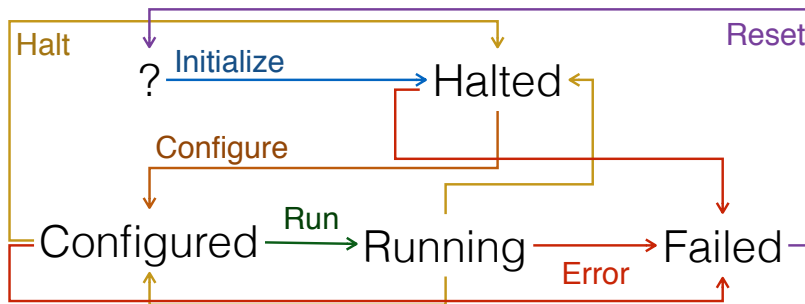


Figure 3.6: Simplified view of the ECAL Finite State Machine and its transitions.

Similarly to the central CMS FSM, the transitions are:

Initialization The Initialization procedure tests the connection between the ECAL Supervisor and the different off-detector components and initializes all required drivers. The information about the hardware resources is then propagated back to the supervisor and the ECAL FM. The initialization transition takes the FSM to Halted state and makes it ready to be configured.

Configuration When the configuration signal is received, it reads the configuration parameters from the ECAL Configurations DataBase (ConfDB) and sends to the off-detector electronics, which are then loaded accordingly. Each different Service Supervisor independently ensures their components have been successfully configured and communicate it back to the ECAL Supervisor. This action takes the FSM to Configured state and is now ready to start producing data (running). It also enables the monitoring services.

Start The start command kicks-off the full data flow described at the beginning of this section, including trigger primitive production and delivery to the L1 trigger, and the delivery of the full data information upon an L1A. It also starts the delivery of monitoring data from the off-detector electronics to the monitoring services. This action takes the FSM to Running state.

Stop/Halt These actions take the system either from Running state to Configured state, or from Running or Configured states to Halted state, respectively. The Stop command interrupts the ECAL DAQ data flow, while the the Halt command interrupts the data flow and flushes the database parameters from the off-detector electronics.

Error Any error during the previous transitions will take the FSM to Failed state.

3.2.3.2 Types of Running Conditions with the ECAL

Global Runs A global run is the usual working condition of ECAL with the full CMS central DAQ infrastructure. In global runs, the ECAL FM receives commands directly from the central DAQ FM, including all state transition actions. These runs happen when the LHC is running, when CMS is taking cosmics data (with its magnetic field on or off) or when specific tests must be performed with the full central DAQ infrastructure.

MiniDAQ Runs These runs happen with a dedicated central DAQ infrastructure that is independent of global runs, and therefore can run in parallel. They are used on ECAL to test the state of the off-detector electronics and investigate possible errors seen in global runs. MiniDAQ runs have also been used in 2015 and 2016 to measure the response of the ECAL electronics to noise (pedestals) and to test pulses generated by the on-detector electronics.

Local Runs Local runs are completely independent from the central DAQ infrastructure. They rely on ECAL software to both directly configure the off-detector electronics and process the data that is produced by the DCCs. This freedom allows for more complex types of running conditions, such as the ones needed for more coherent measurements of ECAL pedestals (to be used in 2017).

3.3 Electron and Photon Energy Reconstruction

The photon and electron energy reconstruction based on ECAL energy deposits is based on the formula:

$$E_{e,\gamma} = \left[\sum_i (S_i(t) \times c_i \times A_i) \times G(\eta) + E_{ES} \right] \times F_{e,\gamma}, \quad (3.1)$$

with A_i , c_i and $S_i(t)$ as, respectively, the per individual channel amplitude, intercalibration constant and light monitoring constant, $G(\eta)$ is the ADC to GeV absolute scale, E_{ES} is the energy deposit in the preshower, and $F_{e,\gamma}$ are the cluster corrections (different for photons and electrons). The methods used to obtain the different terms in this equation will be detailed in the next sections.

3.3.1 Online Reconstruction

The time spacing between two consecutive samples from the ECAL readout electronics is 25 ns, which is the same time spacing between two colliding bunches in the LHC. This implies that, during the readout of one pulse, another scintillation process might start in the same crystal, compromising the in-time amplitude reconstruction. To mitigate this effect, also called out-of-time (OOT) pile up, a new online pulse reconstruction method (multifit) was developed to replace the Run I method [?].

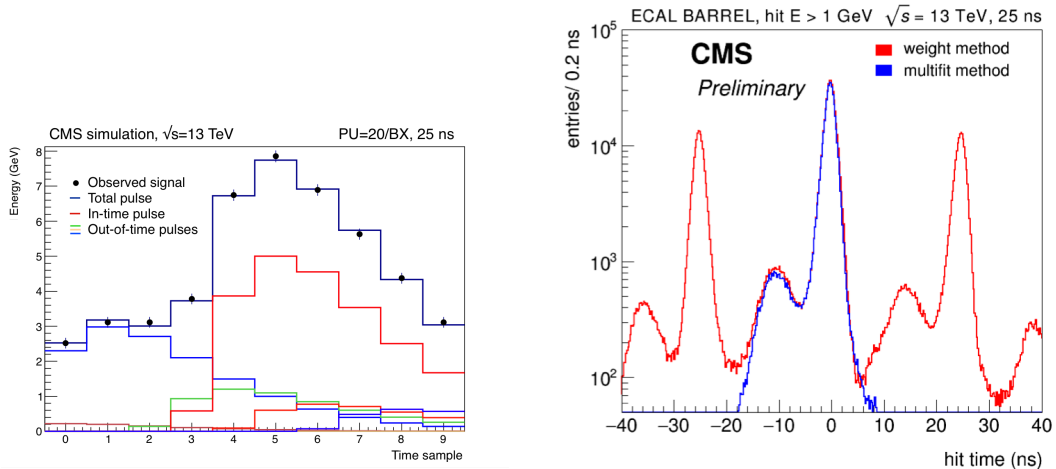


Figure 3.7: (Left) Fitted pulse shapes with the multifit method. (Right) In-time and out-of-time contributions to energy reconstruction with weights method (red) and multifit (blue).

In the multifit method, the pulse shape is reconstructed based on a fit to the time samples, minimizing $\chi^2 = \sum_{i=1}^{10} \left(\sum_j^M A_j p_{ij} - S_i \right)^2 / \sigma_{S_i}^2$. The samples (S_i) are fitted

with one in-time pulse shape template, plus up to 9 out-of-time templates (p_{ij}) times their respective amplitudes (A_j). σ_{S_i} is noise generated by electronics associated with the crystal readout chain. The OOT templates have the same shape as the in time one, but are shifted in time by multiples of 1 bunch crossing (1 BX = 25 ns), within a range of -5 to +4 BX around the in time signal (BX = 0). The pulse shapes have been measured in early 2015, in special runs in which the LHC delivered isolated bunches (no OOT pile up).

It has been observed in both data and simulation that, with the multifit method, OOT pile up reconstruction is negligible. The energy resolution improvement, with respect to the Run I amplitude reconstruction method, is substantial especially for low E_T photons and electrons, given the larger contribution of deposits from pile up to the total energy.

3.3.2 Response Monitoring

Time dependent corrections must be applied to the reconstructed amplitude due to changes in detector response with radiation exposure. These changes in response are due to decreases in crystal transparency and variations in VPT response in endcaps.

The changes in the crystal transparency is due to ionizing radiation creating color centers in the lead tungstate. While the scintillation process remains intact, the amount of light detected by the photodetectors decreases. This effect is partially mitigated through thermal annealing, causing the transparency to increase in the absence of radiation.

A light monitoring system is used to monitor the overall changes in response in the ECAL [?]. It consists of a system of lasers (operating at 447 nm, close to the wavelength of peak emission for lead tungstate) that injects light in each ECAL crystal, which is then read by the standard ECAL readout. The change in transparency per crystal (R/R_0) is then related to the ratio between reconstructed amplitude and the injected light amplitude (S/S_0) through the formula:

$$\frac{S}{S_0} = \left(\frac{R}{R_0} \right)^\alpha, \quad (3.2)$$

where α has been measured in beam tests and is ≈ 1.5 . S/S_0 is then used as a correction factor to account for the response changes.

The light monitoring infrastructure is an integral part of the ECAL DAQ. It works alongside of the main data flow, in specific periods in which the LHC bunches are empty (orbit gaps). During the orbit gaps, the laser system is shown in different parts

of the ECAL barrel and endcaps. In about 40 minutes, one reading of the full ECAL is performed.

The history of response change measurements is summarized in Figure 3.8. The changes are up to 6% in the barrel and reach up to 30% at $|\eta| \approx 2.5$, the limit of the tracker acceptance. For high $|\eta|$ regions, changes are up to 70%. The recovery of the crystal response during the long shutdown period is visible. The response was not fully recovered, however, particularly in the region closest to the beam pipe. The monitoring corrections are validated by comparing isolated electron energy as measured by ECAL (E) and momentum as measured by the CMS Tracker (p), before and after light monitoring corrections. It is seen that the measured corrections bring stability to energy measurements with ECAL.

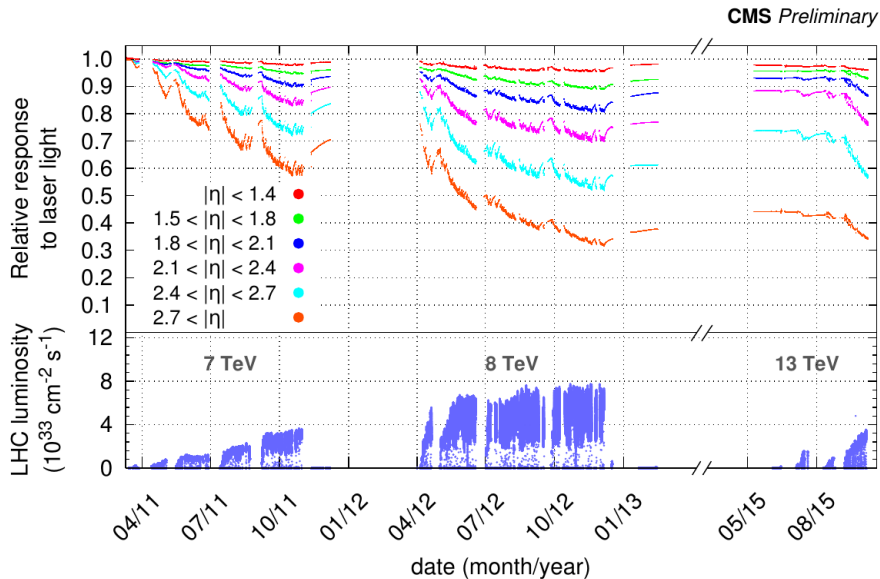


Figure 3.8: History of channel response changes as measured by the light monitoring system.

In Figure 3.9, it can be seen how the laser corrections impact the stability of the ECAL energy measurement. In this plot, the ratio between the energy of an isolated electron as measured by the ECAL (E) and by the CMS Tracker (p) is shown as a function of time. Due to the response changes in the crystals and photon detectors, the ratio decreases when left uncorrected. After the laser correction is applied, ECAL achieves a stable energy measurement in time.

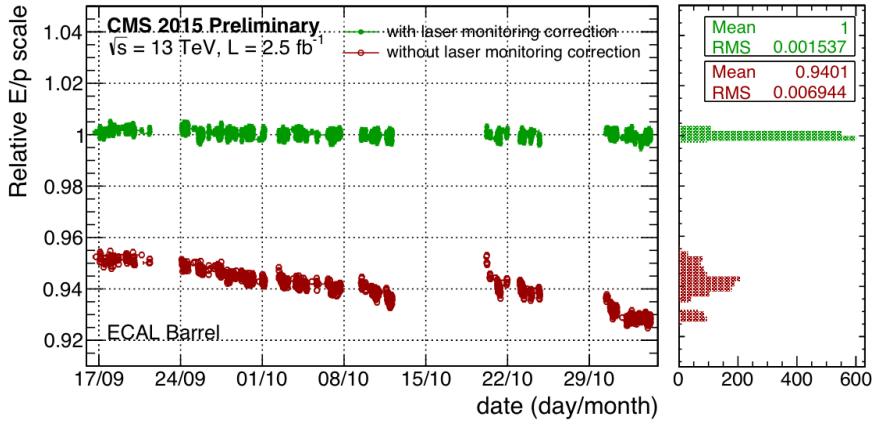


Figure 3.9: Stability of electron energy measurement with and without applying laser monitoring corrections.

3.3.3 Intercalibration

A relative calibration procedure in all ECAL channels is performed to ensure uniformity across the detector. Different and independent methods are used to calculate intercalibration constants (ICs), which are then combined to achieve the desired precision of $< 0.5\%$. The final 2015 version of the ICs have been calculated with the full 2.6 fb^{-1} dataset recorded by CMS with $B=3.8 \text{ T}$. The following methods are the same as in Run I [?].

ϕ -Symmetry The ϕ -symmetry method is based on the expected uniformity of the energy flux along ϕ rings (region with fixed η). The ICs are calculated to correct non-uniformities in this flux. This method was used in 2015 to translate the latest ICs, calculated with the full 2012 dataset, to the 2015 detector conditions. This was done by scaling the 2012 ICs by the ratio between 2015 and 2012 ϕ -symmetry ICs.

π^0/η The π^0/η method consists of measuring the invariant mass of these resonances' decays to two photons and maximizing their resolutions by varying the ICs iteratively. This method does not utilize the absolute value of the π^0 and η resonances not to interfere with the absolute scale calibration.

E/p The E/p method employs the same logic as the light monitoring validation method, comparing isolated electron energy and momentum. An iterative method is used to minimize the spread of the E/p distribution.

The combined intercalibration was obtained from the mean of the individual ICs at a fixed value of η , weighted by their respective precisions. The residual miscalibration of an intercalibration method, which is related to the final method precision, is calculated as the spread of the difference between the method's ICs and the other methods' ICs at a fixed value of η . This residual miscalibration can be seen in Figure 3.10 (left) for the ECAL barrel, where it is shown that the combination of ICs achieves the desired goal of less than 0.5% precision for the central barrel region. The overall impact of applying the intercalibration constants and the response monitoring corrections can be seen in Figure 3.10 (right), in $Z \rightarrow ee$ events.

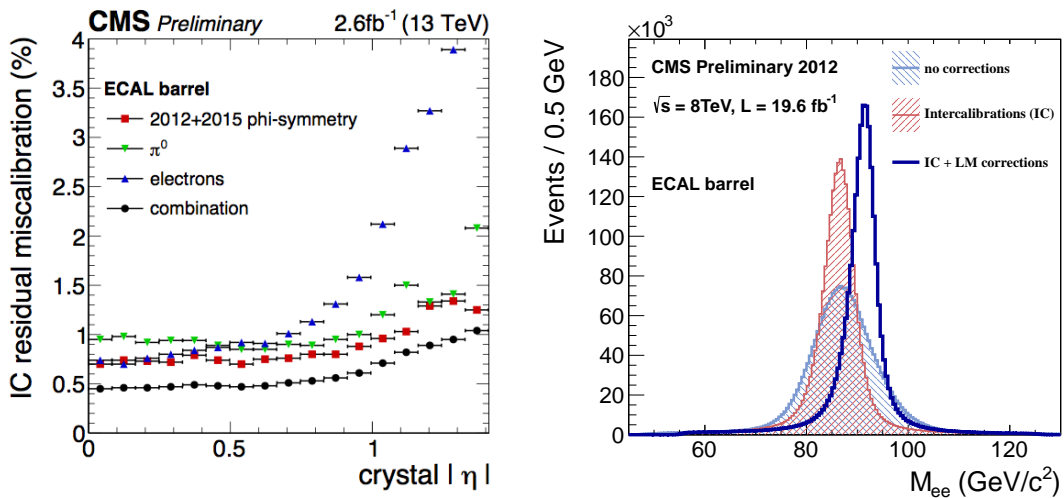


Figure 3.10: Residual mis-intercalibration with the different ECAL intercalibration methods and their combination.

3.3.4 Absolute Calibration

$Z \rightarrow ee$ events are used both to set the η scale and the absolute calibration [?]. The first is developed to ensure that different η regions have the same relative response, while the second (done separately for barrel and endcaps) sets the absolute energy scale.

A dedicated calibration was performed with 0 T data to account for differences in shower shapes in the absence of magnetic field. For example, in 0 T there is no bremsstrahlung radiation outside the main electron cluster deposit, improving the reconstructed energy resolution.

In addition, the calibration was validated with high energy photons and electrons. The validation was performed by comparing data and Monte Carlo simulations for high energy electrons from $Z \rightarrow ee$. The calibration was found to be stable to 0.5%

(0.7%) for electrons up to $p_T = 150$ GeV in the barrel (endcap). Possible saturation effects were corrected for with a multivariate technique, but those effects were found to be < 2% for photons arriving from resonance masses less than 1.4 TeV.

3.3.5 High Level Calibrations

The amount of material in front of ECAL, up to $2X_0$ in the barrel outer regions as seen in Figure 3.11 (left), produces a high rate of bremsstrahlung radiation from electrons and a high probability of photon conversions. To mitigate this effect, a clustering algorithm is used to recombine energy deposits that come from those processes. The cluster energy is corrected via a multivariate technique, separately for photons [?] and electrons [?]. It also aims to correct other effects, such as in time pile up. The effect of these high level cluster corrections on the resolution of the $Z \rightarrow ee$ peak can be seen in Figure 3.11 (right).

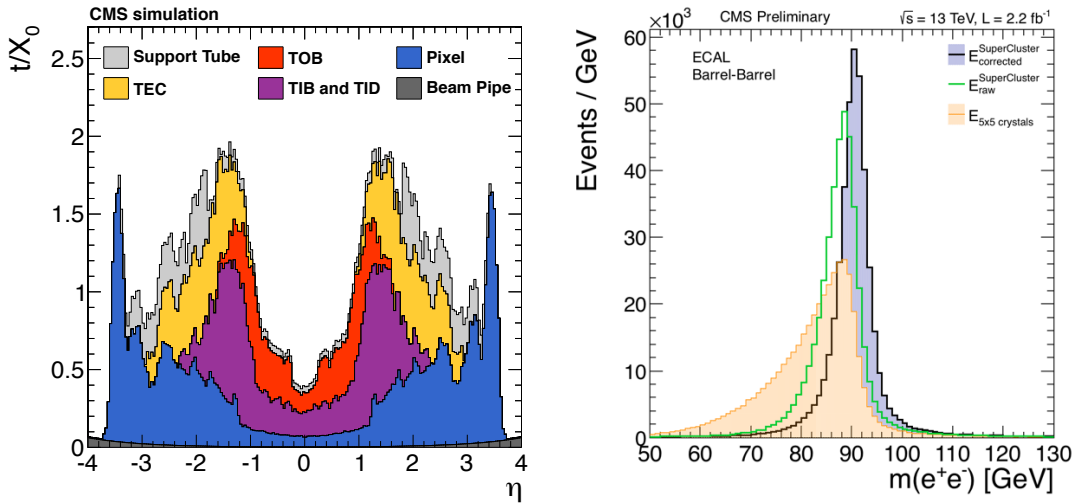


Figure 3.11: Material budget between the ECAL and the collision point on CMS (left). Effect of high level cluster corrections on the resolution of the $Z \rightarrow ee$ peak.

3.4 ECAL Energy Resolution

3.4.1 Energy Resolution of a Calorimeter

The intrinsic energy resolution of an electromagnetic calorimeter can be parametrized in terms of three sources, as in the following equation:

$$\frac{\sigma}{E} = \frac{A}{E} \oplus \frac{B}{\sqrt{E}} \oplus C, \quad (3.3)$$

where the first term on the right-side of the equation is called the noise term, the second is called the stochastic term and the third, the constant term. A brief explanation of the physical nature of these uncertainties follows:

Noise term The noise term is the contribution to the energy resolution from the electronic noise in the readout chain. In the case of ECAL, this noise comes from the VFE and FE part of the detector, specially in the light detection phase by the photo-detectors and on the amplification and sampling phase by the MGPA.

Stochastic term This contribution to the resolution comes from the physical development of the shower shape inside the detector. For homogeneous detectors, such as ECAL, this term is usually small, since the full shower development is contained within the active medium.

Constant term Differently from the other two terms, this one is independent of the energy of the incoming particle in the detector. This uncertainty is related to geometrical and static features of the detector, such as non-uniformities and random instabilities in response that are independent on energy. On ECAL, this contribution is largely mitigated by the intercalibration and laser monitoring calibration.

During the ECAL test-beam commissioning period, these terms were measured directly as: $A = 128 \text{ MeV}$, $B = 2.8 \sqrt{\text{GeV}}$ and $C = 0.3 \%$.

3.4.2 ECAL Energy Resolution with Run II data

The ECAL energy resolution is measured using $Z \rightarrow ee$ events, from an unbinned fit with a Breit-Wigner function convoluted with a Gaussian as signal model. Degradation effects come from the amount of material in front of ECAL and cracks between modules. The resolution, as a function of η , for low bremsstrahlung electrons in the barrel can be seen in Figure 3.12.

The energy resolution achieved with reprocessed data, which includes the latest intercalibration and calibration constants derived with 2015 data, achieves a resolution that is less than 2% for $Z \rightarrow ee$ low bremsstrahlung electrons in the central barrel region. The reprocessed data is especially better performing in the endcaps, when comparing to processed data with 2012 values for intercalibration and calibration. When ported to physics analysis, this energy resolution implies, for example,

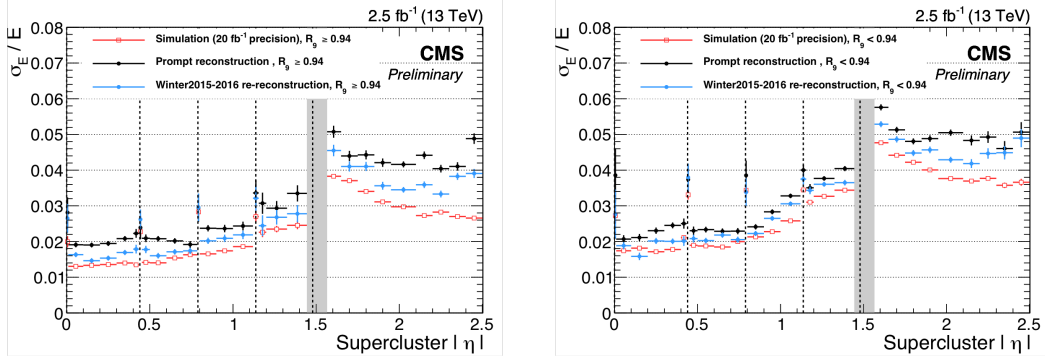


Figure 3.12: Energy resolution for low (left) and high (right) brehmsstrahlung $Z \rightarrow ee$ electrons as a function of η .

in a $\sigma_{eff}/M_h \approx 1.5\%$ (from simulation) in the $H \rightarrow \gamma\gamma$ analysis, where σ_{eff} is the smallest interval in $M(\gamma\gamma)$ with 68.5% coverage [?].

3.5 The CMS ECAL Barrel Upgrade

3.5.1 The High Luminosity LHC

The performance of the Large Hadron Collider, and the physics program carried by ATLAS and CMS, has started remarkably. With the discovery of the Higgs boson in 2012, and the expected 40 fb^{-1} to be delivered in 2016 with record high instantaneous luminosity, the program has exceeded experimental expectations. The current LHC setup, with bunch spacing of 25 ns and peak instantaneous luminosity of the order of $10^{34} \text{ cm}^{-2}\text{s}^{-1}$, is expected to deliver around 300 fb^{-1} until the end of 2022, when the Long Shutdown 3 (LS3) is planned to start.

During LS3, which is planned to last until 2025, the LHC is expected to replace the quadrupoles that focus the beam for ATLAS and CMS. Additionally, upgrades will be performed to optimize the bunch overlap at the interaction region. These improvements are expected to allow the LHC peak luminosity to reach $2 \times 10^{35} \text{ cm}^{-2}\text{s}^{-1}$ (High Luminosity LHC, HL-LHC). During the following 10 years, $250 \text{ fb}^{-1}/\text{year}$ are expected to be delivered. This full dataset of around 2500 fb^{-1} will open a brand new physics program at the LHC, involving precise measurements of the Higgs properties and rarer standard model phenomena, such as the standard model Higgs pair production.

The new LHC configuration will also bring new experimental challenges. With the increased peak luminosity, a higher dose of radiation will be reaching the inner detectors of ATLAS and CMS, causing unrecoverable losses of efficiency in tracking reconstruction and calorimetry, for example. It will also challenge the online performance of the detectors, forcing the trigger systems to cope with higher event rates. To recover their performances to comparable or higher levels of the previous data taking periods, ATLAS and CMS have planned hardware upgrades to be deployed during LS3.

3.5.2 ECAL Electronics Upgrade

As mentioned in the previous section, the impact of incoming radiation on ECAL is to form color centers on the crystals that damage its transparency. With the incoming dose of radiation at the HL-LHC, the endcap crystals are expected to completely lose their transparencies. This prompted the CMS community to entirely replace the ECAL endcaps for its HL-LHC upgrade. The new ECAL endcap will be based on silicon technology, as a sampling calorimeter (HGCal).

On the ECAL barrel, the crystals are expected to robustly cope with the incoming dose of radiation, and will therefore be kept in the detector. However, the new levels of radiation will also represent a challenge to the in-detector electronics. For example, the dark current on the APDs (the electric current flowing through the photo-detector even in the absence of signal, created by random processes) is expected to increase, given the higher ionizing radiation dosage hitting the detector. This dark current is a large contributor to the noise term in the energy resolution formula, specially to homogeneous calorimeters, and upgrades must be devised to keep it under control.

3.5.2.1 VFE Upgrade

For the HL-LHC upgrade, two ways to mitigate the increased detector noise have been investigated: replacing the VFE and cooling the ECAL crystals and APDs from 18°C to 8°C . The APDs cooling works reducing the dark current expected at high integrated luminosities scenario. The downside of this upgrade is the decreased light yields from scintillation from the lead tungstate crystals. The VFE upgrade intends to reduce the electronics noise by reducing the shaping time attached to the amplifying process, currently is 40 ns. This reduction limits the impact of electronics noise in the amplitude reconstruction, while also allowing for a more precise time resolution from ECAL. These improvements can be seen in Figure 3.13 (left). Figure 3.13 (left) also shows that, in the scenario with no HL-LHC upgrades, the noise present on the ECAL barrel would reach levels almost 10 times higher than the current value (1.5 ADC counts). The upgrade reduces the noise at 3000 fb^{-1} by a factor of almost 2.

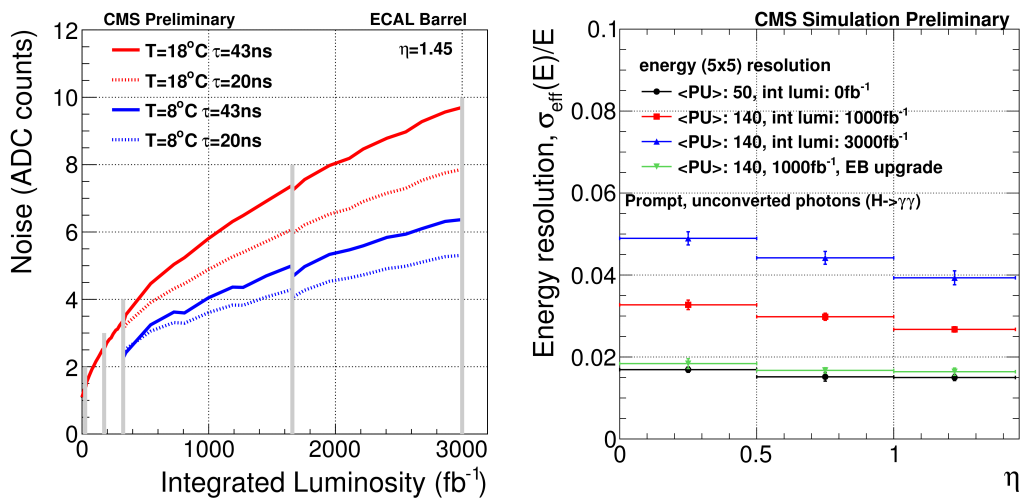


Figure 3.13: Noise levels on the upgraded ECAL barrel assuming different upgrade scenarios.

The noise reduction is translated into physics performance, for example, in $H \rightarrow \gamma\gamma$ searches, as seen in Figure 3.13 (right). Figure 3.13 (right) shows the energy resolution of good quality $H \rightarrow \gamma\gamma$ photons under different integrated luminosity scenarios, with and without the ECAL barrel upgrade.

3.5.2.2 Trigger Upgrade

Another important issue arising from the HL-LHC environment is the increase in electronic spikes in the APDs. These spikes are created when a high energy hadron hits the APDs directly, without showering in the ECAL crystals. This creates an energy discharge in the APD that can fake a signal from a regular particle shower. Spikes are problematic when they happen with high frequency because they enhance L1 trigger rates. These triggers must then have high energy thresholds in order for the rates to be acceptable by the CMS L1 trigger.

Another way currently implemented to suppress spikes at trigger level is through coarse geometric variables. These variables are computed at the trigger primitive generation step, at the front-end electronics. Due to computational limits of the FE boards, these variables use limited information about the crystal array. This can be changed if the TP generation happened at the off-detector electronics instead. However, this would mean transmitting the full crystal information of the whole ECAL to the off-detector electronics at collision rate (40 MHz). By the time of the ECAL commissioning period, the data links could not cope with such requirements, and so the trigger tower based TP generation was implemented.

One of the foreseen ECAL barrel upgrades is aimed at mitigating those constraints by moving the TP generation step to the off-detector electronics. New data links will be used to transmit all crystal data directly from the VFE, instead of being stored waiting for an L1A. With extra computing power based on modern FPGAs, new strategies can be investigated to reduce the impact of spikes at L1 trigger level. One of these strategies is based on analyzing the signal pulse shape coming from the crystals. Given the smaller shaping time from the upgraded VFE, differences in pulse shapes from regular energy showers and spikes can become visible for ECAL.

Chapter 4

Higgs Exotic Decays with Photons and Missing Energy

4.1 Introduction

The final state consisting of a low transverse energy photon and low missing transverse energy (\cancel{E}_T) (also called the “monophoton” final state) can be used to constrain a variety of extensions of the standard model (SM). One such promising extension is supersymmetry (SUSY) [?, ?, ?, ?, ?, ?, ?], which has the attractive feature of stabilizing the radiative corrections to the Higgs boson mass (m_h), while also providing a natural dark matter (DM) particle candidate (χ) in the form of the lightest supersymmetric particle (LSP).

In SUSY scenarios where the SUSY breaking scale is low ($\sqrt{f} \sim \text{TeV}$) the newly discovered Higgs boson ($m_h = 125 \text{ GeV}$) [?, ?] may decay into a gravitino (\tilde{G}) and neutralino ($\tilde{\chi}_1^0$), with the neutralino subsequently decaying into a gravitino and a photon [?]. In this model, the gravitino is the LSP and the neutralino is the next to lightest supersymmetric particle (NLSP). Figure 4.1 shows the Feynman diagram for this process.

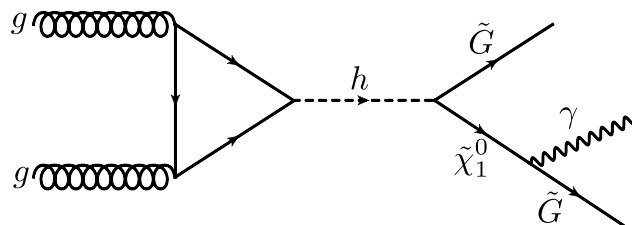


Figure 4.1: Feynman diagrams of a Higgs boson decay to gravitino LSP and a neutralino NLSP, which subsequently decays to a gravitino and photon.

This decay mode produces a single isolated photon and \cancel{E}_T from the undetected gravitinos. If $m_{\tilde{\chi}_1^0} < m_h/2$, the decay process $h \rightarrow \tilde{\chi}_1^0 \tilde{\chi}_1^0 \rightarrow \gamma\gamma + \cancel{E}_T$ would dominate. Therefore the kinematic region of interest for this search is $m_h/2 < m_{\tilde{\chi}_1^0} < m_h$. Furthermore, since $m_h = 125$ GeV, the photon transverse energy (E_T^γ) and \cancel{E}_T will be relatively low.

In this document, we present a search for new physics in the low- E_T photon+ \cancel{E}_T final state, using an integrated luminosity at 7.3 fb^{-1} of $\sqrt{s} = 8$ TeV LHC pp collision data collected with the CMS detector. This study is the first CMS search conducted in this low energy regime and it complements and expands upon previous high-energy monophoton searches for new physics conducted at the LHC [?, ?]. The results are interpreted in terms of the low-scale SUSY breaking model, as well as in a model independent manner.

4.2 Event selection

Events for this analysis are collected using a single HLT path, which is seeded by either a 20 GeV or a 22 GeV single e/γ L1 trigger depending on the running period. The HLT is used to select events with at least one photon with $E_T > 30$ GeV within the ECAL barrel region ($|\eta^\gamma| < 1.44$) and calorimetric $\cancel{E}_T > 25$ GeV with noise cleaning to suppress the anomalous noise in the HCAL barrel (HB) and endcap (HE) subdetectors due to characteristics of the hybrid photodiodes and the readout boxes [?]. The trigger further requires the photon to pass a loose calorimeter-based isolation selection and to exhibit shower shape characteristics consistent with unconverted photons. The main shower shape requirement is based on the R_9 variable, defined as the ratio of the energy deposited in a 3×3 crystal region centered around the crystal containing an energy deposit greater than all of its immediate neighbours (the “seed crystal”) to the energy of the entire deposit of the photon (“supercluster”). The data recorded with this trigger corresponds to an integrated luminosity of 7.3 fb^{-1} and was part of the CMS “data parking” program in 2012. With the data parking program, CMS recorded additional data with relaxed trigger requirements planning for a delayed offline reconstruction in 2013 after the completion of the LHC Run I.

The efficiencies of the trigger as a function of offline reconstructed E_T^γ and \cancel{E}_T are measured using two prescaled control trigger paths. The first control trigger path accept events with single photons with energy greater than 30 GeV with no further identification or isolation requirements on the photons. The second control trigger path has identical photon requirements to the signal path but without any selection

on H_T . Figure 4.2 shows the efficiency turn-on curves as a function of E_T^γ and H_T , parameterized with an analytic function in the form of:

$$\varepsilon = \frac{p_2}{2} \cdot \left(1 + \text{Erf} \left(\frac{x - p_0}{p_1 \cdot \sqrt{2}} \right) \right). \quad (4.1)$$

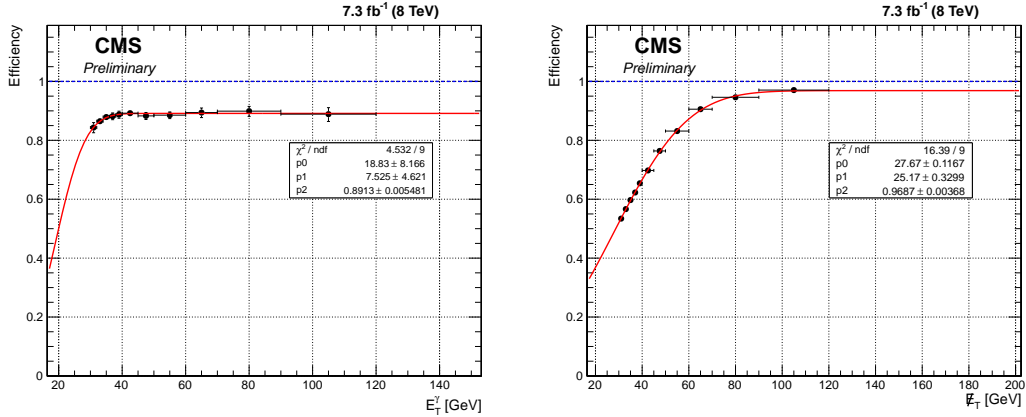


Figure 4.2: Trigger turn-on curves for E_T^γ and H_T . The parameterization of efficiency as a function of offline E_T^γ and H_T are also shown in the form of an analytic function fitted to the turn-on distributions.

In the offline selection, the events are required to have at least one well identified vertex with a distance less than 24 cm away from the nominal interaction point in z -direction and 2 cm away in the xy -plane. The vertex corresponding to the origin of the hard-scattering process with the largest value of $\sum p_T^2$ of all associated tracks is identified as the primary vertex.

Each selected event is required to have at least one photon candidate with $E_T^\gamma > 45$ GeV and $|\eta^\gamma| < 1.44$. The photon must also satisfy the following identification and isolation criteria: (a) to minimize the contribution from misidentified electrons, the shower is required to have no associated hits in the pixel detector, to be referred to as "pixel seed veto"; (b) the lateral extension of the shower, $\sigma_{inj\eta}$, measured in terms of the energy-weighted spread within the 5×5 crystal should be consistent with that of a genuine photon; (c) the ratio between the energy collected by the HCAL cells behind the supercluster and the energy collected by the supercluster is required to be less than 0.05; (d) the sum of the E_T of all photons reconstructed with the particle flow (PF) algorithm within a cone of $\Delta R = 0.3$, excluding a strip in η of 0.015 around the supercluster, is required to be less than $0.7 \text{ GeV} + 0.005 \times E_T^\gamma$; (e) the sum of the E_T of all charged hadrons reconstructed with the PF algorithm within a hollow cone of $0.02 < \Delta R < 0.3$ around the supercluster is required to be

less than 1.5 GeV; (f) the sum of the E_T of all neutral hadrons reconstructed with the PF algorithm within a cone of $\Delta R = 0.3$ around the supercluster is required to be less than $1.0 \text{ GeV} + 0.04 \times E_T^\gamma$. To account for the effects of overlapping proton-proton interactions (pileup), the total energy density in the event is computed using the FASTJET package [?] and is used to correct the isolation quantities. These pileup corrected isolation requirements correspond to a working point with a signal efficiency of approximately 85%. Furthermore, $R_9 > 0.9$ is also required to match the trigger requirements. The photon with the highest E_T in the event that satisfies all of the above requirements is selected as the photon candidate for the signal sample.

Anomalous signals in the ECAL, due to direct interaction of particles with the ECAL photodiodes, are rejected using additional shower shape requirements on the η and ϕ width of the shower. In addition, we reject showers that deposit more than 95% of their energy on the seed crystal [?].

To reduce the SM backgrounds arising from the leptonic decays of W and Z bosons, a lepton veto is applied. Events are rejected if they have at least one electron fulfilling a loose identification requirement [?] with $p_T^e > 10 \text{ GeV}$ and $|\eta^e| < 2.5$ (excluding the transition region of $1.44 < |\eta^e| \leq 1.55$) and are outside the cone defined by $\Delta R = 0.3$ around the photon candidate. Muons candidates which are identified using the PF algorithm using hits in the tracker and the muon systems are required to have $p_T^\mu > 10 \text{ GeV}$, $|\eta^\mu| < 2.1$, and $\Delta R(\gamma, \mu) > 0.3$ separation from the photon candidate. Events are rejected if any such muon is present in the event.

In addition to the selection requirements described above, the \cancel{E}_T is required to be greater than 40 GeV. This level of selection is referred to as the preselection and is applied for both the model independent analysis and the analysis of the SUSY benchmark model. The additional applied selection requirements differ between the two analyses.

To define the jet candidates, identification criteria are used to separate pileup jets from the jets originating from hard scattering. These identification criteria are based on the trajectory of tracks associated with the jets inside the tracker volume, the topology of the jet shape and multiplicity of the objects constituting these jets [?]. Only jets with $p_T^{jet} > 30 \text{ GeV}$ and $|\eta^{jet}| < 2.4$ and that fulfill the non-pileup identification requirements are considered in the event. These jets must not overlap with photon candidate within $\Delta R(\gamma, \text{jet}) < 0.5$. In the model independent analysis, events with 2 or more jets are rejected and, if there is a jet in the event, we also require that $\Delta\phi(\gamma, \text{jet}) < 2.5$.

In the analysis of the SUSY benchmark model, where no requirement is made on the jet multiplicity, more advanced selection is applied to reduce the background due to mismeasured \cancel{E}_T . Mismeasured \cancel{E}_T can arise from many sources, including limited \cancel{E}_T resolution, reconstruction and instrumental inefficiencies, and improper pattern recognition. Due to their large cross section the $\gamma +$ jets and multijet processes can contribute significantly to the background of this analysis, even though such events do not have genuine \cancel{E}_T . In order to minimize the contribution from these processes, we have used two different methods for identifying events with mismeasured \cancel{E}_T . The first one is the \cancel{E}_T significance method [?] which takes into account the reconstructed objects in each event and their known measurement resolutions to compute an event-by-event estimation of the likelihood that the observed \cancel{E}_T is consistent with zero. To complement this method we further developed the Missing H_T (MH_T) minimization method [?]. In the MH_T minimization method we first construct a χ^2 function with the form:

$$\chi^2 = \sum_{i=objects} \left(\frac{(p_T^{reco})_i - (\tilde{p}_T)_i}{(\sigma_{p_T})_i} \right)^2 + \left(\frac{\tilde{E}_x}{\sigma_{E_x}} \right)^2 + \left(\frac{\tilde{E}_y}{\sigma_{E_y}} \right)^2. \quad (4.2)$$

In the above equation, $(p_T^{reco})_i$ are the transverse momenta of the reconstructed objects that pass the above mentioned identification criteria, the $(\sigma_{p_T})_i$ are the expected resolutions of each object, the $\sigma_{E_{x,y}}$ are the resolution of the \cancel{E}_T projection along the x-axis and the y-axis and the $(\tilde{p}_T)_i$ are the free parameters allowed to vary in order to minimize the function. The first term of the equation is a scalar difference. The quantities $\tilde{E}_{x,y}$ are functions of the free parameters;

$$\tilde{E}_{x,y} = - \sum_{i=objects} (\tilde{p}_{x,y})_i \quad (4.3)$$

In events with no genuine \cancel{E}_T , the mismeasured quantities can be re-distributed back into the particle momenta, resulting in a low χ^2 value. On the other hand, in events with genuine \cancel{E}_T from undetected particles, the minimization generally will yield larger χ^2 values. For the analysis of the SUSY benchmark model, the recalculated $\widetilde{\cancel{E}_T} = \sqrt{\widetilde{E}_x^2 + \widetilde{E}_y^2}$, i.e., in which the original object momenta are replaced with those obtained with the χ^2 minimization, is required to be > 45 GeV and the probability value obtained from the χ^2 minimization is required to be less than 10^{-3} .

To further suppress multijet backgrounds, events are rejected if the scalar sum of transverse momentum of the identified jets (H_T) in the event is required to be greater

than 100 GeV. An additional requirement is made on the angle (α) between the beam direction and the major axis of the supercluster in order to reject photons that have showers elongated along the beam line which is characteristic of non-prompt photons.

Finally, the transverse mass, $M_T = \sqrt{2p_T^\gamma E_T(1 - \cos \Delta\phi(\gamma, E_T))}$, formed by the photon candidate, E_T and the angle between them, is required to be greater than 100 GeV. In order to easily interpret the results within the chosen benchmark model, we require the $E_T^\gamma < 60$ GeV.

The final list of advanced selection used in both the model independent analysis and the analysis of the SUSY benchmark model with the relative cumulative efficiencies of the selection requirements relative to the preselection is given on table 4.1.

Selection requirements	Model independent		SUSY benchmark model		
	$Z\gamma \rightarrow \nu\bar{\nu}\gamma$	$\gamma+\text{jet}$	$Z\gamma \rightarrow \nu\bar{\nu}\gamma$	$\gamma+\text{jet}$	$M_{\tilde{\chi}_1^0} = 120$ GeV
<i>Advanced selection</i>					
Number of jets < 2	0.909	0.769	-	-	-
$\Delta\phi(\gamma, \text{jet}) < 2.5$	0.834	0.262	-	-	-
Transverse mass > 100 GeV	-	-	0.867	0.292	0.829
$H_T < 100$ GeV	-	-	0.785	0.188	0.804
MH_T minimization: $\tilde{E}_T > 45$ GeV	-	-	0.761	0.071	0.743
MH_T minimization: $\text{Prob}(\chi^2) < 10^{-3}$	-	-	0.626	0.033	0.467
E_T^γ significance > 20	-	-	0.440	0.001	0.195
$\alpha > 1.2$	-	-	0.390	0.001	0.165
$E_T^\gamma < 60$ GeV	-	-	0.074	0.0002	0.106

Table 4.1: Summary of selection for both model independent analysis and analysis with SUSY benchmark model with the cumulative efficiencies of the selection requirements relative to the preselection for $Z\gamma \rightarrow \nu\bar{\nu}\gamma$, $\gamma+\text{jet}$ and $M_{\tilde{\chi}_1^0} = 120$ GeV.

4.3 Background estimation

The irreducible background for the $\gamma+E_T$ signal is the SM process $Z\gamma \rightarrow \nu\bar{\nu}\gamma$. Other SM backgrounds include $W\gamma$, $W \rightarrow e\nu$, $W \rightarrow \mu\nu$, $W \rightarrow \tau\nu$, $\gamma+\text{jet}$, multijet (referred to as QCD background) and diphoton events. Background events that do not come from collision processes are also considered in the analysis. These backgrounds can be divided broadly into three categories:

- Backgrounds estimated with Monte Carlo (MC) simulation: $Z\gamma \rightarrow \nu\bar{\nu}\gamma$, $Z\gamma \rightarrow \ell\ell\gamma$, $W\gamma$, $\gamma+\text{jets}$, $\gamma\gamma$;
- Collision backgrounds estimated using data: jets misidentified as photons and electrons misidentified as photons;

- Non-collision backgrounds estimated using data.

4.3.1 Background estimates from MC simulation

The $Z\gamma \rightarrow \nu\bar{\nu}\gamma$ is the irreducible background in this study. It is estimated from a MC sample generated with MADGRAPH [?] and processed with PYTHIA v6.426 [?] for showering and hadronization. To describe the topology of events in a realistic manner, up to two extra partons were included in the matrix elements during event generation. The final event yields are normalized using the next-to-leading-order (NLO) cross section calculated with the MCFM event generator [?]. The $W\gamma$ MC simulation was also produced with MADGRAPH, including up to two extra partons, and normalized using the NLO cross section calculated from MCFM.

The γ +jet is one of the most significant backgrounds in this analysis due to the presence of a genuine photon and the large production cross section. The events for this process are simulated using MADGRAPH, processed through PYTHIA and normalized using the LO cross section. The normalization of this background is then corrected using control sample in data for two different event classes: no-jet and one or more jets. The control sample in data is obtained using events collected with the prescaled single-photon trigger and with the E_T requirement reversed to ensure orthogonality to the signal phase space. Correction factors (C) are derived by normalizing the event yield in the simulation to match the data in the control region, separately for events with zero jets ($C = 1.7$) and one or more jets ($C = 1.1$). These correction factors are then used to normalize the γ +jet event yield from simulation in the signal region. An uncertainty of 16% is derived for these correction factors based on the difference between the corrected and uncorrected simulation and the relative fraction of zero jet ($\sim 10\%$ of the events in the control region) and one or more jet events.

The background estimate from the process $Z\gamma \rightarrow \ell\ell\gamma$ is obtained using MADGRAPH, and the background estimates from the processes $W \rightarrow \mu\nu$, $W \rightarrow \tau\nu$ are obtained using PYTHIA. These processes are found to contribute only to a small fraction of the total background prediction.

All simulated events are processed through a GEANT4-based simulation of the CMS detector [?] and the same reconstruction chain as the data. To take into account differences between data and simulation due to imperfect MC modeling, various scale factors (SF) are applied to correct the MC-based estimates. These SFs are defined as the ratio of the efficiency in data to the efficiency in simulation for a given selection. The SF for photon reconstruction and identification is estimated from $Z \rightarrow ee$ decays

with $R_9 > 0.9$ using a standard “tag-and-probe” method [?] and are listed in Table 4.2. The trigger efficiency measured in Section 4.2 is applied to the simulated samples.

Table 4.2: Scale factors for the photon identification

Variable	E_T^γ [30 – 40] GeV	E_T^γ [40 – 50] GeV	E_T^γ > 50 GeV
Pixel Seed Veto	0.995 ± 0.004	0.970 ± 0.016	1.012 ± 0.014
Photon ID ($0 < \eta < 0.8$)	0.996 ± 0.010	0.996 ± 0.010	0.996 ± 0.010
Photon ID ($0.8 < \eta < 1.5$)	0.996 ± 0.010	0.997 ± 0.010	0.997 ± 0.010

4.3.2 Jets Identified as Photons Background

The contamination from jets misidentified as photons is estimated by using a data control sample, enriched in QCD multijet events, defined by $\cancel{E}_T < 40$ GeV. In this sample we measure the ratio of events that pass the signal photon identification and isolation criteria (numerator selection) relative to those that pass a looser photon identification and isolation criteria but also fail one of the nominal isolation requirements (denominator selection). The sample of events passing the numerator selection includes genuine photons whose contribution must be subtracted to obtain the true ratio of misidentified jets. This contribution is estimated by fitting templates of energy-weighted shower widths of genuine photons (determined from MC simulation of γ +jets events) and misidentified photons (determined from an isolation sideband in data) to the candidate distribution. The final corrected extrapolation factor, shown in Figure 4.3, is then used to scale a sample of events in data which pass the denominator selection in addition to the other non-orthogonal event selections.

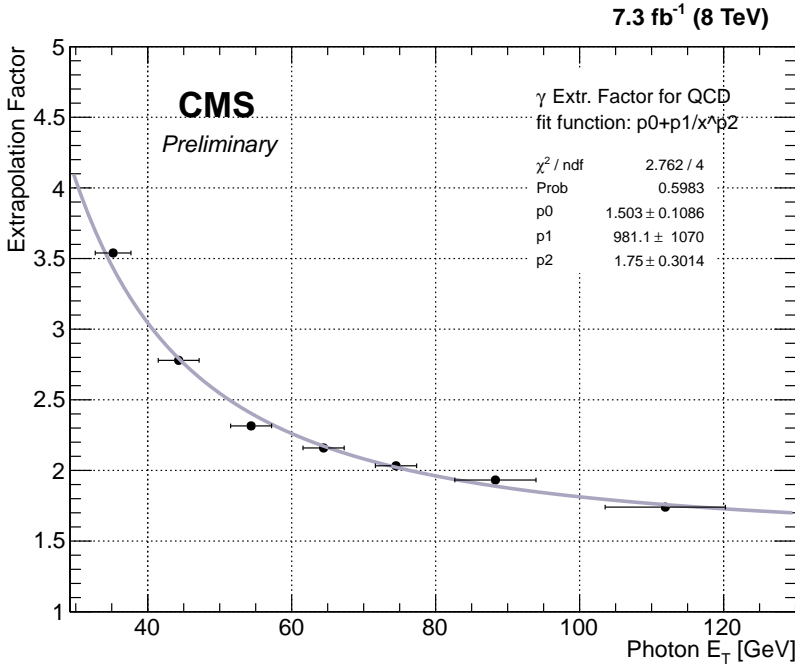


Figure 4.3: Ratio of number of photons passing signal like requirement relative to those satisfying a very loose identification and isolation selection and at the same time failing at least one of the isolation criteria as a function of E_T^γ .

The systematic uncertainty in this method is dominated by the choice of the isolation sideband region and is conservatively estimated to be 35% by varying the charged-hadron isolation in the sideband region definition. The other sources of systematic uncertainty are determined by varying the bin size of the templates, the E_T' selection for the control region, and the loose identification requirements on the photons, and are found to be comparatively small.

4.3.3 Electrons Identified as Photons Background

After the cuts for QCD-like events are applied, the background that arises from electrons-faking-photons becomes the dominant for the kinematic range of this analysis. We have developed a data-driven method to obtain an accurate estimation of the electron-faking-photon background. The main physical process behind this background is the $W \rightarrow e\nu$ production, which has a kinematic signature (fake photon E_T , transverse mass, etc) very similar to the signal sample and large production cross section.

The method for estimating the electron-faking-photon contamination in the signal sample was done by constructing a control sample, similar to the signal sample, but

enriched by electrons and not signal photons. This was achieved by reverting the pixel seed veto (PSV) in the photon ID requirements. The pixel seed veto cut is not the standard electron rejection tool in the $e - \gamma$ POG recommended photon ID; however, it has been shown to have a much smaller fake rate compared to the official electron rejection cut, the conversion safe electron veto. The PSV has been used in other photon-related analyses, such as the SUSY Photon and Exotica High Pt Monophoton analysis, in which the electron-faking-photon background is a dominant one.

After the control sample is created, it needs to be normalized by the number of expected electrons-faking-photons in the signal sample. This normalization can be obtained by the calculation of the fake rate of the PSV regarding electrons-faking-photons. It should be noted that this is not the fake rate of the full set of photon ID requirements, but only of the PSV cut.

Before describing the details of this method, the following definitions must be made:

- γ : Objects that pass the complete e/γ POG photon ID, including the PSV cut (photon object);
- γ_e : Objects that pass the photon ID with the PSV cut reversed (e -fake object);
- N_{γ_e} : Number of events in the control sample, which is made of γ_e ;
- ϵ_{γ_e} : Efficiency of accepting γ_e objects (including acceptance);
- ϵ_γ : Efficiency of accepting γ objects (including acceptance);
- $F_{e \rightarrow \gamma}$: Fake rate of the PSV cut for electrons-faking-photons.

Therefore, the number of electrons-faking-photons in the signal sample is given by

$$N_{e \rightarrow \gamma} = \frac{N_{\gamma_e}}{\epsilon_{\gamma_e}} \times F_{e \rightarrow \gamma} = N_{\gamma_e} \times R \quad (4.4)$$

$$R = \frac{F_{e \rightarrow \gamma}}{\epsilon_{\gamma_e}}. \quad (4.5)$$

This ratio (R) can be related to the PSV fake rate because, for the PSV cut, the efficiency and fake rate obey the following relation:

$$\epsilon_{\gamma_e} + F_{e \rightarrow \gamma} = 1. \quad (4.6)$$

Therefore,

$$F_{e \rightarrow \gamma} = \frac{R}{1+R}. \quad (4.7)$$

The ratio and the fake rate can be measured using a tag-and-probe method. This method was applied to the SinglePhotonParked signal dataset. Analyzing events in which the Z decays to electrons, we can reconstruct the number of events in four different cases:

- $Z_{e\gamma}$: one of the electrons of the Z decay is identified as an electron and the other is reconstructed as a photon object;
- $Z_{e\gamma_e}$: one of the electrons of the Z decay is identified as an electron and the other is reconstructed as an e -fake;
- $Z_{\gamma_e\gamma}$: one of the electrons of the Z decay is identified as an e -fake and the other as a photon;
- $Z_{\gamma_e\gamma_e}$: both electrons of the Z decay are identified as e -fakes;

Therefore, we can reconstruct the number of events in each Z peak case as:

$$N_{e\gamma} = 2 \times N'(Z \rightarrow ee) \times \epsilon_e \times F_{e \rightarrow \gamma} \quad (4.8)$$

$$N_{e\gamma_e} = 2 \times N'(Z \rightarrow ee) \times \epsilon_e \times \epsilon_{\gamma_e} \quad (4.9)$$

$$N_{\gamma_e\gamma} = 2 \times N'(Z \rightarrow ee) \times F_{e \rightarrow \gamma} \times \epsilon_{\gamma_e} \quad (4.10)$$

$$N_{\gamma_e\gamma_e} = N'(Z \rightarrow ee) \times \epsilon_{\gamma_e}^2, \quad (4.11)$$

where N_{xy} is the number of events of Z decaying to electrons when the electrons are reconstructed as x and y , and $N'(Z \rightarrow ee)$ overall number of expected $Z \rightarrow ee$ in the sample. The factors of two multiplying the first three equations are due to combinatorics.

With that system, we can infer that the calculation of the ratio can be performed in two ways:

$$R = \frac{F_{e \rightarrow \gamma}}{\epsilon_{\gamma_e}} = \frac{N_{e\gamma}}{N_{e\gamma_e}} = \frac{1}{2} \frac{N_{\gamma_e\gamma}}{N_{\gamma_e\gamma_e}} \quad (4.12)$$

The Z shape was obtained from the template of a DY $\rightarrow ee$ MC at generator level. This template was then convoluted with a Gaussian to simulate detector resolution effects. The parameters of the Gaussian were then fitted to the obtained invariant mass distribution from the different categories detailed above. For the calculation of

N_{xy} , the signal function was integrated in the $\pm 2\sigma$ region to obtain the number of signal events. The fits for the $Z \rightarrow e\gamma$ and $Z \rightarrow e\gamma_e$ cases can be seen in Fig. 4.3.3 and 4.3.3. The background shape for the fit was estimated by the convolution of an error function and a decaying exponential function (RooCMSShape). The background in the Fig. 4.3.3 is originated from the combinatorics of the electron plus non-resonant photon-like objects, such as real photons, jets faking photons and electrons faking photons originated from other interactions. Because the electron is most likely coming from the resonant Z production, the yield drops at lower values of $M_{e\gamma}$. The small disagreement between the fits and the data around 85 GeV comes from the trigger and selection acceptances, since our trigger photon object selection is 30 GeV and our probe selection p_T for this study is 35 GeV.

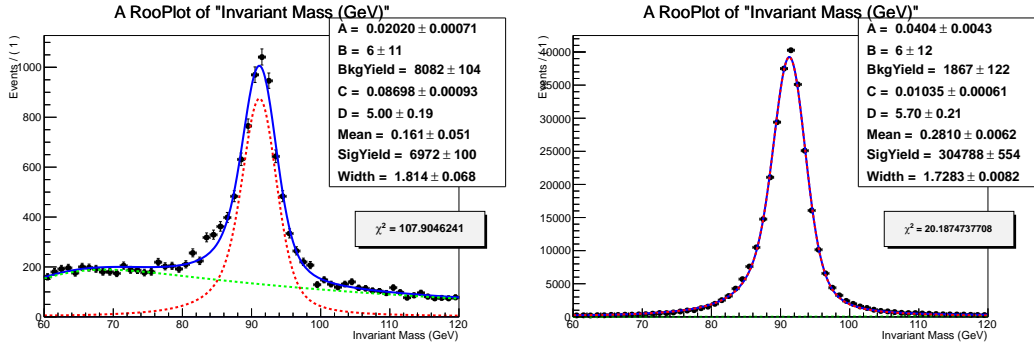


Figure 4.4: Fit of the Z invariant mass for the $Z \rightarrow e\gamma$ case and the $Z \rightarrow e\gamma_e$ case.

Assuming a Poissonian error on the signal integral result, the error on the ratio and fake rate can be estimated as:

$$\sigma_R = \sqrt{\frac{1}{N_{e\gamma_e}^2} \sigma_{N_{e\gamma}}^2 + \frac{N_{e\gamma}^2}{N_{e\gamma_e}^4} \sigma_{N_{e\gamma_e}}^2} \quad (4.13)$$

$$\sigma_{FR} = \frac{1}{(1+R)^2} \sigma_R. \quad (4.14)$$

With that, we obtain the following results:

$$R = (2.38 \pm 0.03)\% \quad (4.15)$$

$$F_{e \rightarrow \gamma} = (2.32 \pm 0.03)\%. \quad (4.16)$$

4.3.3.1 Electron \rightarrow Photon Fake Rate Dependencies on p_T , N_{Vtx} , N_{Trk}

It has been shown before, in the environment of the SUSY Photon analysis[?], that the PSV fake rate is dependent on variables such as the probe p_T , the number of tracks associated with the primary vertex and the number of reconstructed primary vertices in the event. The nature of the two last dependencies are deeply rooted in the track reconstruction and matching algorithm. Those details were documented in the Appendix of the SUSY Photon Analysis AN [?].

To check the dependency of the fake rate in the three variables mentioned, the fake rate was calculated in exclusive bins. In each bin, the signal template used was the corresponding bin in the MC signal sample. Each fit was done individually for every bin.

In Fig. 4.3.3.1, 4.3.3.1 and 4.3.3.1, we see how the PSV fake rate depends on the probe p_T , number of tracks associated with the primary vertex and the number of reconstructed primary vertices, respectively. The red line in each plot represents the fake rate obtained previously, assuming that there are no dependencies, with the entire invariant mass spectrum. For now on, this first result will be referenced as the flat fake rate.

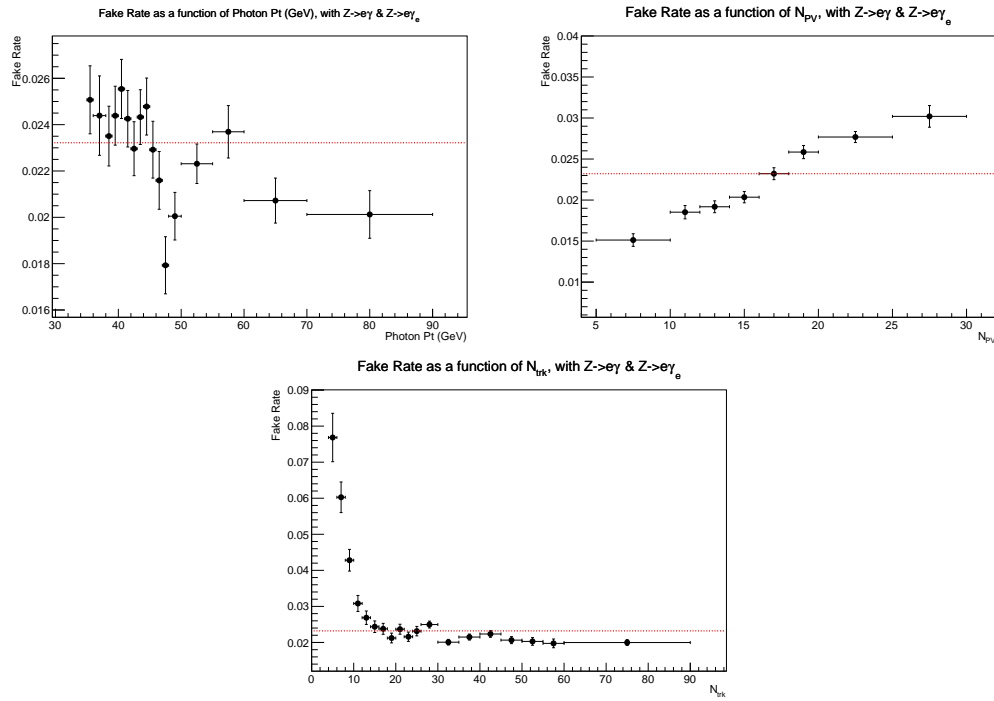


Figure 4.5: Fake rate vs. probe p_T , number of primary vertices and track multiplicity.

As shown in the plots, there is a non-trivial dependency of the fake rate on the variables probed. There are different ways to solve this feature. The most complete one would be to achieve a multi-parameter description of the fake rate, including a 3-dimensional function with dependencies of the fake rate on each variable. That, however, demands a thorough study of these dependencies and a functional form to perform this task. A second way would be to choose one of the parametrizations, including the flat one, and prescribe a systematical error to that assumption. To know how much one choice impacts the fake rate, we can look at the final result and observe how much the yields change with each assumption.

In our case, the final result is the control sample of photon-like objects that fail the pixel seed veto normalized by the fake rate, which represents the estimation of our electron faking photon contamination in the signal region. Figs. 4.3.3.1, 4.3.3.1 and 4.3.3.1 show the shape and yields of this control sample when normalized by the different parametrizations of the fake rate. When checking the differences in number of events of each bin, we see that they are all within 5% of each other, being higher around the p_T peak and approaching 0 for higher values. Therefore, it is safe to choose any specific parametrization and assume a systematic error of 5% on the number of events to make sure that the different assumptions are compatible. With these assumptions, we choose to use the flat parametrization, since it only involves one fit and it has been shown to be much more stable with respect to different fit functions, for signal and background.

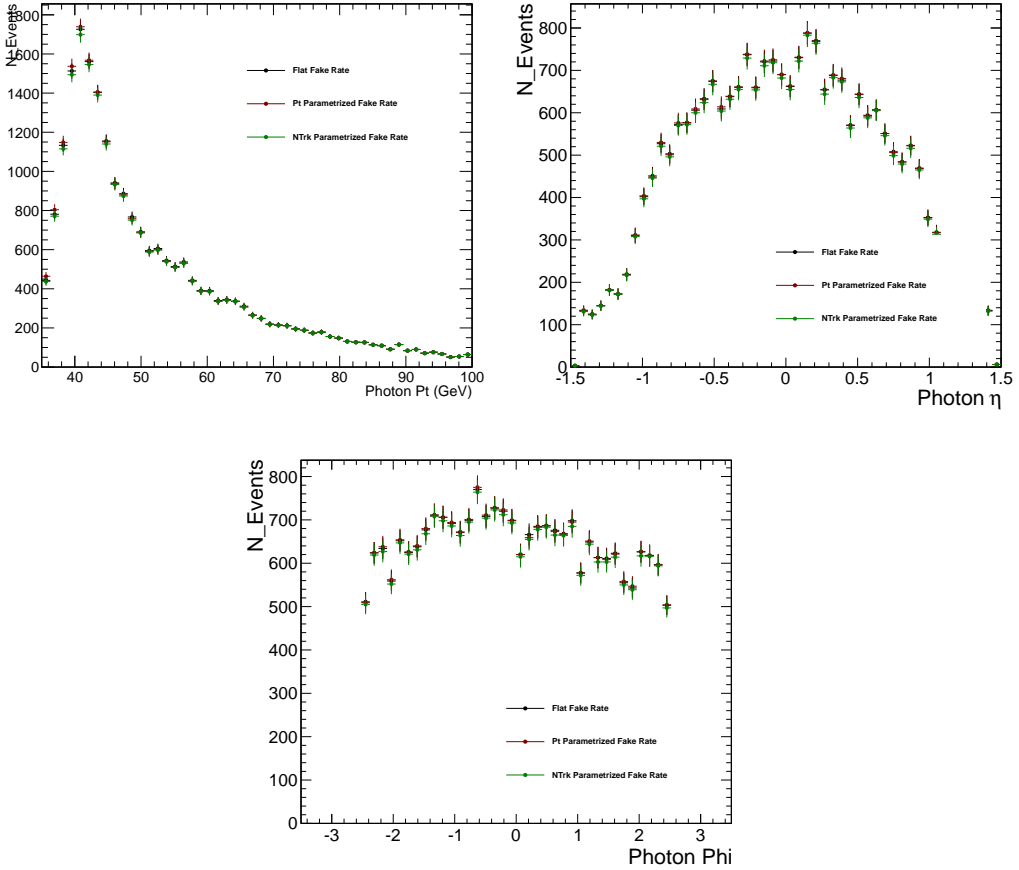


Figure 4.6: Control sample distribution of photon p_T , η and ϕ .

4.3.3.2 Closure Test for Electron \rightarrow Photon Fake Rate Measurment

As a closure test, we compare the generator-level fake rate to the fake rate as calculated by the method described above on MC (the reco-level fake rate) and check that they agree. For that, we used the Drell-Yan sample.

The generator-level fake rate is defined as:

$$F_{gen} = \frac{\# \text{Medium ID Photons \&& Matched to Gen Electrons \&& Pass the PSV}}{\# \text{Medium ID Photons \&& Matched to Gen Electrons}} \quad (4.17)$$

Here, the Medium photon ID is the one used on the analysis, including all the shower shape cuts to remove spikes and other contributions.

We compare the results of the two measurements, generator-level and reco-level, on the plots in Fig. 4.3.3.2, 4.3.3.2 and 4.3.3.2.

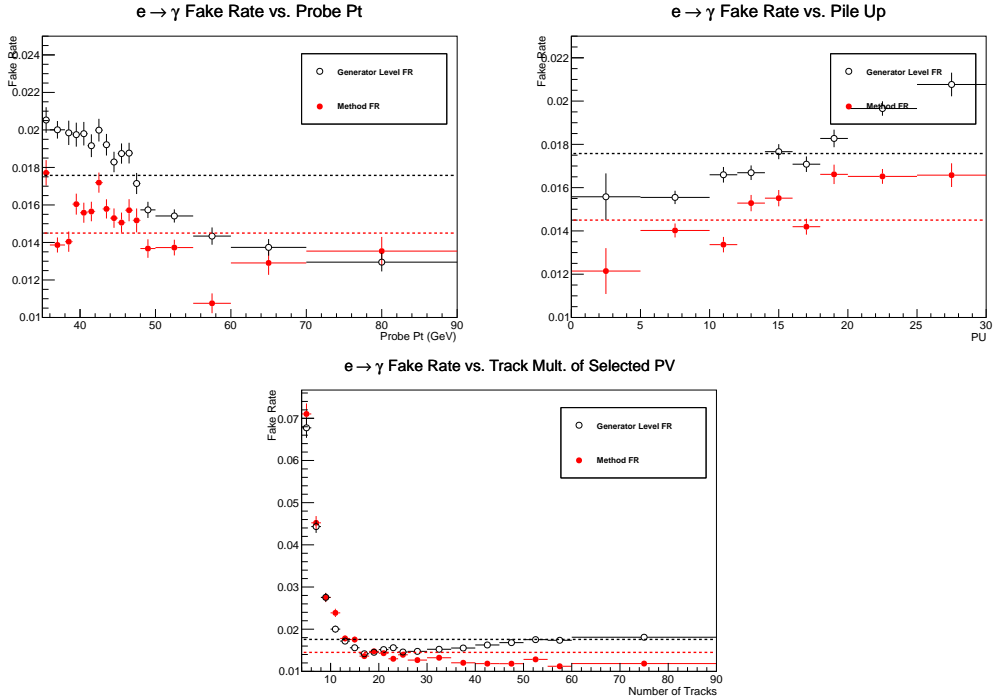


Figure 4.7: Closure test in probe p_T , number of reconstructed primary vertices and track multiplicity .

The lines represent the fake rate results from the flat assumption. For the generator-level fake rate, that is just the ratio on equation 4.17 on all events, while the parametrized fake rate is the ratio in each bin. As shown, there is a significant discrepancy between the two measurements. With those results, we can only say that the method is closed within 20%. The 20% number comes from the difference between the flat fake rates on generator-level and reco-level results.

We investigated the cause of this result and noticed that it comes about because of a "hidden" primary vertex matching on the tag-and-probe method. When using the tag and probe for electrons as tag and photons as probe, the photon ends up being matched to the hardest primary vertex because the electron, in the electron ID requirements, is indeed matched. When we require the invariant mass of the pair to be close to the Z peak, the electron PV matching is indirectly passed to the probe photon, since they must come from the same source. This requirement does not exist on the gen-level fake rate, which is basically a counting experiment.

The importance of the PV matching requirement comes about because of the nature of the $DY \rightarrow ee$ process. Since it is a low multiplicity process, i.e., there will not be many objects naturally from the hard scatter process, the Z might not come

from the hardest reconstructed primary vertex of the event. Therefore, when that happens, we measure the fake rate from a primary vertex that is not the hardest and, therefore, has fewer tracks than the primary vertex assumed. Since we know that the fake rate increases sharply when there are few tracks in the primary vertex, that explains why, in plot 4.3.3.2, there is an increase in higher values of NTrack - those are actually hard scatter events with few tracks that were mistakenly matched to the hardest PV.

To overcome these problems, we match the gen-level particles used for the gen-level fake rate to the hardest reconstructed primary vertex with the following cuts (from the muon ID POG recommendations):

- $Dz < 0.5$;
- $Dxy < 0.2$.

These variables are obtained directly from methods of the RECO::Candidate class inherited by the RECO::GenParticle. With that, we have the plots on Fig. 4.3.3.2, 4.3.3.2 and 4.3.3.2.

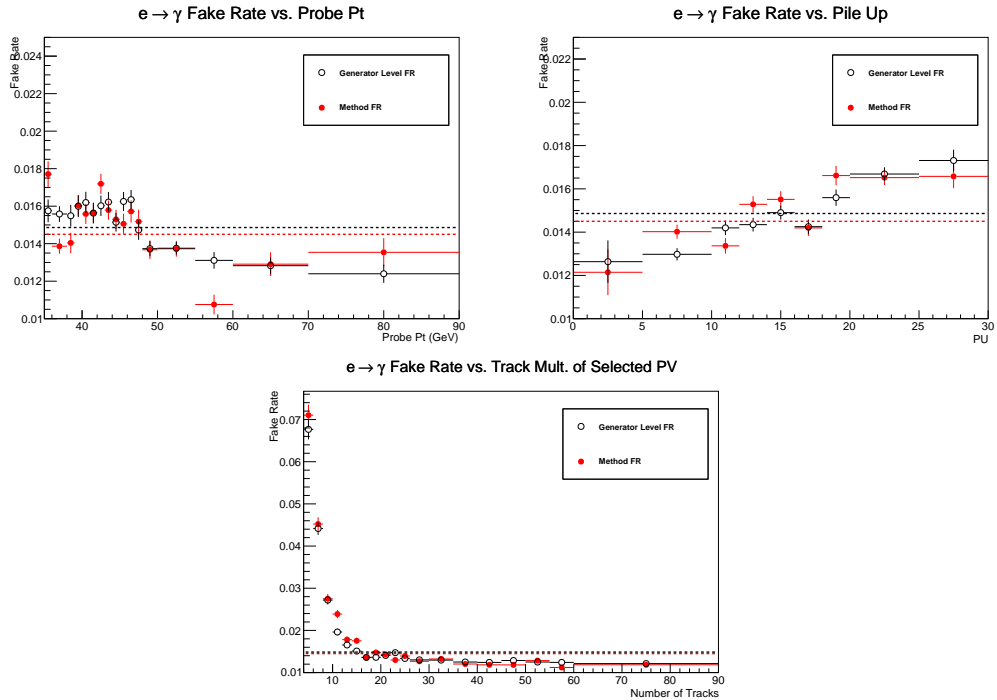


Figure 4.8: PV matched closure test in probe p_T , number of reconstructeed primary vertices and track multiplicity

We can see that the agreement between the gen-level and reco-level fake rates improves and the method closes within 4%.

4.3.3.3 Systematic Uncertainty on the Electron → Photon Fake Rate Measurement

Two of the main systematic errors have been discussed in the previous section:

- The flat assumption systematic error is found to be 5% on the number of events;
- The closure test systematic is found to be 4% on the value of the fake rate.

The remaining systematic uncertainty is related to the background estimation Fig. 4.4, i.e. the choice of the functional form to represent the background composition. Two choices were made for that estimation: a simple decaying exponential and the RooCMSShape. Looking at the full mass spectrum of the invariant mass, without parametrization, the amount of expected background is much smaller than the number of signal events. Because of that, we don't expect the fake rate to be very dependent on the functional shape of the background. Indeed, the difference in the calculated fake rate for the two functions is about 4%.

These systematic errors are assumed independent and should be added as such in the final number for the fake rate. They are, however, very small compared to the other sources of systematic errors in the analysis.

4.3.4 Non-collision background estimates from data

The search is susceptible to contamination from non-collision backgrounds which arise from cosmic ray interactions, spurious signals in the ECAL, and accelerator induced secondary particles (beam halo). These backgrounds have different arrival time distributions compared to prompt photons produced in hard scattering. To quantify the contamination due to these backgrounds a fit is performed to the candidate time distribution using background templates derived from the data. The contamination due to out-of-time background contribution is found to be negligible, therefore not included in the final event yield.

4.3.5 Background modeling validation

The background modeling is examined in several control regions. A control sample enriched in $W(l\nu)\gamma$ events is defined with inverted lepton-veto requirement in the preselection, thus selecting events with a loose e or μ . It is expected to be free of

any signal contamination due to the presence of a lepton. Another control sample enriched in γ +jet events is constructed by just requiring no selection other than the preselection requirements. Figure 4.9 shows the data vs SM expectation in the two control regions. The observed data and estimated SM backgrounds are found to be consistent both in yield and shape.

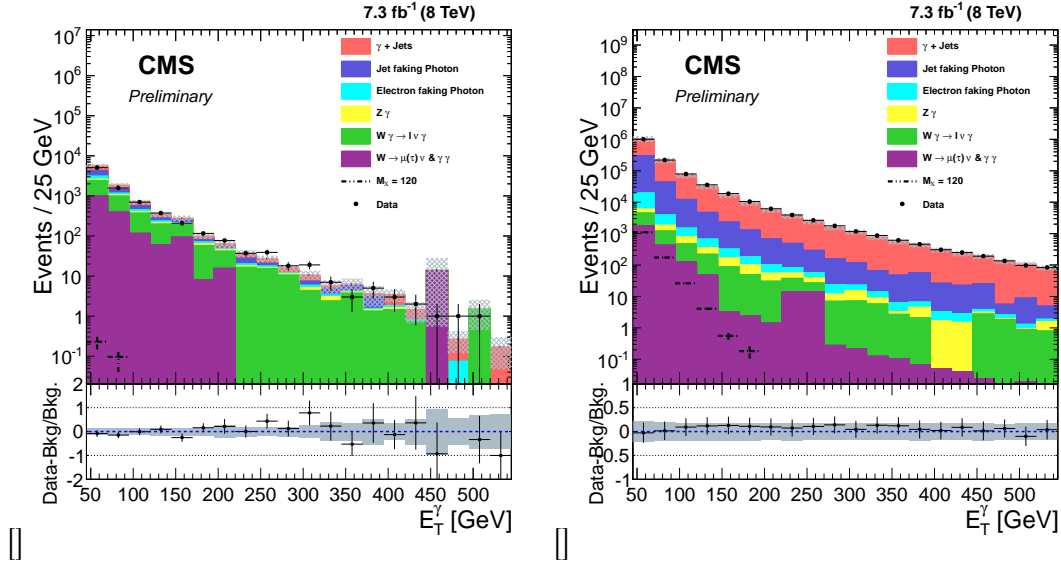


Figure 4.9: The E_T^γ distributions for data vs. SM expectation in a control region enriched by (a) $W(l\nu)$ events, and (b) γ +jet events. The bottom panels in each plot show the ratio of (data - background)/background and the gray band includes both the statistical and systematic uncertainty on the background prediction.

4.4 Systematic uncertainties

The experimental systematic uncertainties considered in the analysis are listed in Table 5.6. Since the model independent and model specific selections differ significantly, e.g. the inclusion of the mismeasured E_T reduction selection and E_T^γ window for the model specific results, the systematic uncertainties are evaluated separately for each selection. The systematic uncertainty associated with the measurement of the integrated luminosity is 2.6% [?]. The photon energy scale uncertainty [?] of about 1.0% affects the signal and background predictions by 4% for the model specific selection and by 0.5% for the model independent selection. Similarly, the jet energy scale uncertainty affects the signal and background predictions by 2 – 5% depending on the process and selection. When varying the photon or jet energy scales, the E_T is also recomputed. In addition, the systematic uncertainty associated with the jet energy resolution (0.5%) and unclustered energy (energy not contained within jets

or leptons or photons) scale (2%) are propagated to the E_T' and effect the signal and background predictions by 2 – 4%. The uncertainty due to the choice of parton density functions (PDFs) is estimated following PDF4LHC recommendations [?, ?, ?] and are found to be 10% for SUSY Higgs boson signal, and 4% for $Z\nu\nu\gamma$ and the $W\gamma$. An additional uncertainty due to the choice of renormalization and factorization scales is evaluated using MCFM and is found to be 3% for $Z\nu\nu\gamma$ and the $W\gamma$. As described in the previous section, a 16% uncertainty is applied to the γ +jet normalization due to the difference in the jet multiplicity distribution between the data and background prediction in the γ +jet control region. The uncertainty due to the pileup modeling is found to be 1% and is estimated by shifting the central value of the total inelastic cross section from 69.4 mb to 73.5 mb. Finally, the systematic uncertainties associated with backgrounds estimated from data have been applied as discussed in previous section.

Source	Signal	$\text{Jet} \rightarrow \gamma$	$\text{Electron} \rightarrow \gamma$	$\gamma + \text{jet}$	$Z\nu\nu\gamma$	$W\gamma$
PDF	10(0)	-	-	-	4(4)	4(4)
Luminosity	2.6(2.6)	-	-	2.6(2.6)	2.6(2.6)	2.6(2.6)
Photon energy scale $\pm 1\%$	4(0.5)	-	-	4(0.5)	4(0.5)	4(0.5)
E_T' energy scale	4(2)	-	-	4(2)	4(2)	4(2)
Jet energy scale	3(2)	-	-	5(5)	3(2)	3(2)
Pileup	1(1)	-	-	1(1)	1(1)	1(1)
$Z\nu\nu\gamma$ MCFM NLO calculation	-	-	-	-	3(3)	-
γ + jet normalization	-	-	-	16(16)	-	-
$W\gamma$ MCFM NLO calculation	-	-	-	-	-	3(3)
Jet $\rightarrow \gamma$ unc.	-	35(35)	-	-	-	-
Electron $\rightarrow \gamma$ unc.	-	-	6(6)	-	-	-

Table 4.3: Summary of all systematic relative uncertainties in percent on $A \times \epsilon_{MC}$ calculation for SUSY Higgs model (Model independent) selection.

4.5 Results

To evaluate the 95% confidence level (CL) limits on the new physics production cross section, an asymptotic CL_S method [?, ?] is used where the systematic uncertainties in the signal and background predictions are treated as nuisance parameters with log-normal prior distributions.

4.5.1 Model-independent limits

Due to the variety of signals which can contribute to this final state, we present results for a generic signal using the model-independent selection described in Section 4.2. Although this selection does not have as strong of discrimination power between signal like and background like events compared to the misreconstructed E_T' rejection

selections, it does have less model dependence. This is due to E_T significance and \tilde{E}_T minimization requirements having a non trivial efficiency dependence on the underlying event and observed E_T .

The total expected SM background and observed data events after the model-independent selection are found to be compatible within the systematic uncertainties. Table 4.4 shows a comparison of the event yields estimated for background processes and the observed data. Figure 4.10 shows the M_T and E_T distributions after the model-independent selection has been applied.

Process	# of Events
$\gamma + \text{jets}$	$(313 \pm 50) \times 10^3$
$\text{jet} \rightarrow \gamma$	$(906 \pm 317) \times 10^2$
$e \rightarrow \gamma$	$(1035 \pm 62) \times 10^1$
$W(\rightarrow \ell\nu) + \gamma$	2239 ± 111
$Z(\rightarrow \nu\bar{\nu}) + \gamma$	2050 ± 102
Other	1809 ± 91
Total background	$(420 \pm 82) \times 10^3$
Data	442×10^3

Table 4.4: Comparison of event yields for observed data and background, after the model-independent selection.

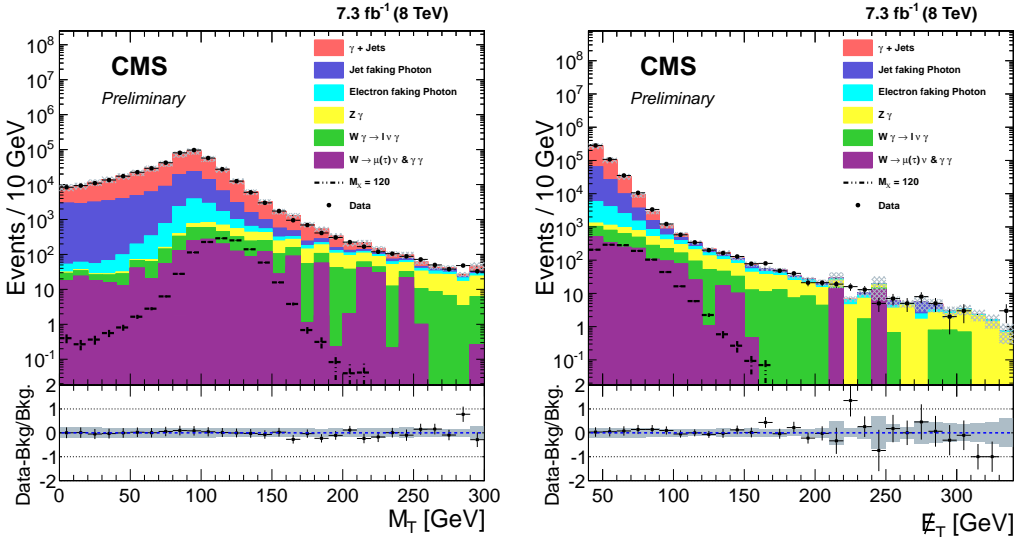


Figure 4.10: The M_T and E_T distributions for data, background estimates, and signal after the model-independent selection. The bottom panels in each plot show the ratio of (data - background)/background and the gray band includes both the statistical and systematic uncertainty on the background prediction.

Figure 4.11 shows the observed and expected model-independent 95% CL upper limits on $\sigma \times BR \times A \times \epsilon$ for different E_T' and M_T thresholds. The observed and expected limits are also shown in Fig 4.11(c) at a 95% CL for $M_T > 100$ GeV and as a function of E_T' .

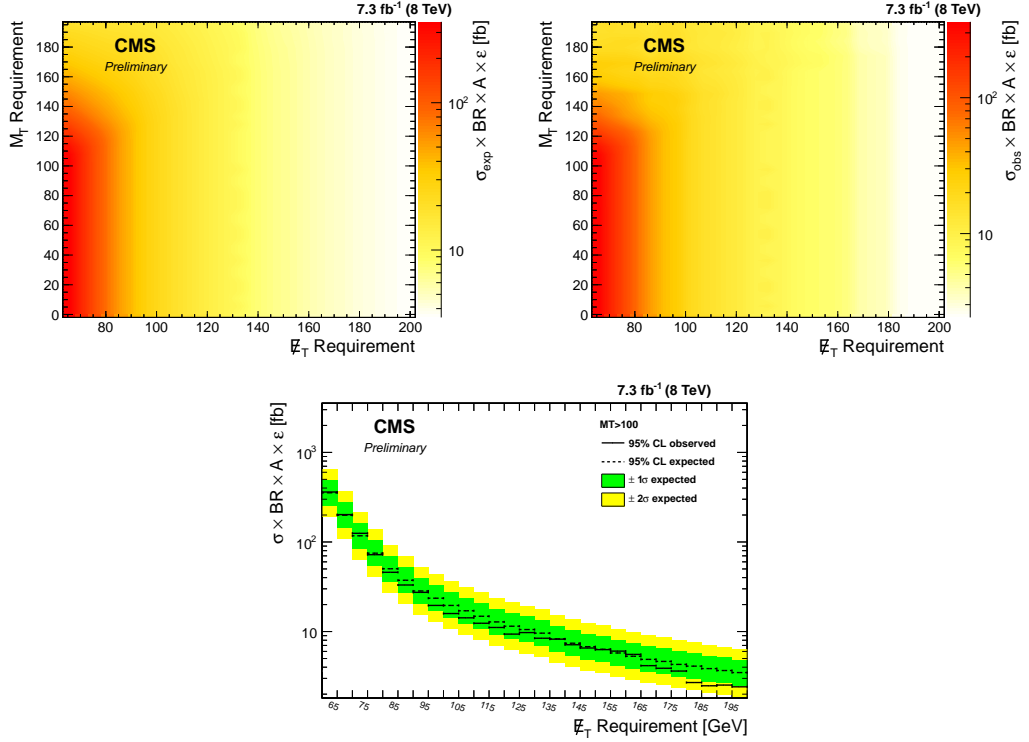


Figure 4.11: The expected (a) and observed (b) 95% CL upper limit on $\sigma \times BR \times A \times \epsilon$ for different M_T and E_T' thresholds and (c) for $M_T > 100$ GeV as function of the E_T' threshold.

4.5.2 Model-specific limits

The yields for supersymmetric decays of the Higgs boson ($h \rightarrow \tilde{G}\tilde{\chi}_1^0, \tilde{\chi}_1^0 \rightarrow \tilde{G}\gamma$) are acquired through imposing the model-specific selection described in Section 4.2. The yields for this selection are shown in Table 4.5. The 95% CL upper limits on the $\sigma \times$ branching ratio(BR) and $(\sigma \times BR)/\sigma_{SM}$, where σ_{SM} is the cross section for the standard model Higgs boson, are evaluated for different mass values of $\tilde{\chi}_1^0$ ranging from 65 GeV to 120 GeV and are shown in Fig. 4.12.

Process	Estimate
$\gamma + \text{jets}$	179 ± 28
$\text{jet} \rightarrow \gamma$	269 ± 94
$e \rightarrow \gamma$	355 ± 28
$W(\rightarrow \ell\nu) + \gamma$	154 ± 15
$Z(\rightarrow \nu\bar{\nu}) + \gamma$	182 ± 13
Other	91 ± 10
Total background	1232 ± 188
Data	1296
$M_{\tilde{\chi}_1^0} = 65 \text{ GeV}$	653.0 ± 77
$M_{\tilde{\chi}_1^0} = 95 \text{ GeV}$	1158.1 ± 137
$M_{\tilde{\chi}_1^0} = 120 \text{ GeV}$	2935.0 ± 349

Table 4.5: Expected (SM background) and observed event yields after the selection optimized for the supersymmetric decay of the Higgs boson ($h \rightarrow \tilde{G}\tilde{\chi}_1^0, \tilde{\chi}_1^0 \rightarrow \tilde{G}\gamma$) and the signal predictions correspond to $\text{BR}(H \rightarrow \text{invisible} + \gamma) = 100\%$.

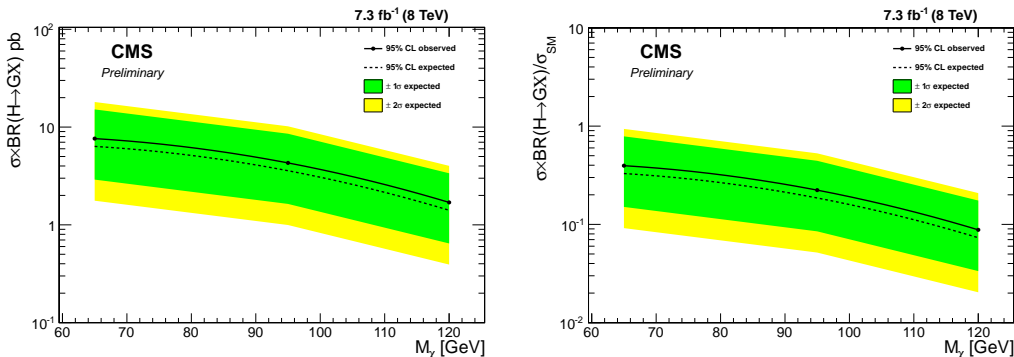


Figure 4.12: Expected and observed 95% CL upper limits on (a) $\sigma \times BR$ and (b) the ratio of this product over the SM Higgs production cross section as a function of different $M_{\tilde{\chi}_1^0}$ values. The uncertainty on the expected limit at 1σ and 2σ levels are shown as green and yellow bands, respectively.

4.6 Higgs Exotic Decays to Photons and MET Projection Studies

4.6.1 Introduction

Exotic decays of the Higgs boson can produce the final state consisting of two photons and missing transverse energy (E_T^{miss}) [?]. In the non-resonant case, the photons arise from opposite sides of the initial two-body decay: $h \rightarrow XX, X \rightarrow \gamma Y$, where Y is a stable neutral particle. For instance, such a decay can occur within general gauge

mediation models of supersymmetry, in which the X corresponds to a neutralino NLSP with mass less than half the Higgs mass, and the Y corresponds to a gravitino LSP [?, ?, ?]. In the resonant case, the photons are produced through an intermediate resonance: $h \rightarrow S_1 S_2$, with $S_1 \rightarrow \gamma\gamma$ on one side of the decay, while S_2 escapes detection, appearing as E_T^{miss} in the detector. The resonant signal benefits from a peak in the diphoton invariant mass spectrum. The Feynman diagrams for the non-resonant and resonant decays can be seen in Figure 4.13.

Previous searches for the $\gamma\gamma + E_T^{\text{miss}}$ final state in the low energy regime include searches for the non-resonant decay in the supersymmetric scenario described above. CMS and ATLAS have set upper limits on the branching ratio of this decay, with the Higgs boson produced in association with a Z boson [?] and through vector boson fusion [?].

In this study, we devise a search strategy for the $\gamma\gamma + E_T^{\text{miss}}$ final state, motivated by the exotic decays of the Higgs described above. We estimate the sensitivity of this search for 100 fb^{-1} of $\sqrt{s} = 14 \text{ TeV}$ pp data from the LHC.

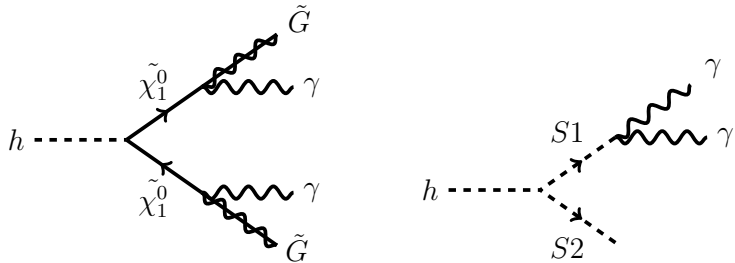


Figure 4.13: Feynman diagrams for the (left) the non-resonant and (right) resonant signal scenarios.

4.6.2 Methodology

4.6.2.1 Simulation Samples

Signal and background Monte Carlo (MC) samples were generated with Madgraph 5 [?] and hadronized with PYTHIA 8 [?], with the detector simulation provided by DELPHES 3 [?]. The samples were produced at $\sqrt{s} = 14 \text{ TeV}$.

The object reconstruction and identification are performed with DELPHES, according to the information provided in the detector configuration card. For the photons reconstruction and identification, we assume an efficiency of 95% in the electromagnetic calorimeter barrel ($|\eta| < 1.5$) and 85% in the endcap ($1.5 < |\eta| < 2.5$). We also impose an isolation cut on the photons by requiring all particle flow candidates

within a cone of $\Delta R < 0.3$ to have an energy ratio less than 0.1 with respect to the photon candidate. For muons, we assume an efficiency of 95% for the whole detector acceptance ($|\eta| < 2.5$). An isolation cut similar to the photons is also applied. Jets are reconstructed with the anti- k_T algorithm with $R = 0.4$.

Signal MC Samples

The signal for the non-resonant case was based on the supersymmetric cascade decay of the Higgs boson into two neutralinos, which subsequently decay into two gravitinos and two photons (Figure 4.13, left). This class of models has been implemented in FeynRules [?] and generated via Madgraph 5. We assume a gravitino mass close to zero, which is consistent with gauge mediated low-scale SUSY breaking models with $\sqrt{f} \approx \text{TeV}$ [?]. We simulate neutralino masses in the range [10, 60] GeV in steps of 5 GeV, with 100,000 events per mass point.

For the resonant case, we assume the Higgs boson decays into two scalar particles, S_1 and S_2 (Figure 4.13, right). One of the scalars then decays into two photons, while the other escapes detection. For this study, we assume the masses of these two particles are the same; this choice was made for simplicity, but for detailed studies, more combinations should be investigated. We generate samples with $M_1 = M_2 = [10, 60]$ GeV, in steps of 5 GeV, with 100,000 events per mass point.

We investigate the production of the Higgs boson through both gluon fusion and associated production with a Z boson (ZH), with the Z boson decaying to two muons. The inclusion of the dielectron decay of the Z can also be considered for future studies. A branching ratio of $B(H \rightarrow \gamma\gamma + E_T^{\text{miss}}) = 10\%$ is assumed for the signal. This value of the branching ratio was chosen to be within the current bounds on the Higgs boson width, yet close to the 8 TeV limits from the search for Higgs decays to the monophoton final state ($H \rightarrow \gamma + E_T^{\text{miss}}$) [?].

Background MC Samples

Although this analysis is not guaranteed to be entirely free from QCD multi-jet backgrounds, it has been shown in similar analyses (such as [?]) that it is possible to reduce the QCD to a sub-dominant contribution. As such, the remaining backgrounds for this analysis arise predominantly from the single boson ($\gamma/Z/W$) plus jets and diboson processes.

The background samples were modeled using the Snowmass LHE simulation samples [?]. They consist of single boson samples ($\gamma/Z/W$) with at least one jet and inclusive diboson ($\gamma\gamma/Z\gamma/W\gamma/ WW/ZZ/WZ$) samples. No pure QCD sample was produced for this study. The samples include both hadronic and leptonic decays of

the W and Z bosons. The cross subsections used for normalizing the single boson samples were estimated with MCFM [?], assuming an efficiency of 15% for the 1 jet requirement (obtained with Madgraph). For the diboson samples, the cross subsections used were estimated from the reference [?]. The cross subsections and number of events in the samples are shown in Table 4.7.

4.6.2.2 Event Selection

Trigger Projections

For the ZH channel, the trigger strategy is expected to be straightforward and can be based on the decay of the Z to two muons. On the other hand, triggering is one of the main challenges for the gluon fusion channel, since the final state consists of two soft photons plus missing energy. The standard triggers used for $H \rightarrow \gamma\gamma$ analyses typically have a diphoton invariant mass cut which makes it incompatible with the low energy spectrum of this analysis. However, we have identified three possible trigger strategies for this channel, based on unprescaled triggers used by the CMS experiment in Run-2:

- Asymmetric Diphoton Trigger: This trigger requires two photons with different E_T and trigger-level identification requirements, plus a diphoton invariant mass cut. This type of trigger usually has a non-negligible turn-on curve in the leading and subleading photon E_T .
- Symmetric Diphoton Trigger: This trigger requires two photons with the same E_T requirement, without any extra requirement.
- $\gamma + E_T^{\text{miss}}$ Trigger: This trigger requires only one barrel photon passing identification requirements and a E_T requirement that is usually higher than the previous two triggers. In addition, there is a calorimetric E_T^{miss} requirement. We expect non-negligible turn-on curves with respect to both photon and E_T^{miss} for this trigger.

The three triggers described here represent different selection strategies that were investigated and will be described below.

Offline Selection

The gluon fusion selection is based on the diphoton selection and must reflect the chosen trigger strategy, while maintaining a good signal efficiency. The ZH -produced signal events are tagged through the decay of the Z boson to muons, minimizing the

	gluon Fusion			ZH
Variable	Asymmetric $\gamma\gamma$	Symmetric $\gamma\gamma$	$\gamma + E_T^{\text{miss}}$	
Number of photons	> 1	> 1	> 1	> 1
$p_T(\gamma_1)$	$> 45 \text{ GeV}$	$> 40 \text{ GeV}$	$> 55 \text{ GeV}$	$> 20 \text{ GeV}$
$ \eta(\gamma_1) $	< 2.5	< 2.5	< 1.4	< 2.5
$p_T(\gamma_2)$	$> 30 \text{ GeV}$	$> 40 \text{ GeV}$	$> 20 \text{ GeV}$	$> 20 \text{ GeV}$
$ \eta(\gamma_2) $	< 2.5	< 2.5	< 2.5	< 2.5
$M(\gamma\gamma)$	$\in [15, 100] \text{ GeV}$	$< 100 \text{ GeV}$	$< 100 \text{ GeV}$	$< 100 \text{ GeV}$
E_T^{miss}	$> 90 \text{ GeV}$	$> 90 \text{ GeV}$	$> 90 \text{ GeV}$	$> 60 \text{ GeV}$
$M_T(\gamma\gamma, E_T^{\text{miss}})$	$< 140 \text{ GeV}$	$< 140 \text{ GeV}$	$< 140 \text{ GeV}$	$< 140 \text{ GeV}$
$\Delta\phi(\gamma\gamma, E_T^{\text{miss}})$	< 1.5	< 1.5	< 1.5	< 1.5
Number of leptons	< 1	< 1	< 1	2 muons
$p_T(\mu_{1,2})$	-	-	-	$> 20 \text{ GeV}$
$ \eta(\mu_{1,2}) $	-	-	-	< 2.5
$M(\mu\mu)$	-	-	-	$\in [75, 115] \text{ GeV}$
$M_T(\gamma\gamma + E_T^{\text{miss}}, \mu\mu)$	-	-	-	$> 400 \text{ GeV}$

Table 4.6: Analysis selection for the gluon fusion channel (for each trigger scenario) and the ZH channel.

largest backgrounds. The photon selection is chosen to maximize the signal acceptance in the ZH case, with E_T thresholds as low as possible. The final event selection requirements for the gluon fusion and ZH channels are summarized in Table 4.6. On this table, we use the following definitions for transverse mass:

$$M_T(\gamma\gamma, E_T^{\text{miss}}) = \sqrt{2E_T(\gamma\gamma)E_T^{\text{miss}}(1 - \cos(\Delta\phi(\gamma\gamma, E_T^{\text{miss}}))),} \quad (4.18)$$

$$M_T(\gamma\gamma + E_T^{\text{miss}}, \mu\mu) = \sqrt{2E_T(\gamma\gamma + E_T^{\text{miss}})p_T(\mu\mu)(1 - \cos(\Delta\phi(\gamma\gamma + E_T^{\text{miss}}, \mu\mu))).} \quad (4.19)$$

To exploit the topology of the resonant signature, we apply an additional requirement of a $\pm 10 \text{ GeV}$ mass window, in the diphoton invariant mass distribution ($M(\gamma\gamma)$), around the signal mass (M_1). The efficiencies for each individual process and the different searches, after the full selection (without the $M(\gamma\gamma)$ mass window requirement), are shown in Table 4.7.

For the ZH case, we also explore the strategy performed by CMS in their Run I result [?], in which one or more photons are required in the event, instead of two or more. In this case, we gain back the efficiency that is lost due to the inefficiency in reconstructing the subleading photon, which can have very low E_T . The selection is similar to what is described in Table 4.6, but without the $M(\gamma\gamma)$ cut or the mass window requirement for the non resonant topology. The other variables that use the diphoton information are instead reconstructed with the leading photon in the event.

Process	σ (pb)	$N_{\text{Generated}}$	gluon Fusion			ZH
			Asymmetric $\gamma\gamma$	Symmetric $\gamma\gamma$	$\gamma + E_T^{\text{miss}}$	
Backgrounds						
$\gamma + \text{Jets}$	1.0×10^5	5425448	1.9×10^{-6}	4.7×10^{-7}	8.9×10^{-7}	≈ 0
$Z + \text{Jets}$	0.94×10^4	1888446	5.6×10^{-4}	1.5×10^{-4}	5.0×10^{-5}	≈ 0
$W + \text{Jets}$	2.96×10^4	5263872	6.2×10^{-4}	1.9×10^{-4}	2.7×10^{-5}	≈ 0
$\gamma\gamma$	10.8×10^1	4268781	3.1×10^{-5}	1.0×10^{-5}	1.1×10^{-5}	≈ 0
$Z\gamma$	6.30×10^2	3406151	4.3×10^{-4}	1.4×10^{-4}	5.7×10^{-5}	≈ 0
$W\gamma$	1.03×10^3	5258034	1.4×10^{-4}	4.6×10^{-5}	5.4×10^{-5}	≈ 0
WW	1.24×10^2	8059829	2.6×10^{-1}	8.4×10^{-2}	9.8×10^{-5}	8.2×10^{-8}
ZZ	1.8×10^1	1101611	1.4×10^{-2}	4.7×10^{-3}	6.7×10^{-4}	7.3×10^{-6}
WZ	5.1×10^1	3319770	3.6×10^{-1}	1.2×10^{-1}	2.5×10^{-4}	2.9×10^{-6}

Table 4.7: Cross subsections, numbers of events generated per process, and selection efficiencies for background processes, for gluon fusion and ZH production mechanisms.

4.6.2.3 Background Estimation for Misidentified Photons

Background processes with mis-identified (or "fake") photons, such as jets and electrons misidentified as photons, that pass the final selection generally have very low efficiency at the LHC. Nonetheless, such backgrounds may be non-negligible since the production cross-subsections can be large. Such mis-identification rates are typically measured with data-driven methods at the LHC. Although this study was limited by MC statistics in measuring fake photon backgrounds, a method was developed to mitigate this problem, which we describe below.

The object reconstruction and selection is done at DELPHES level, where, given the photon identification requirements described in subsection 4.6.2.1, we obtain an associated fake rate. These fake rates are accounted for in the overall efficiencies in Table 4.7. In order to bypass the efficiency loss due to the small fake rates, we select jets and electrons as fake photon candidates. For the background processes with one prompt photon ($\gamma+\text{jets}$, $W\gamma$ and $Z\gamma$), we select one fake photon candidate. For the processes with no prompt photons ($W/Z+\text{jets}$, WW , WZ and ZZ), we select two fake photon candidates. No fake photon selection is done for the $\gamma\gamma+\text{jets}$ sample.

With the assumption of a flat fake rate for both jets and electrons, the fake photon candidates are randomly selected from the jets and electrons that passed the photon acceptance requirements. One extra assumption is that the electron-to-photon fake rate is set to be order of magnitude larger than the jets-to-photon fake rate. Therefore, electrons are set to have a probability of being selected to be a misidentified photon that is ten times higher than for jets.

After the choice of fake photon candidates, we calculate weights for the individual samples based on the E_T spectrum of the selected photons (prompt and fake) to match the spectrum found with the photon candidates reconstructed directly from DELPHES. This reweighting is done on the sum of E_T of the two leading photons for samples with at least one prompt photon, and on the E_T of the leading photon for samples with no prompt photon. An independent reweighting is also done in η . Both reweightings reflect the different reconstruction efficiencies and energy resolutions of objects that are not reconstructed as photons. After applying the weights, we observe a good agreement between the kinematic distributions of interest arising from photons reconstructed by DELPHES and from our fake photon candidates.

4.6.3 Results

We present the expected sensitivity of this search in terms of the necessary $h \rightarrow \gamma\gamma + E_T^{\text{miss}}$ branching ratio to reach a 5σ sensitivity for an assumed integrated luminosity of 100 fb^{-1} at $\sqrt{s} = 14 \text{ TeV}$, with the sensitivity defined as:

$$\mathcal{S} = \frac{N_{\text{Signal}}}{\sqrt{N_{\text{Background}}}}. \quad (4.20)$$

In Figure 4.14 (left), we show the signal efficiency for the different trigger selections presented and (right) the sensitivity plot for the gluon fusion case. This plot shows that, after the full selection, the performance of the triggers is comparable. Although it's safe to assume that a diphoton trigger with a low $M(\gamma\gamma)$ cut will be present in the future trigger menus of CMS and ATLAS, we choose to perform the analysis in the $\gamma + E_T^{\text{miss}}$ case. We make this choice as an effort to make the case for the existence of such a trigger strategy for the future LHC runs. While the diphoton triggers are designed with specific usages that are already well established, the $h \rightarrow \gamma\gamma + E_T^{\text{miss}}$ analysis could be viewed as a benchmark for the $\gamma + E_T^{\text{miss}}$ trigger for three reasons:

- It's a trigger that is already present at the LHC experiments, but can be retuned with a specific analysis as benchmark;
- A dedicated trigger for this analysis requiring two photons might not be as efficient at trigger level, given the soft spectrum of the second photon;
- This trigger can also be used for other exotic searches, such as the extension to low energies of the dark matter searches in the monophoton channel.

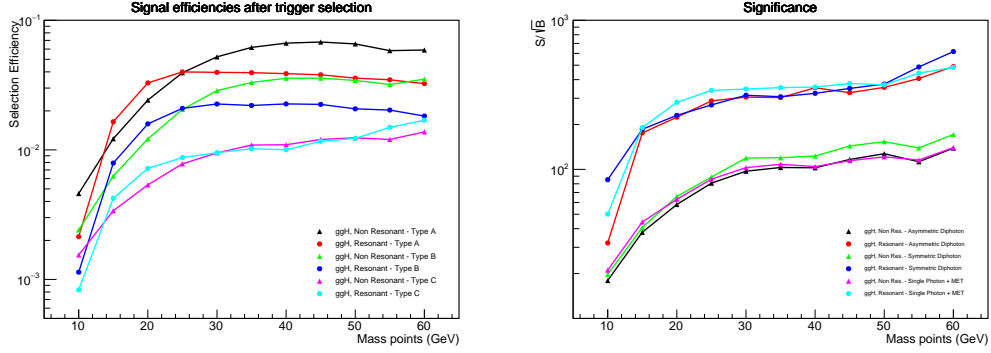


Figure 4.14: Signal efficiency (left) and significance (right) plots for different trigger scenarios in the gluon fusion analysis.

Plots of some of the discriminating variables can be seen on subsection ?? for both gluon fusion and ZH cases. The normalization reflects the expected number of events at $\sqrt{s} = 14$ TeV with a target luminosity of 100 fb^{-1} . The distributions are shown after the full selection, without the transverse mass and $\Delta\phi(\gamma\gamma, E_T^{\text{miss}})$ cuts. For the ZH case, the plots are also before the $M_T(\gamma\gamma + E_T^{\text{miss}}, \mu\mu)$ and $M(\mu\mu)$ cuts. For the gluon fusion channel, the single photon selection was used.

In Figure 4.15, on the left, we show the branching ratio of $h \rightarrow \gamma\gamma + E_T^{\text{miss}}$ needed for a significance of 5σ , assuming the Standard Model Higgs cross subsection, for the gluon fusion analysis (assuming the $\gamma + E_T^{\text{miss}}$ trigger strategy and selection). On the right, we show the branching ratio $h \rightarrow \gamma\gamma + E_T^{\text{miss}}$ needed for a significance of 2σ , which represents the 95% confidence level for exclusion, assuming SM ZH production. For the ZH case, we show the results for the strategies requiring at least one ($N(\gamma) \geq 1$) and at least two ($N(\gamma) \geq 2$) photons.

4.6.3.1 Systematic Uncertainties

While the uncertainties in the ZH channel is expected to be dominated by statistics, the gluon fusion channel is very sensitive to the systematic uncertainties associated with the background predictions. We estimate the effect of these uncertainties by parametrizing the sensitivity as:

$$\mathcal{S}_{sys} = \frac{N_{\text{Signal}}}{\sqrt{N_{\text{Background}} + \sigma_{sys} \times N_{\text{Background}}}}, \quad (4.21)$$

with σ_{sys} representing a source of uncertainty that does not scale with the amount of statistics. Figure 4.15 shows the effect on the 5σ branching ratios due to the addition of a 10% systematic uncertainty according to Eqn 4.21.

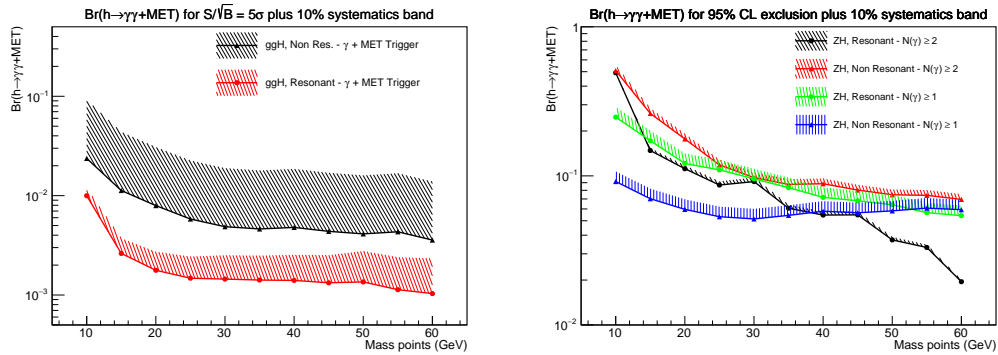


Figure 4.15: (Left) 5σ branching ratios for the gluon fusion channel, for resonant and non-resonant final states, using the $\gamma + E_T^{\text{miss}}$ trigger. (Right) Branching ratios for 95% confidence level exclusion in the ZH case, resonant and non-resonant topologies, requiring at least one photon ($N(\gamma) \geq 1$) and at least two photons ($N(\gamma) \geq 2$). The shaded areas correspond to a variation in systematics up to 10%.

References

Chapter 5

HH searches with photons and b-jets at CMS Run 2

5.1 Introduction

This Analysis Note describes the inclusive search for the double Higgs production process in the decay mode $\text{HH} \rightarrow b\bar{b}\gamma\gamma$ at $\sqrt{s} = 13 \text{ TeV}$, with 36.5 fb^{-1} from the 2016 data taking period. This analysis is based on the search at 8 TeV performed in the same final state, recently published by CMS in Ref. [?] (the internal CMS documentation of this analysis can be found in Refs. [?, ?]), and on the earlier 13 TeV search using 2015 data HIG-16-032.

Many theories beyond the SM (BSM) suggest the existence of new physics potentially manifested in the detection of a pair of Higgs bosons. The simplest signal we can look for is in the form of a resonant contribution to the invariant mass of the HH system (resonant search). If the BSM new particles are not directly detectable (either too heavy or too light to be in the HH invariant mass spectrum), but still couple to HH, their virtual contribution to the non-resonant HH production can still be measured (as shown, e.g., in Refs. [?, ?]). Additionally, the fundamental couplings of the Higgs boson to other SM particles (including itself) can be modified as well in BSM theories (as shown, e.g., in Refs. [?, ?]). Both of these cases can be studied via the non-resonant HH process.

In order to study the HH production, the Higgs bosons' final states must be carefully chosen. On one hand, the overall cross section of the process must be kept high enough for a good sensitivity. On the other hand, a good selection efficiency, online and offline, is important for a well performing analysis. This is achieved with the $b\bar{b}\gamma\gamma$ final state. The $\text{H} \rightarrow b\bar{b}$ leg provides a high branching ratio (57.7%), while the $\text{H} \rightarrow \gamma\gamma$ leg provides an efficient way to correctly identify the interesting events

and a high mass resolution. The total branching ratio of the $\text{HH} \rightarrow b\bar{b}\gamma\gamma$ channel is 0.26%.

The resonant analysis is dedicated to the search of a generic narrow width resonance (both spin-0 and spin-2). In this note, we will use a Warped Extra Dimensions (WED) theory¹ as a benchmark model for resonant HH search. It provides candidates for both spin-0 (radion) and spin-2 (graviton²) that decay into HH.

In the non-resonant search, we investigate explicitly the case of anomalous couplings in the Higgs boson potential, following the same model parametrization used in Ref. [?]. In the 13 TeV analysis however we study the parameter space of anomalous couplings using the approach suggested in [?], where physics benchmarks are defined based in basic signal kinematics. We also put limits in the Standard Model like HH production, a process that has a cross section of $\sigma_{HH}(\text{SMNNLO}) = 33.70 \text{ fb}$ at 13 TeV [?].

This note is organized as follows. In section 5.2, we describe the data and Monte Carlo samples used in the analysis, both for signal and background. In section 5.3.1, the online selection used in this analysis is described. Sections 5.3.2 and 5.3.3 are dedicated to the object reconstruction and selection in the analysis. The categorization procedure for the resonant and non-resonant analyses is defined in section 5.8.2. Section 5.5 described a new variable \tilde{M}_X that is a better proxy to the true 4-body invariant mass than the standard $M(jj\gamma\gamma)$, and how it is used to create signal mass dependent selections. The selection efficiencies are shown in section 5.6. The limits and signal extraction are defined in section 5.8, along with the signal and background modeling procedures. The systematic uncertainties for this analysis are defined in section 5.9. Finally, the results are shown in sections 5.10 and 5.11, for the resonant and non-resonant analyses respectively. Section 5.12 provides a summary of this analysis note.

5.1.1 Strategy Summary

The main strategy upgrades with respect to the Run-I analysis are:

- We make use of MVA ID for the photon selection, which improves the selection efficiency, see section 5.3.2

¹Based in the Randall-Sundrum (RS) setup [?].

²The graviton can be interpreted either as the first Kaluza-Klein (KK) excitation, or the graviton in the bulk RS scenario [?, ?, ?]

- Using \tilde{M}_X variable instead of 4-body mass, $M(jj\gamma\gamma)$. This allows to cancel the effects of the low dijet mass resolution (compared to $M(\gamma\gamma)$). uncertainties in the jet energy scale, see Section 5.5
- An improved version of the Combined Secondary Vertex algorithm (CSVv2) for b-tagging was developed in CMS.
- A new categorization method was developed to deal with signal categories and phase spaces with not enough events for a reliable background description.
- A dedicated b-jet energy regression is being developed for Run-II analysis, see Section 5.3.3.1.
- The main part of the analysis is performed in a framework based on top of the one developed by the $H \rightarrow \gamma\gamma$ group [?], so we benefit from the latest and greatest photon selection tools available.

In the new version of the analysis we also profit from a better description of the signal in the MC samples (Section 5.2), and a higher statistics of the MC events. The description of the simulated background is also improved. We observe a good agreement in the shapes of the basic distributions between data and MC in all control regions, see Section 5.7.

There are however a few new challenges in Run-II analysis. We utilize the double-photon trigger to select event for the analysis. Compared to the 8 TeV data-taking the E_T thresholds of the L1 seeds of those triggers were increased, which reduces the selection efficiency of the signal. Smaller distance parameter in the jet clustering algorithm is used by CMS ($D = 0.4$ in Run-II vs $D = 0.5$ in Run-I), which introduces a larger bias and decreased resolution in the reconstruction of the $M(jj)$ variable. Another challenge of the CMS running conditions in Run-II is higher pile-up environment, specially during the 2016 data taking.

With respect to the 2015 version of the analysis, many improvements have been implemented focusing on maximizing the S/B, given the larger amount of data available. New categorization schemes have been developed and the mass window selection has been re-optimized. A new training for the b jet energy regression has also been developed, with a better performance both regarding the jet energy scale and resolution.

5.2 Samples

All the MC samples used were processed centrally. As default for CMS, the signal samples use PDF4LHC15_nlo_mc_pdfs set [?, ?, ?, ?, ?, ?] in the four flavour scheme. The central value for the strong coupling is taken as $\alpha_s(m_Z) = 0.118$. This analysis aims to investigate data collected by CMS in 2016, therefore, all the samples mentioned below have been produced in the 80X CMSSW releases. The samples used in this analysis have also been pre-processed by the central $H \rightarrow \gamma\gamma$ analysis framework FLASHgg, in order to obtain and latest and greatest photon energy, resolution and ID used by the SM main analysis.

5.2.1 Signal MC: resonant production

To simulate the generic resonances we use `MG5_aMC@NLO` [?] at leading order. For the gluon fusion produced spin-2 resonance, we use the model for a KK-graviton in the bulk described on [?], which is an adaptation of the RS1 model of Ref. [?, ?], introducing the relevant coupling modifications. The model files can be found in [?] and its found to agree at the level of cross sections and branching ratios with the bulk WED scenario implemented by the authors of [?] on `CalcHep` [?] framework. To simulate the scalar resonance, we use the Higgs Effective Model [?] that can found in the `FeynRules` database [?].

The spin-0 and spin-2 resonances are simulated with masses: 250, 260, 270, 280, 300, 320, 340, 350, 400, 450, 500, 550, 600, 650, 700, 750, 800, 900, 1000 GeV, with 50K events each, assuming resonance width of 1 GeV. The samples corresponding to each signal point are:

- Spin-0: `/GluGluToRadionToHHTo2B2G_M-XXX_narrow_13TeV-madgraph`
- Spin-2: `/GluGluToBulkGravitonToHHTo2B2G_M-XXX_narrow_13TeV-madgraph`

The cross sections for the interpretations can be found here [?]. The `MG5_aMC@NLO` configuration cards used for the simulations are organized here [?].

5.2.2 Signal MC: nonresonant production

In the SM, Higgs boson pair production occurs predominantly by gluon-gluon fusion (GF) via an internal fermion loop. Since the Higgs boson couplings are defined by the particles masses, the top quark contribution is dominant, while couplings to light

quarks are negligible³. In the absence of new light states, the GF Higgs boson pair production at the LHC can then be generally described (to leading approximation) by five parameters controlling the tree-level interactions of the Higgs boson. The Higgs boson trilinear coupling and the top Yukawa interaction exist in the SM Lagrangian, where the former is given by $\lambda_{SM} = m_h^2/2v^2$, with v the vacuum-expectation value of the Higgs field. Deviations from SM values are parametrized with the multiplicative factors κ_λ and κ_t , respectively. The contact interactions of the Higgs boson with gluons and those coupling two Higgs bosons with two gluons or a top-antitop quark pair, which could arise through the mediation of very heavy new states, are instead genuinely not predicted by the SM; they can be parametrized by the absolute couplings c_g , c_{2g} , and c_2 . The relevant part of the Lagrangian then takes the form

$$\begin{aligned}\mathcal{L}_h = & \frac{1}{2}\partial_\mu h\partial^\mu h - \frac{1}{2}m_h^2 h^2 - \kappa_\lambda \lambda_{SM} v h^3 - \frac{m_t}{v}(v + \kappa_t h + \frac{c_2}{v} h h)(\bar{t}_L t_R + h.c.) \\ & + \frac{1}{4} \frac{\alpha_s}{3\pi v} (c_g h - \frac{c_{2g}}{2v} h h) G^{\mu\nu} G_{\mu\nu}. \quad (5.1)\end{aligned}$$

The different Feynman diagrams contributing to a di-Higgs boson signal in pp collisions at leading order (LO) are shown in Fig. 5.1. The simulation setup used in this paper was produced by the authors of [?], we use **MG5_aMC@NLO** as generator. The LO process is already at one-loop level; in the approach followed in [?], loop factors are calculated on an event-by-event basis with a **Fortran** routine on top of an *aMC@NLO* [?, ?] effective model;

In the Ref. [?] it was designed a method to partition the 5 dimensional parameter space in regions with similar LO kinematics. When the simulation was launched in the CMS system this work was in preliminary version, we had simulated the samples referent to the recommendations of its first version. The list of relevant parameters iused in each sample is in table 5.2. The **MG5_aMC@NLO** configuration cards used for the simulations are organized here [?]. Since then, the metric used by the method was improved and the parameter space scan extended, resulting in a new set of benchmarks, that can be found in the last ArXiV version of the mentioned paper, and as well in [?].

The full simulated samples can be found on DAS as:

- /GluGluToHHTo2B2G_node_X_13TeV-madgraph

³This assumption is motivated also in BSM theories where the Higgs sector is minimal (see also [?])

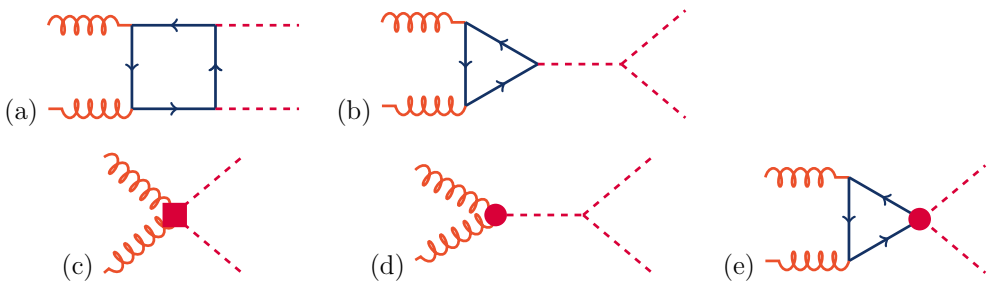


Figure 5.1: Feynman diagrams that contribute to Higgs boson pair production by gluon-gluon fusion at leading order. Diagrams (a) and (b) correspond to SM-like processes, while diagrams (c), (d), and (e) correspond to pure BSM effects: (c) and (d) describe contact interactions between the Higgs boson and gluons, and (e) exploits the contact interaction of two Higgs bosons with top quarks.

where the X ranges between 0 and 13. The $X = 0$ represents the point $(\kappa_\lambda, \kappa_t, c_2, c_g, c_{2g}) = (0, 1, 0, 0, 0)$ - when the process is induced only by the box diagram and the reminiscent correspond to the points listed in Tab. 5.2. The analytical formula that allows us to calculate cross sections for any point of the parameter space can be found here [?], and a handful script that calculates the cross sections point by point can be found here [?].

In the next session we explain how we had derived results in different benchmark points, based in the above full-simulated samples.

- Distributions at Gen level

5.2.2.1 Reweighting

We are considering a $2 \rightarrow 2$ process at leading order. The two Higgs bosons are produced with identical transverse momenta (p_T^H), and they are back-to-back in azimuth at this order (before a parton shower). The final state can then be completely defined by three kinematic variables, if we ignore the irrelevant azimuthal angle of emission of the bosons. Furthermore, one of the three remaining variables can be used to isolate all the information related to the PDF of the colliding partons, which is also irrelevant to the physics of the production process once one focuses on a specific initial state (the gluon-gluon fusion process). The variable factorizing out the PDF modeling can

Node	κ_λ	κ_t	c_2	c_g	c_{2g}
1	1.0	1.0	0.0	0.0	0.0
2	7.5	2.5	-0.5	0.0	0.0
3	15.0	1.5	-3.0	-0.0816	0.3010
4	5.0	2.25	3.0	0.0	0.0
5	10.0	1.5	-1.0	-0.0956	0.1240
6	1.0	0.5	4.0	-1.0	-0.3780
7	2.4	1.25	2.0	-0.2560	-0.1480
8	7.5	2.0	0.5	0.0	0.0
9	10.0	2.25	2.0	-0.2130	-0.0893
10	15.0	0.5	1.0	-0.0743	-0.0668
11	-15.0	2.0	6.0	-0.1680	-0.5180
12	2.4	2.25	2.0	-0.0616	-0.1200
13	-15.0	1.25	6.0	-0.0467	-0.5150

Table 5.1: Parameter values of the final benchmarks selected with $N_{clus} = 13$. The first cluster is the one that contains the SM sample.

be taken as the magnitude of the boost of the centre of mass frame as seen in the laboratory frame.

The two remaining variables, which provide direct information on the physics of GF HH production, can be chosen to be the invariant mass of the HH system (m_{HH}) and the modulus of the cosine of the polar angle of one Higgs boson with respect to the beam axis ($|cos\theta^*|$). Since we are using parton-level information, this last variable is equivalent to the polar angle in the Collins-Soper frame ($|cos\theta_{CS}^*|$) [?], which is commonly used in experimental analysis. The variables m_{HH} and $|cos\theta^*|$ can thus be used to fully characterize the final state kinematics produced by different choices of the value of anomalous Higgs boson (self-) coupling parameters.

By construction the full-simulated samples listed in Tab. 5.2 are good representatives of the kinematic space. Therefore, based in the generation level m_{HH} and $|cos\theta^*|$, those can be used to construct samples to any other parameter space point.

The procedure is made as follows:

- For each new parameter space point we perform a simulation in **MG5_aMC@NLO**, asking for N events;
- We construct two dimensional histograms in the generation level m_{HH} and $cos\theta^*$, with 20 GeV-wide bins in the m_{HH} and 0.2-wide bins in $cos\theta^*$ (without the moduli);
- We construct the same histogram with the sum of all the full simulated samples described in the last section (signal dataset);

- The new sample is constructed by weighting the signal dataset event-by-event by:

$$W_e = \frac{New_{ij}}{D_{ij}}, \quad (5.2)$$

where (ij) specify the bin in which the event e belongs and New_{ij} (D_{ij}) the number of events of the new signal sample (signal dataset) in that bin.

We make reweighted samples for three types of theory scans:

- A plain scan in κ_λ , while all the other parameters are kept as in SM ($\kappa_t, c_2 = c_g = c_{2g} = 0$), where the gen-level histograms are made from 50,000 events
- Another set of samples that we will use to calculate the shape systematics necessary to extrapolate the limits in the benchmarks to an extended part of the parameter space (see Sec. ??).

Benchmark	κ_λ	κ_t	c_2	c_g	c_{2g}
1	7.5	1.0	-1.0	0.0	0.0
2	1.0	1.0	0.5	-0.8	0.6
3	1.0	1.0	-1.5	0.0	-0.8
4	-3.5	1.5	-3.0	0.0	0.0
5	1.0	1.0	0.0	0.8	-1
6	2.4	1.0	0.0	0.2	-0.2
7	5.0	1.0	0.0	0.2	-0.2
8	15.0	1.0	0.0	-1	1
9	1.0	1.0	1.0	-0.6	0.6
10	10.0	1.5	-1.0	0.0	0.0
11	2.4	1.0	0.0	1	-1
12	15.0	1.0	1.0	0.0	0.0
SM	1.0	1.0	0.0	0.0	0.0

Table 5.2: Parameter values of the twelve benchmarks and the Standard Model point.

5.2.2.2 Non-resonant Vector Boson Fusion

For the 2016 version of the analysis, one non-resonant VBF sample was also produced centrally with the Standard Model coupling parameters. The MiniAOD version of this sample can be found on DAS under: /VBFHTo2B2G_CV_1_C2V_1_C3_1_13TeV-madgraph/RunIISummer16MiniAODv2-PUMoriond17_80X_mcRun2_asymptotic_2016_TrancheIV_v1/MINIAODSIM

5.2.3 Background MC

Even though the signal extraction and background modeling of this analysis are performed based on data, background Monte Carlo samples are used to validate the simulation of our signal description and to develop the analysis. The main backgrounds for the $b\bar{b}\gamma\gamma$ final state come from either well-isolated photons coming from the hard scatter (prompt photons) or isolated photons reconstructed due to very collimated $\pi^0 \rightarrow \gamma\gamma$ decays fragmented from jets (fake photons). These backgrounds are the same as the ones to the SM $H \rightarrow \gamma\gamma$ analysis, and a more complete description of the samples used can be found in the $H \rightarrow \gamma\gamma$ AN [?, ?].

We can classify these backgrounds with respect to the number of prompt and fake photons in the selected diphoton candidate. The prompt-prompt background events are simulated with the Sherpa generator; it includes the born processes with up to 3 additional jets at LO accuracy as well as the box processes at LO. The prompt-fake and the fake-fake contributions are simulated with PYTHIA8, with a "Double-EM Enriched" filter⁴ applied during production to improve the samples selection efficiencies. Additionally, a sample of Drell-Yan events decaying into electrons, simulated at NLO with AMC@NLO, is used, although its final contribution to the event yield is minimal due to the $M(\gamma\gamma) > 100$ GeV selection cut.

5.2.4 Data

The data samples used in this analysis correspond to approximately 36.5 fb^{-1} of data collected in 2016, reconstructed with the 80X CMSSW release.

5.3 Analysis objects and selection

This analysis uses general purpose reconstruction of the photons and jets for which we have brief descriptions below.

5.3.1 Triggers And Pre-Selection

Exploiting the high online performance of the CMS ECAL to reconstruct photons and electrons, the dataset used in this analysis is constructed with a selection that requires two photons at High Level Trigger (HLT) level.

⁴it requires a high p_T and well isolated photon-like signal (electromagnetic activity) coming from photons, electrons, or neutral hadrons)

For the 2016 data taking period, the online strategy was based on a single HLT trigger path:

- HLT_Diphoton30_18_R9Id_OR_IsoCaloId_AND_HE_R9Id_Mass90;

In order to achieve a good data/simulation comparison, a pre-selection that is tighter than the online selection is applied on data and Monte Carlo. This pre-selection is described on table 5.3. It is based on shower shape variables ($R9$, the ratio between the energy deposited on a 3x3 ECAL crystal matrix around the most energetic crystal in the supercluster, and the supercluster energy), isolation variables (charged hadron isolation, CHI, the sum of all charged hadron particle flow candidates energies inside a cone of $\Delta R < 0.3$ around the photon axis), identification variables (H/E, the ratio between the photon's energy deposit on HCAL and on ECAL), and kinematic variables (E_T and the photon supercluster η). Only events that have at least one diphoton candidate passing the pre-selection requirements are considered in the analysis.

Requirements	Leading Photon	Subleading Photon
E_T	30 GeV	20 GeV
$ \eta $	< 2.5 and outside 1.442	$ \eta < 1.566$
Shower shape and Isolation	$R9 > 0.8$ or $CHI < 20$ or $CHI/E_T < 0.3$	
Identification		H/E < 0.08

Table 5.3: Trigger based pre-selection applied on diphoton candidates.

The central $H \rightarrow \gamma\gamma$ analysis provides scale factors and uncertainties related to those scale factors due to this HLT selection, which we also apply in the analysis and take into account in our final list of systematics.

5.3.2 Photons

The kinematic requirements applied on the photons, after the diphoton candidates have passed through the event pre-selection (see Section 5.3.1), is analogous to the ones used in the SM $H \rightarrow \gamma\gamma$ analysis. The selection is as follows:

- Leading photon $E_T > 30$ GeV, trailing photon $E_T > 20$ GeV;
- Leading photon $E_T/M(\gamma\gamma) > 1/3$, trailing photon $E_T/M(\gamma\gamma) > 1/4$;
- $100 < M(\gamma\gamma) < 180$ GeV.

Additionally, a photon identification requirement is applied to the photons.

In the 13 TeV run of 2016 we have at least three different identification algorithms for photons:

- General purpose cut-based ID developed by the CMS EGamma group [?]. The ID makes use only of a few variables: H/E, σ_{inj} and isolation. This type of ID was used in Run-I analysis.
- General purpose MVA ID developed within the EGamma group [?]. It utilizes the information from many shower shape variables at ECAL, as well as isolation information.
- MVA ID developed by the $H \rightarrow \gamma\gamma$ search group [?] (ref to be updated). It is similar to the one developed in EGamma group, but uses a slightly different set of input variables.

We have chosen to use the EGM MVA photon ID on this analysis. The WP chosen is one that provides 90% signal efficiency for the photon selection (provided centrally). The scale factors used to ensure data/MC agreement in the selection efficiency are also applied (provided centrally). Additionally, an electron veto is applied to avoid background with electrons faking photons (scale factors provided centrally also applied).

===== OLD =====

Currently (as of January 2016), the available samples processed by the $H \rightarrow \gamma\gamma$ group only have stored their own training of the photon MVA ID. We have chosen working points that ensure that the resonant low mass samples have a 90% efficiency both in the barrel and the endcap ECAL regions.

ECAL Region	Hgg MVA Selection
EB	0.07
EE	-0.03

Efficiencies of the leading photon to pass the ID criteria, as a function of the photon transverse energy, are shown in Figure 5.2. Only photons matched to gen-level prompt photons are used.

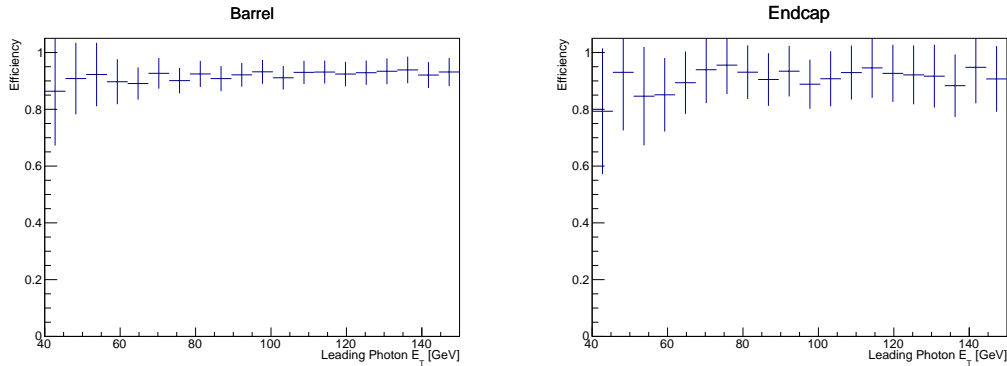


Figure 5.2: Efficiencies of the leading photon to pass the ID criteria, as a function of the photon transverse energy, for photons in the barrel and endcap regions of ECAL.

5.3.2.1 Fake Photon Control Region

A control region is created by selecting diphoton candidates with one photon that passed the ID requirement and one that didn't. All the other selections remain the same, and the procedure to select such diphoton candidate is the same as in the signal region.

This control region is used on the analysis to perform the closure test on the background modeling.

5.3.2.2 Vertex

Inheriting from the main $H \rightarrow \gamma\gamma$ analysis, we use the vertex that gives the highest $H \rightarrow \gamma\gamma$ vertex MVA score. Because there are additional jets in the event, picking this vertex has a very small mismatch efficiency. Only in less than 0.1% of the events, the chosen vertex is different from the vertex associated to the simulated event.

5.3.2.3 Gain Switch

Due to the ECAL slew rate issue discovered during the 2016 data taking, we investigated the fraction of selected events in our blinded signal region with photons that go through gain switches. The plots on Figure 5.3 show, in bins of \tilde{M}_X , the fraction of events with at least one of the photon candidates going through gain switches (to gain 1, gain 6 or both). These results show that, for the high mass region, around 20% of our events are affected by gain switches. This non-negligible rate means that the analysis needs to use the re-MiniAOD Moriond17 campaign, which has the slew rate effect mitigated.

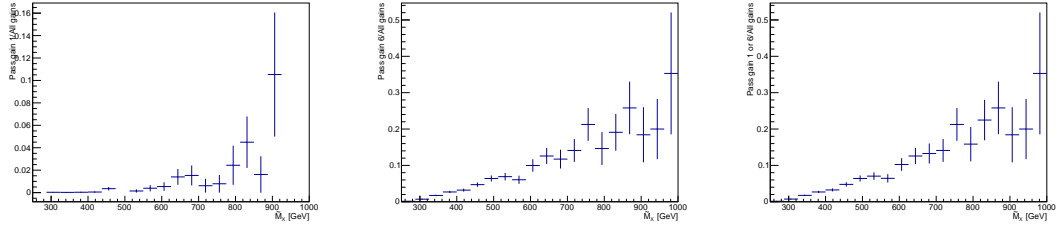


Figure 5.3: Fraction of events with photon candidates going through gain switch.

5.3.2.4 Regression

A new version of the photon energy regression has been trained (with 80X MC and 2016 data taking conditions). We compared this new regression to the previous training (74X), as seen in the plots of Figure 5.4 for three different resonance mass points. The difference observed is not large enough for this analysis to be affected, so the regression version used is 74X (following main $H \rightarrow \gamma\gamma$ analysis).

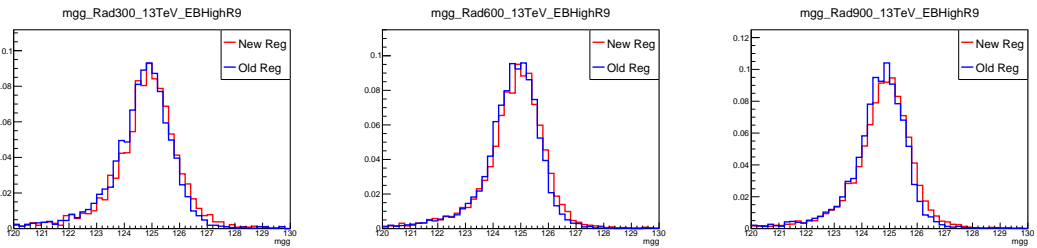


Figure 5.4: $M(\gamma\gamma)$ reconstructed with different versions of the photon energy regression.

5.3.3 Jets

Note: the jets selection has not changed with respect to the 2015 analysis.

The jets in Run-II at CMS are reconstructed using anti- kt algorithm with the distance parameter $D = 0.4$. This was a change with respect to the parameter distance of $D = 0.5$ in Run-I due to increased pile-up in Run-II data taking. This change results in smaller $M(jj)$ resolution but induced a bias towards lower energy of the signal $M(jj)$ peak, because less energy is clustered in a jet. This effect can be seen in figure 5.5 of the $M(jj)$ distribution for reconstructed jets matched to generator-level jets (that come from the Higgs) from the Radion sample of $M = 300$ GeV.

We use the *Loose ID* criteria to select the jets, which is described in Ref [?].

The jet candidates in the event, after passing the aforementioned ID, must have $p_T > 25$ GeV and $|\eta| < 2.4$ (so that they are within the tracker of CMS and can be

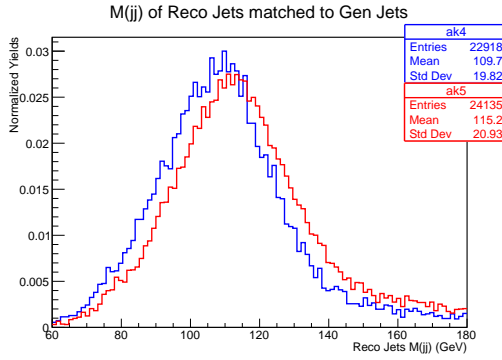


Figure 5.5: Difference between jet reconstruction used in Run I (red) and Run II (blue)

tagged as coming from b quark). The jets must also be outside the photon cone with a $\Delta R(j, \gamma) > 0.4$. Dijet objects are then created and only dijets with $M(jj)$ between 60 and 180 GeV pass the selection. If more than one dijet has passed those criteria, the dijet with two jets with highest b-tagging score (see sec. 5.3.3.2) are selected as the dijet candidate.

5.3.3.1 Jet energy regression

In addition to the misfortune of a small distance parameter of the jet reconstruction algorithm, the energy of the jets coming from b -quarks can not be fully reconstructed due to neutrinos escaping the detector. In order to improve the $M(jj)$ resolution and gain in S/B discrimination, we employ jet energy regression technique based on MC simulated samples. We use implementation of the regression in TMVA package and train it on $X \rightarrow HH \rightarrow b\bar{b}b\bar{b}$ MC samples. Input variables to the training include jet kinematics, energy deposited in the calorimeter, vertex information, and also the missing transverse energy in the event (MET). Performance of the regression was validated on MC signal samples as well as in data, based on $Z(\ell\ell) + bb$ events, where the p_T balance was checked of the $p_T(\ell\ell)$ and $p_T(bb)$. Detailed information about the training and its validation can be found in Appendix ??.

The effect of the regression on the analysis can be summarized in figures 5.6. While data in the photon control region remains the same, the $M(jj)$ spectrum in the signal is shifted towards higher values (scale correction). This leads to an improvement in the analysis due to the gain in signal efficiency.

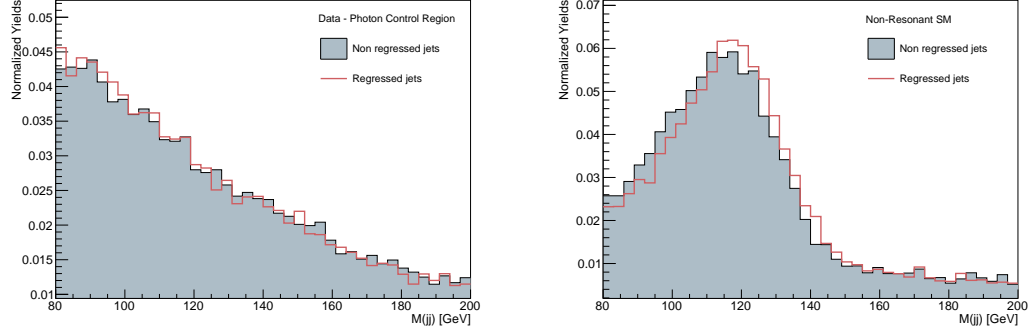


Figure 5.6: Comparison between dijet invariant mass with regressed jets and without for data in photon control region and signal MC. WARNING - THESE ARE 2015 PLOTS, NEED TO UPDATE

5.3.3.2 B-tagging

We utilize the *Combined Secondary Vertex* algorithm (CSVv2) for tagging b-jets, described in Ref. [?]. This b-tagging score for leading and subleading jets is then used for the resonant and non-resonant analyses categorization (see section 5.8.2).

The b-tagging scale factors have been calculated according to the BTV recipe, including the in situ calculation of signal efficiency. The signal efficiency has been calculated for all signal samples combined, in bins of p_T and $|\eta|$. The efficiency plots for tight WP, medium WP and loose WP can be seen in figure 5.7.

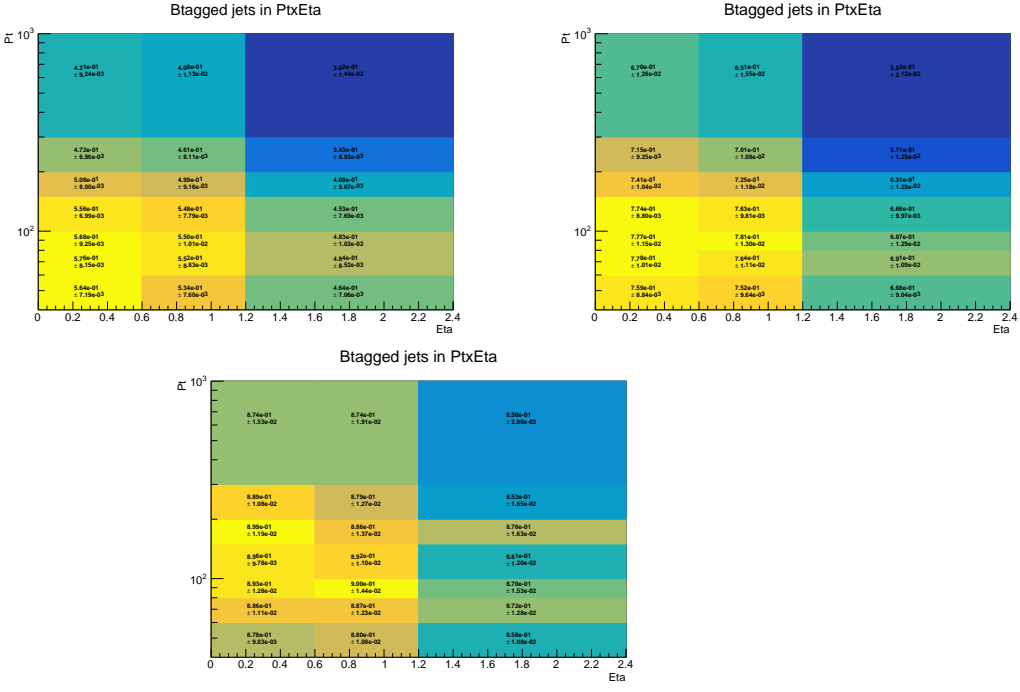


Figure 5.7: B-tagging efficiency for tight, medium and loose working points, as a function of jet p_T and $|\eta|$. WARNING - THESE ARE 2015 PLOTS, NEED TO UPDATE

5.4 Categorization

To boost the sensitivity of the analysis, we divide the signal region into different categories based on the b-tagging score of the leading and subleading jets. These categories are constructed based on the most sensitive regions of the 2D plane defined by the b-tagging scores of the leading and subleading jet candidates. In order to measure the significance of these regions without using our signal region, we use the control region defined by requiring one of the photons to fail the MVA ID selection. It's important to make sure that this control region models well our signal region in our variables of interest, namely the b-tagging scores and the 4-body invariant mass. That can be inferred through the plots in Figure 5.8.

By checking the ratio between the distributions of the signal region and the photon control region, before normalization, it was found that the photon control region needs to be scaled by a factor of 0.14 in order to also be consistent in terms of yields with the signal region. By the time this optimization was performed, only 22/fb of prompt reco data was available, therefore, the control region was also scaled by a factor of 35/22 in order to match the expected full integrated luminosity of 2016. For the significance calculation, we assume the SM HH signal with a cross section of 1 fb and

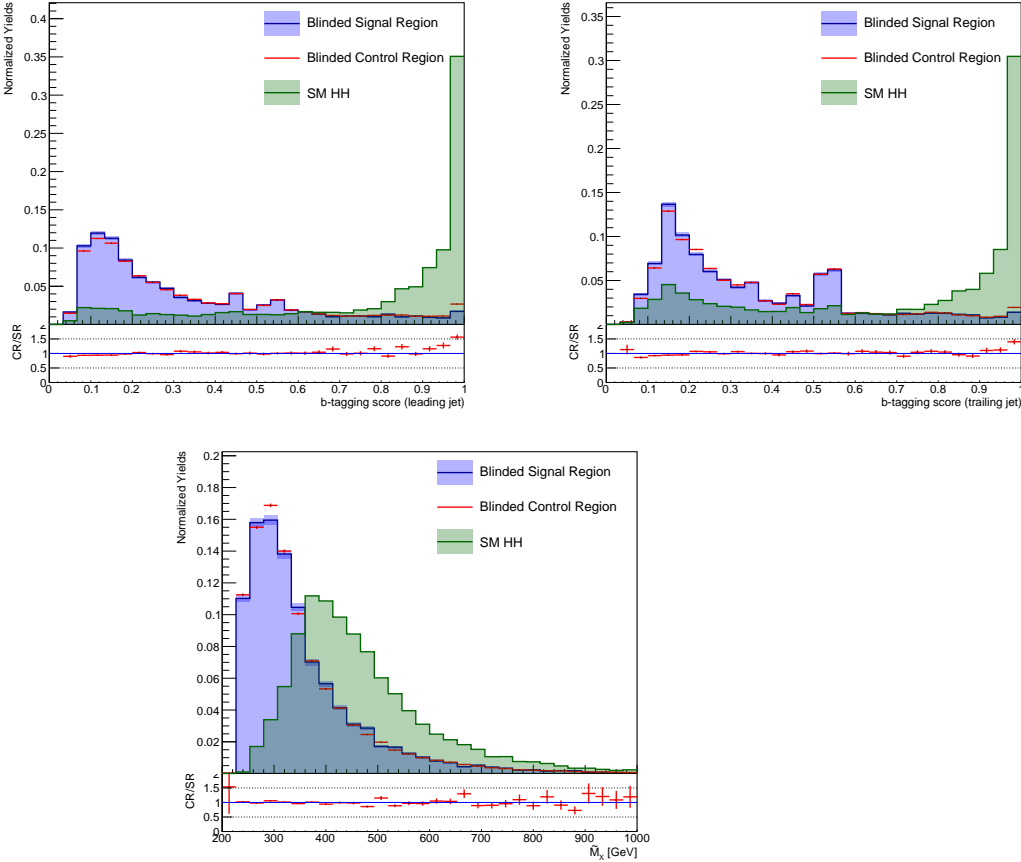


Figure 5.8: Comparison between blinded signal region and blinded photon control region in the leading jet b-tagging, subleading jet b-tagging and effective mass.

an integrated luminosity of 35/fb. We then calculate the significance of each exclusive b-tagging bin in the b-tagging 2D plane, as shown in Figure 5.9.

With that in mind, we construct different options for the categorization schemes. These can be seen in Figure 5.10. The green squares represent the High Purity Category (HPC), the yellow squares represent the Medium Purity Category (MPC) and the blue squares represent the Jet Control Region (JCR).

Another point that needs to be checked during the categorization is the expected number of background events. Since our background estimation is data driven, with the sidebands of the diphoton and dijet mass distributions, we need to make sure some events are left to fit. Therefore, we apply the mass window requirement (for the resonant case) and the \tilde{M}_X categorization (for the non-resonant case) and check the amount of expected background events. For the non-resonant case, we found that even using the most strict categorization definitions, we would still have enough expected background events for a robust description. For the resonant case, we test

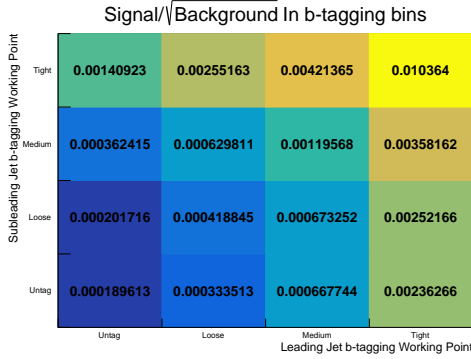


Figure 5.9: Significance in exclusive b-tagging bins in the 2D plane defined by the b-tagging score of the selected leading and subleading jet candidates.

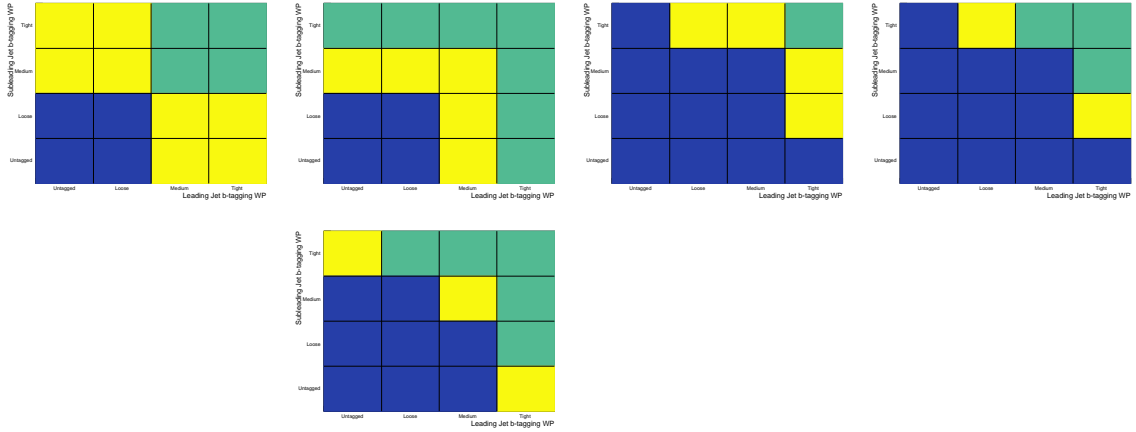


Figure 5.10: Different categorization strategies, from left to right, Run 1 categorization, 2015 low mass resonant categorization, Non-resonant option, Option 2 and Option 3.

the different categorization schemes shown in Figure 5.10 to see the expected number of background events (with the photon control region) on both HPC and MPC. These mass scans can be seen in Figure 5.11.

From Figure 5.11, we see that the non-resonant proposed categorization is too tight for most of the resonance masses in both categories. Option 2 seems to give a reasonable amount of background events for the modeling up until the boundary used in 2015 to define the low/high resonant regions. Therefore, for the low mass resonant analysis ($\tilde{M}_X < 500$ GeV), we use the categorization under Option 2 in the diagrams of Figure 5.10. For the High mass resonant analysis ($\tilde{M}_X > 500$ GeV), we use the same categorization scheme that was used for the 2015 low mass resonant analysis.

In addition to the categories mentioned above, cuts on the helicity angle $|\cos(\theta_{CS}^*)|$ have been investigated. It was found that the cut that maximizes the sensitivity of the

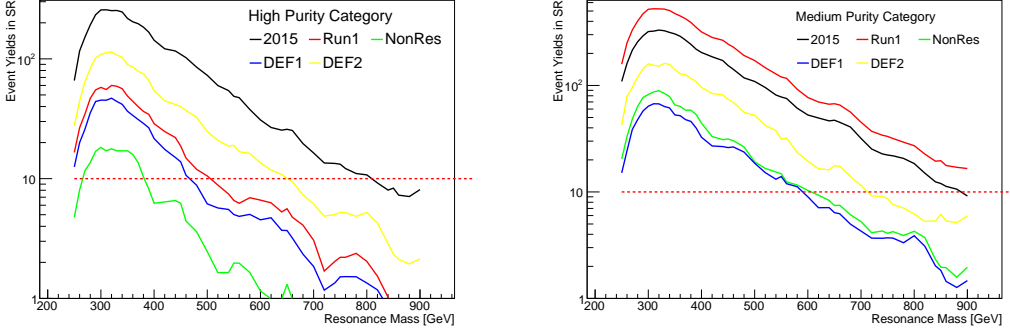


Figure 5.11: Expected background yields, from the photon control region scaled to the signal region, for the different resonant mass points (including mass window requirement), for the HPC and the MPC, respectively. Please note that "DEF1" in the legend corresponds to Option 2 in the diagrams of Figure 5.10, while "DEF2" corresponds to Option 3.

analysis is at 0.80 for the non-resonant categories. No cut is imposed in the resonant analysis.

5.4.1 MVA Categorization

During the analysis, it has been noticed that different kinematic variables could potentially contribute to tightening the signal region without cutting too much on the signal efficiency. However, this large-dimensional optimization procedure (all investigated variables) was not optimal. Instead, we have developed a multivariate analysis (MVA), combining these different variables, into a single discriminant. This discriminant is used to categorize the events in High Purity, Medium Purity categories and a control region, similarly to the cut based categorization.

The input variables investigated for this MVA were:

- Leading and subleading jets b-tagging score;
- Helicity angles $|\cos(\theta_{CS}^*)|$, $|\cos(\theta_{bb}^*)|$ and $|\cos(\theta_{\gamma\gamma}^*)|$: $|\cos(\theta_{CS}^*)|$ is defined as the angle between the direction of the $H \rightarrow \gamma\gamma$ candidate to the Colin-Sopper reference frame (assumes each incoming particle in the scattering to have 6.5 TeV); $|\cos(\theta_{xx}^*)|$ is defined as the angle between the particle x and the direction defined by the $H \rightarrow xx$ candidate (randomly choosing between x's), where $x = \gamma$ or b ;
- $p_T(\gamma\gamma)/M(jj\gamma\gamma)$ and $p_T(jj)/M(jj\gamma\gamma)$

The training was performed in the photon control region, as described in 5.3.2.1, modeling our background. Plots comparing the input variables in the photon control region and the blinded signal region are shown in Figure 5.12. As our signal in the training, we sum the 14 non-resonant HH samples available (box only, SM, and 12 BSM points). Thus, we have a training that is not specific to a single region in the parameter space, maintaining the sensitivities comparable between the benchmark points (as it is with the cut based categorization).

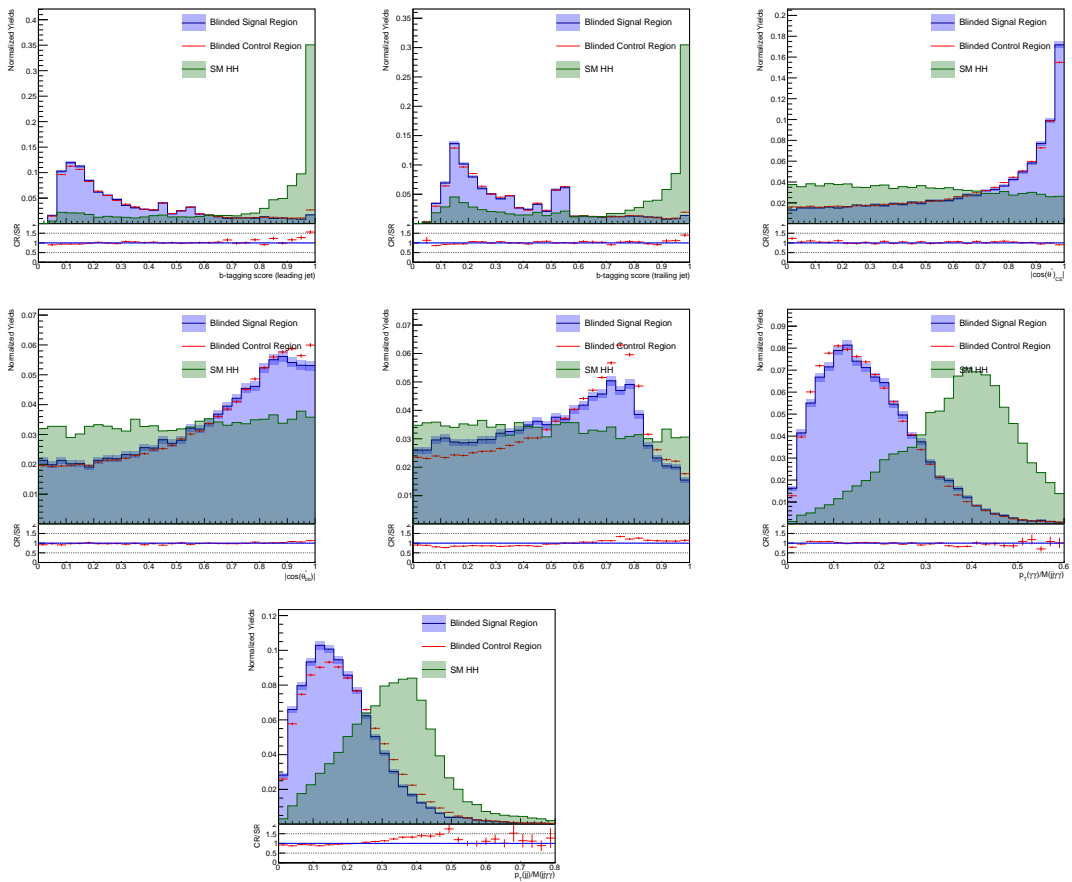


Figure 5.12: Distributions of input variables in the blinded photon control region, blinded signal region, and SM HH sample. All normalized to unity.

To improve the training, we split the training into two regions: Low Mass and High Mass. The low mass training is performed with events with \tilde{M}_X below 400 GeV, while the high mass training uses the complementary region. The training is based on a decision tree boosted with the gradient algorithm, with the trees randomized between iterations to decrease overtraining. To implement the training the TMVA package was used. The TMVA output plots are shown for both trainings in Figures

Mass Region	HPC	MPC
Low Mass	$\text{HHTagger} > 0.96$	$0.75 < \text{HHTagger} < 0.96$
High Mass	$\text{HHTagger} > 0.96$	$0.6 < \text{HHTagger} < 0.96$

Table 5.4: Non-resonant categorization with HHTagger discriminant.

5.13 and 5.14. From now on, we will refer to the trainings discriminant variable as HHTagger.

With the HHTagger discriminant, we build our two signal categories based on the maximal S/\sqrt{B} point, separately in the high mass and in the low mass regions. As signal, we use the SM HH sample to calculate the sensitivity. The outcome of this study was the categorization in table 5.4. The expected number of background events, when comparing MPC and HPC between cut based and MVA approaches, is comparable and consistent, while for the number of signal events, the performance is better for the HHTagger categorization.

We have also to insure that the HHTagger selection does not shape our variables of interest, $M(jj)$ and $M(\gamma\gamma)$. We demonstrate that there is no appreciable shaping by comparing the $M(jj)$ and $M(\gamma\gamma)$ shapes in different bins of the HHTagger discriminant. This can be seen in Figure 5.15.

5.4.1.1 Performance Cross-Checks

We have performed several cross checks to look for possible improvements on the categorization MVA.

- **Signal Hypothesis**

In the standard training, the sum of all non-resonant samples are used as signal hypothesis. However, this might not be the optimal training for the SM HH case. To test this, we compare the performance of different trainings assuming the SM HH signal. The signal hypotheses tested are:

- All non-resonant (standard);
- SM HH;
- SM HH, with separate training for the high mass and low mass region (similar to standard);
- SM HH + Benchmark 3 (this benchmark point refers to the node that contains the SM point);

- SM HH + Benchmark 3, with separate training for the high mass and low mass region (similar to standard).

The background hypothesis for this test is the photon control region, in the high mass region.

The ROC curves from the different trainings are shown in Figure 5.16. Since no significant improvement is seen in the high purity region (for background rejection larger than 95%, a typical value for the chosen WPs), the standard training method is kept in use.

- **Background Hypothesis**

In the standard training, the photon control region is used as a background model, avoiding MC reliance. However, this might not be the optimal because the photon control region might have different correlation between the MVA variables with respect to the signal region. To test this, we compare the performance of different trainings assuming different background hypotheses:

- Photon control region (standard);
- Blinded signal region;
- Blinded control region (to insure that the difference between the two previous trainings does not come from blinding).

The background hypothesis for this test is the blinded signal region, in the high mass region, and the signal hypothesis is SM HH.

The ROC curves from the different trainings are shown in Figure 5.17. While some improvement is seen, this training is not optimal for statistical reasons. The blinded signal region contains significantly less events than the photon control region. This limits the precision and accuracy of the multivariate analysis training. Specifically, it has been observed that the blinded signal region does not contain events in the high BDT region (signal-like phase space), which can cause over training. The second issue is that, optimally, training on a dataset that is statistically independent from the one to which it will be applied leads to a more robust procedure.

- **Resonant Hypothesis**

While this MVA is trained with the non-resonant signal hypotheses, it can also be applied to the resonant search. We check, however, if a dedicated training with the resonant samples as signal hypothesis performs better, when applying the categorization to the resonant analysis. This is tested by comparing the categorization performance of the standard training versus a resonant training on a resonant signal point. The plot in Figure 5.18, these two trainings are shown and no significant difference is seen. Therefore the standard, non-resonant training will be used also for the resonant analysis.

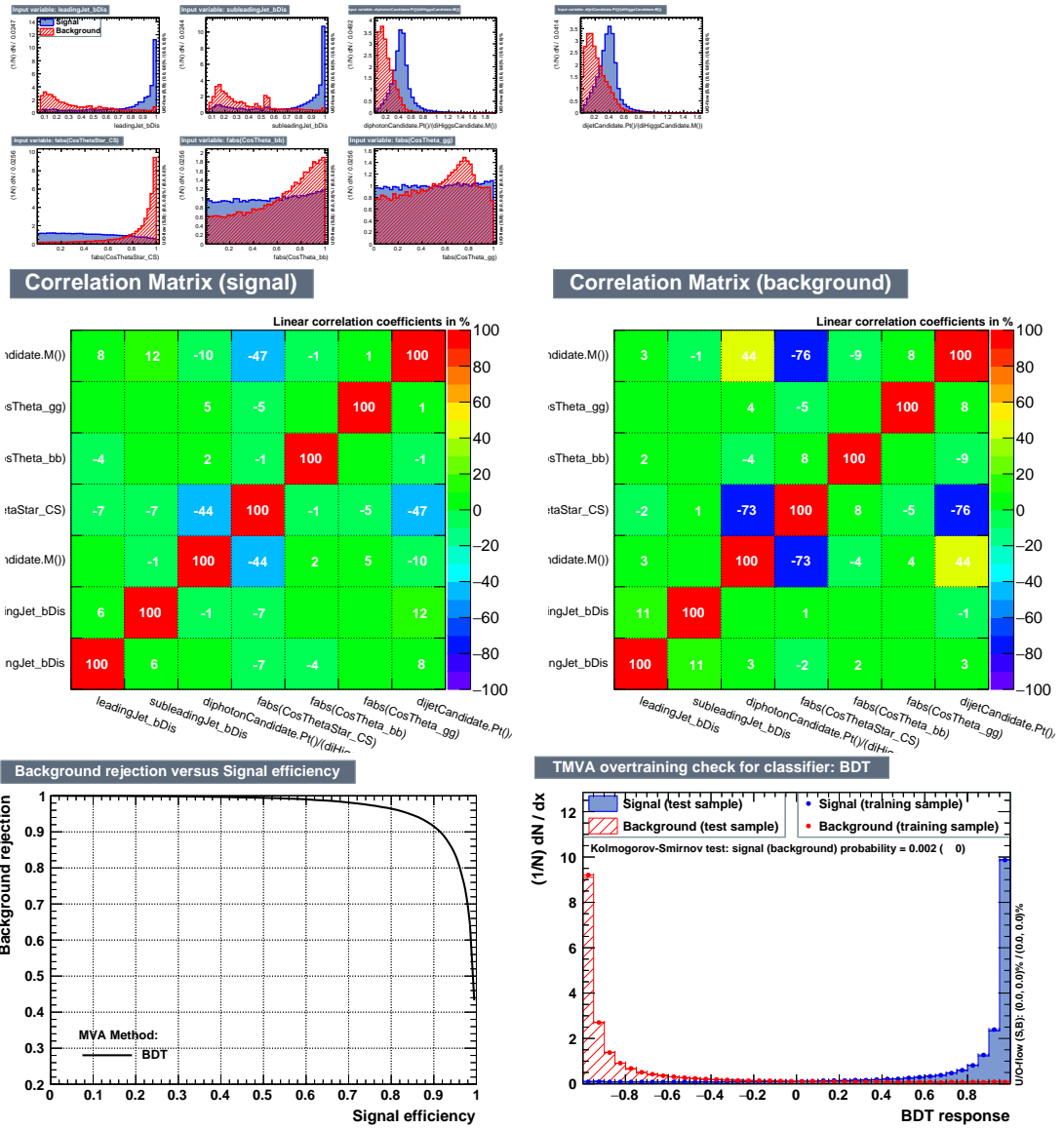


Figure 5.13: TMVA output plots for the High Mass Training.

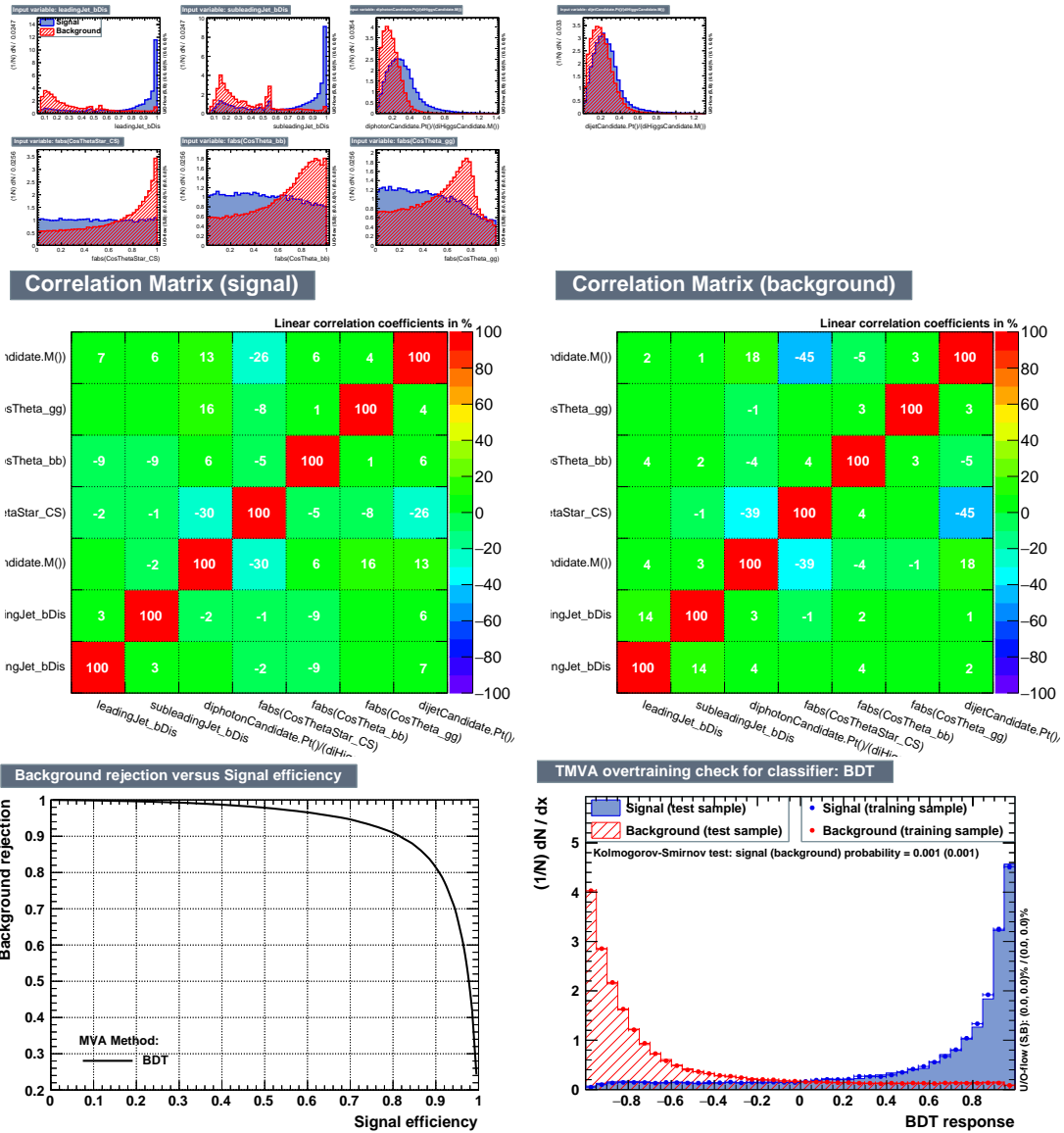


Figure 5.14: TMVA output plots for the Low Mass Training.

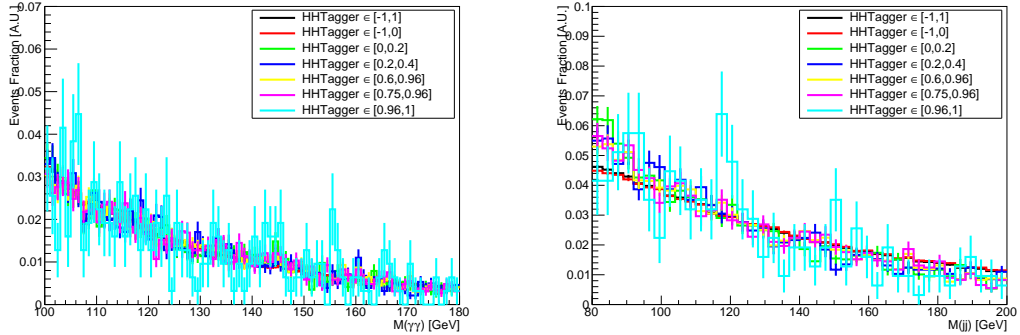


Figure 5.15: $M(\gamma\gamma)$ and $M(jj)$ in bins of HHTagger. Although the slope changes between bins, this effect does not influence the limit setting.

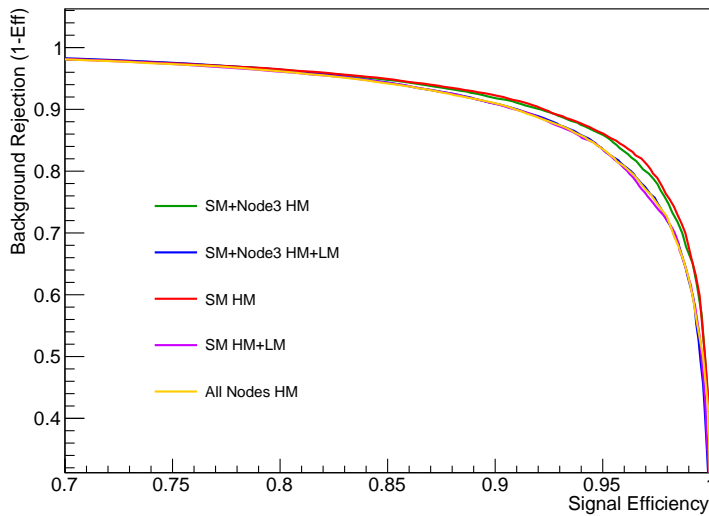


Figure 5.16: ROC curves with different signal hypotheses for training. The performance is evaluated on the high mass region, with the photon control region as background and SM HH as signal.

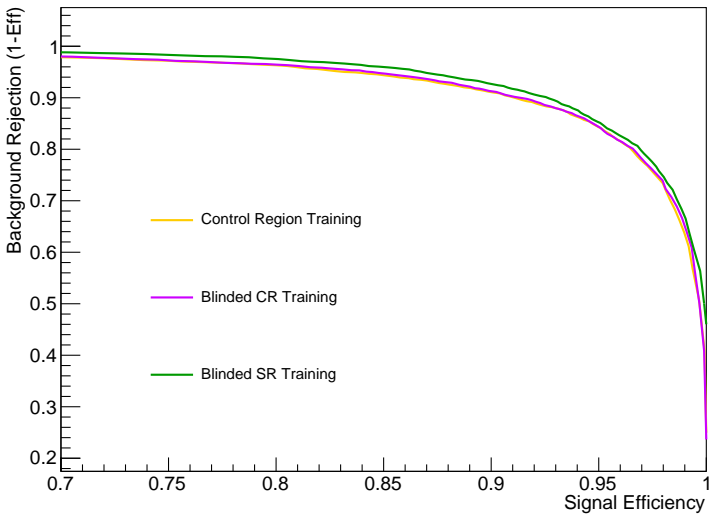


Figure 5.17: ROC curves with different background hypotheses for training. The performance is evaluated on the high mass region, with the blinded signal region as background and SM HH as signal.

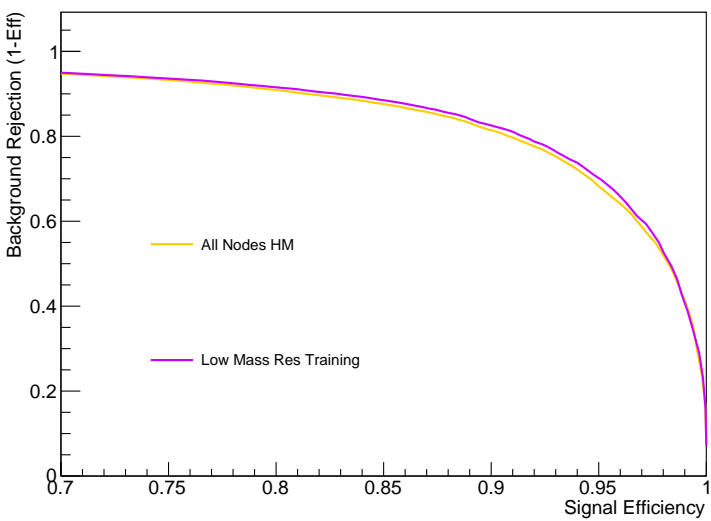


Figure 5.18: ROC curves with different signal hypotheses for training. The performance is evaluated on the high mass region, with the photon control region as background and Radion 300 GeV as signal.

5.5 \tilde{M}_X and Mass Window Selection

In order to increase the sensitivity of the resonant analysis, we perform a cut on the 4-body invariant mass before the signal extraction with the 2D fit. In the Run I analysis, the 4-body invariant mass was corrected with a kinematic fit, to mitigate the effects of the low mass resolution of the dijet system. However, it has been seen that this method is too reliant on the a-priori set of energy and spatial resolutions for the jets in that analysis (these resolutions must be measured in situ, since they are kinematic dependent). One solution for this was to use instead the variable \tilde{M}_X , defined as:

$$\tilde{M}_X = M(jj\gamma\gamma) - M(jj) - M(\gamma\gamma) + 250 \text{ GeV}. \quad (5.3)$$

This variable performs a kinematic fit "by hand", by effectively scaling the dijet and diphoton invariant masses to 125 GeV. In order to quantify the improvement of this variable with respect to other 4-body invariant mass reconstructions, we calculate the width of the smallest interval that covers 68% of the signal shape in each reconstruction method. We compare \tilde{M}_X with the standard $M(jj\gamma\gamma)$ and with $M(jj\gamma\gamma)_{KF}$, which is reconstructed with a kinematic fit in $M(jj)$, which tries to vary the jets within their uncertainties to achieve $M(jj) = 125$ GeV. The widths are compared in Figure 5.19.

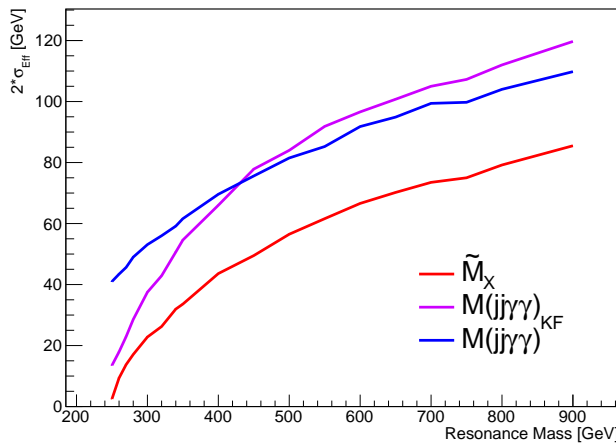


Figure 5.19: Different 4-body mass widths: \tilde{M}_X , $M(jj\gamma\gamma)$ with kinematic fit, and $M(jj\gamma\gamma)$ with no extra corrections.

The effect of reconstructing the 4-body invariant mass with \tilde{M}_X on the signal shape can be seen in 5.20. The figure shows that the \tilde{M}_X reconstruction yields a

better performing resolution for the 4-body invariant mass reconstruction, meaning that we can perform tighter cuts on it and increase the signal/background for each signal mass point.

One extra check we must do while using this variable is to make sure there are no unexpected effects on the background shapes. The effect of \tilde{M}_X is similar to the kinematic fitted $M(jj\gamma\gamma)$, but more pronounced, which is the sharp kinematic cut around the $\tilde{M}_X = 250$ GeV point. This can be seen in the figures in section 5.7..

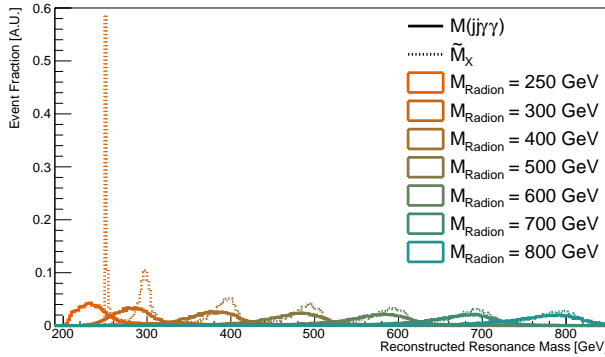


Figure 5.20: Different 4-body mass reconstructions: \tilde{M}_X (dotted line), $M(jj\gamma\gamma)$ with kinematic fit (dashed line), and $M(jj\gamma\gamma)$ with no extra correction (full line). Signals for different radion masses are shown. The normalizations are such that the non-corrected mass peaks at 1 (same normalization for different reconstructions in each mass point). This plot is made after full selection, in the b-tagging signal region (at least one medium b-tagged jet).

It has also been observed that, for the non-resonant signal samples, the \tilde{M}_X variable approaches the generator level HH invariant mass distribution more so than the kinematic fitted $M(jj\gamma\gamma)$ and the default 4-body invariant mass. This can be seen in figure 5.21. For this, \tilde{M}_X will also be used in the non-resonant analysis.

One desirable effect of the \tilde{M}_X definition in this version of the analysis, compared to the 2015 definition (which only scaled the $M(jj)$ value as in $\tilde{M}_X = M(jj\gamma\gamma) - M(jj) + 125$ GeV), is that a \tilde{M}_X selection does not bias $M(\gamma\gamma)$ and $M(jj)$. This can be seen in the 2D plots of $\tilde{M}_X : M(\gamma\gamma)$ and $\tilde{M}_X : M(jj)$ in Figure ??.

With \tilde{M}_X , we can improve the resonant analysis by tightening the signal region around the 4-body resonance mass (mass window). Through limits optimization, it has been checked that constructing a mass window with the smallest interval that covers 60% of the signal shape provides the best sensitivity. The size of these intervals, as a function of the hypothesis mass, is seen in Figure 5.23.

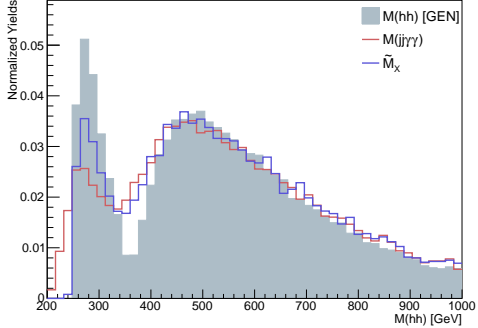


Figure 5.21: Behavior of \tilde{M}_X , $M(jj\gamma\gamma)$ and GEN-level $M(hh)$. WARNING - THIS IS THE 2015 PLOT

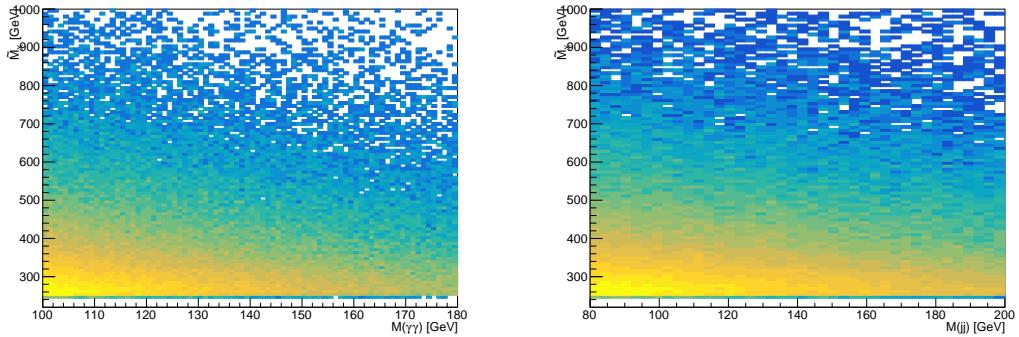


Figure 5.22: $\tilde{M}_X : M(jj\gamma\gamma)$ and $\tilde{M}_X : M(jj)$ in the photon control region, scaled to unity and Z-axis in log scale.

We implement this mass window by requiring that $W_- < \tilde{M}_X < W_+$. W_{\pm} are calculated based on the widths defined in Figure 5.23. We fit W_{\pm} with a 3rd degree polynomial so that the mass windows can be defined functionally based on the mass hypothesis. These fits, and, therefore, the definition of W_{\pm} can be seen in Figure 5.24. W_{\pm} can be inferred through the Y-axis of 5.24, W_- is defined by the blue curve and W_+ by the red.

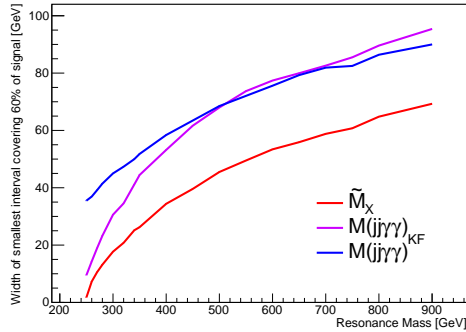


Figure 5.23: Mass window sizes as a function of the resonance mass.

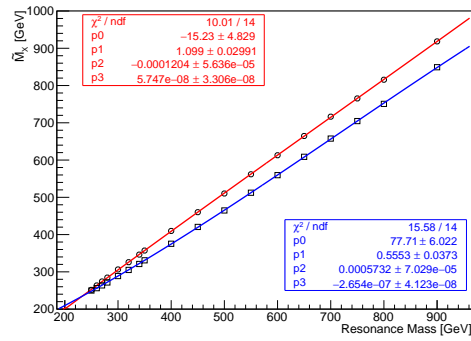


Figure 5.24: Mass window sizes as a function of the resonance mass.

5.6 Selection Efficiencies

As a summary of the previous sections, the cut flow of the analysis is as follows:

- At least two photons and two jets in the event
- At least two photons pass the trigger based pre-selection (see sec. 5.3.1);
- At least two photons pass the kinematic and identification requirements (see sec. 5.3.2) → select two highest E_T photons as diphoton candidate;
- At least two jets pass the kinematic selection (see sec. 5.3.3) → select two jets with highest b-tagging score as dijet candidate;
- Event can be classified in either High Purity Category or Medium Purity Category;

The efficiency after each step above and taking into account the acceptance is estimated and shown for each of the signal samples considered in our analysis. Figure 5.25 shows the cut flow efficiency \times acceptance for the graviton signal samples

ranging from mass hypothesis of 250 up to 900 GeV on the top left. It shows the one with the bjet regression applied, on the top right and the ratio of the efficiencies of the two on the bottom. figure 5.26 shows the analog cut flow efficiency \times acceptance of the Radion samples (with mass range of 250 to 900 GeV) on the top left. It shows the same cutflow with the bjet regression applied, on the top right and the ratio of the efficiencies of the two on the the bottom. Figure 5.27 and figure 5.28 show the analog cutflow \times acceptance of the 14 nodes of nonresonant signal benchmarks corresponding to 12 anomalous couplings combinations, in addition to the box diagram(node=0) and the SM couplings (node=1) as defined in subsection 5.2.2 and in table 5.2. Figure 5.27 displays the values for the cut based categorization on the top left, the ones with the MVA based categorization on the top right and the ratios of the two on the bottom. Figure 5.28 shows the values when the b-jet regression is applied in addition the MVA based categorization in the left, and the ratio of the two.

These figures report results using for the above described selections where the photon identification is the $H \rightarrow \gamma\gamma$ MVA procedure.

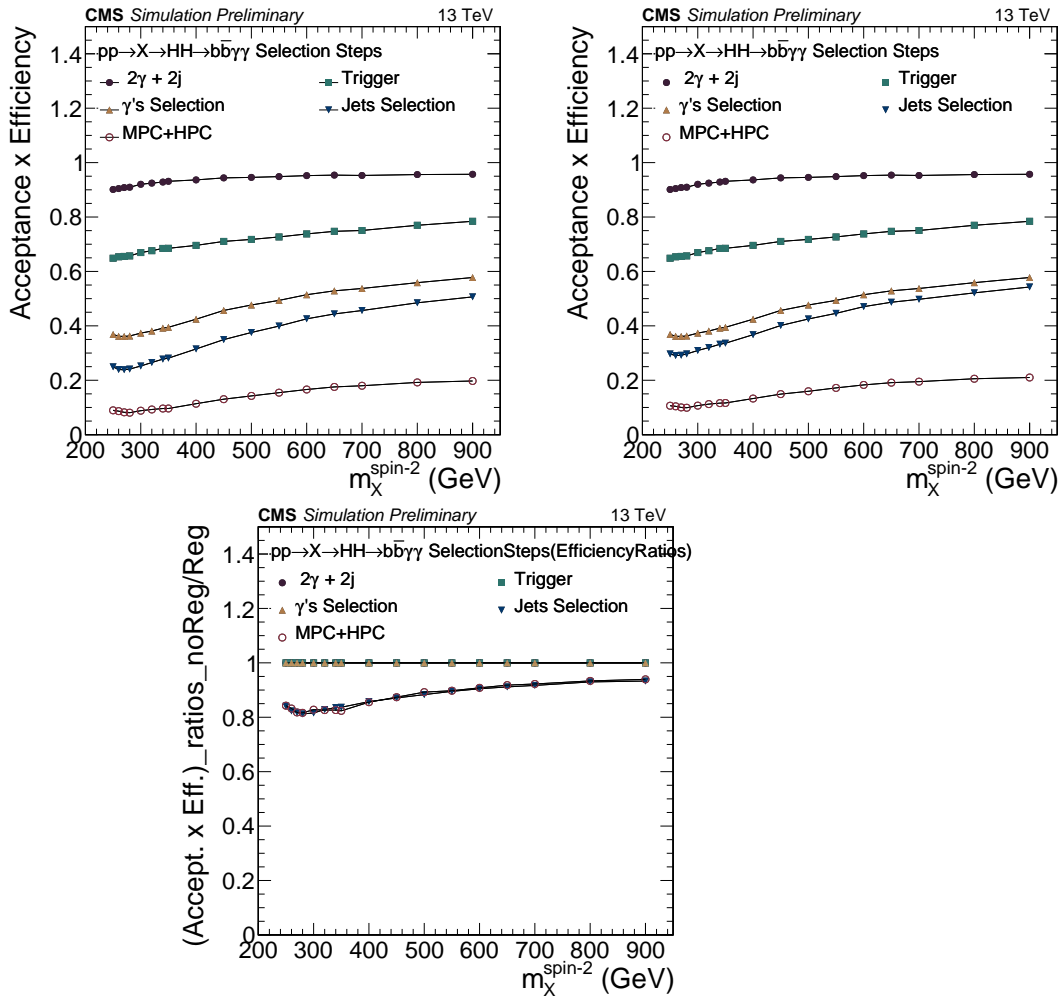


Figure 5.25: Graviton signal acceptance \times efficiency for each cut (described in text) on the top left plot, the bjet regression is applied on the top right and the ratio of the cutflows on the bottom.

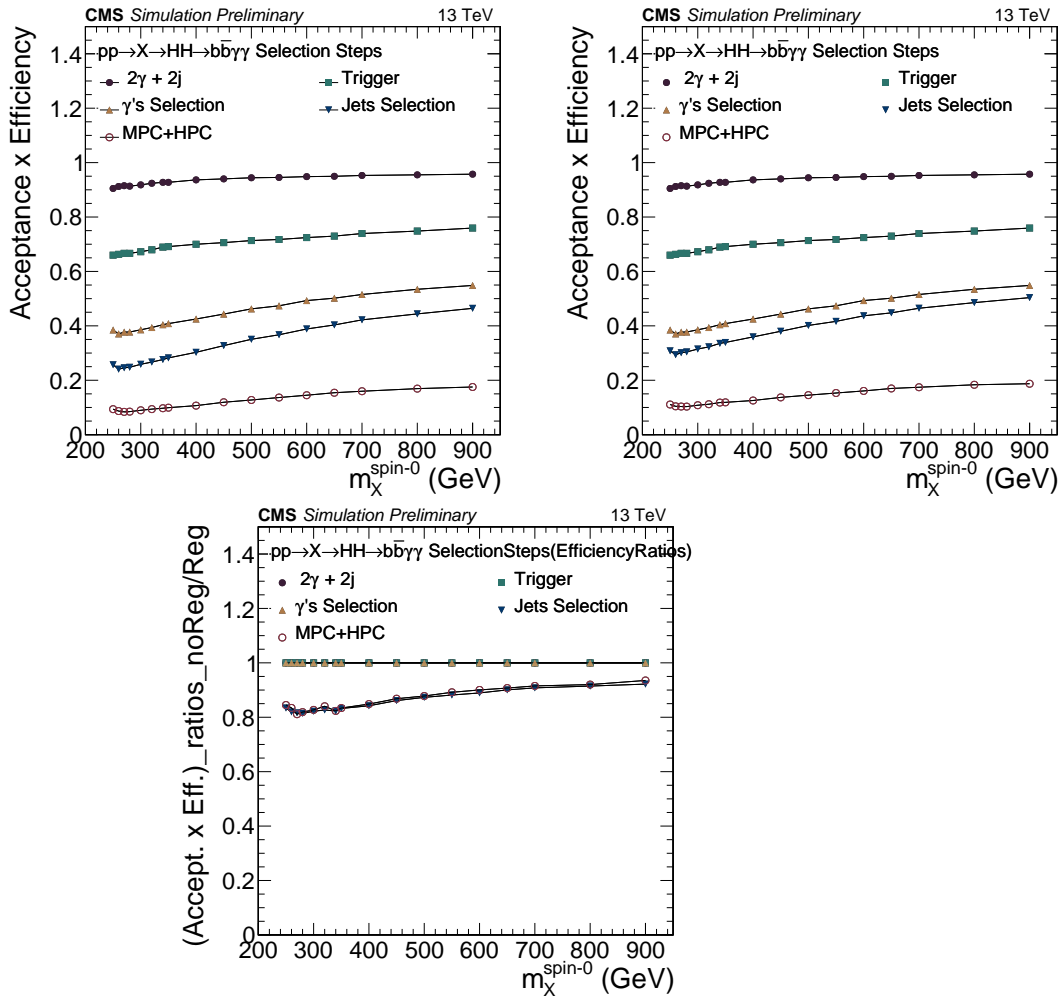


Figure 5.26: Radion signal acceptance \times efficiency for each cut (described in text) on the top left plot, the bjet regression is applied on the top right and the ratio of the cutflows on the bottom.

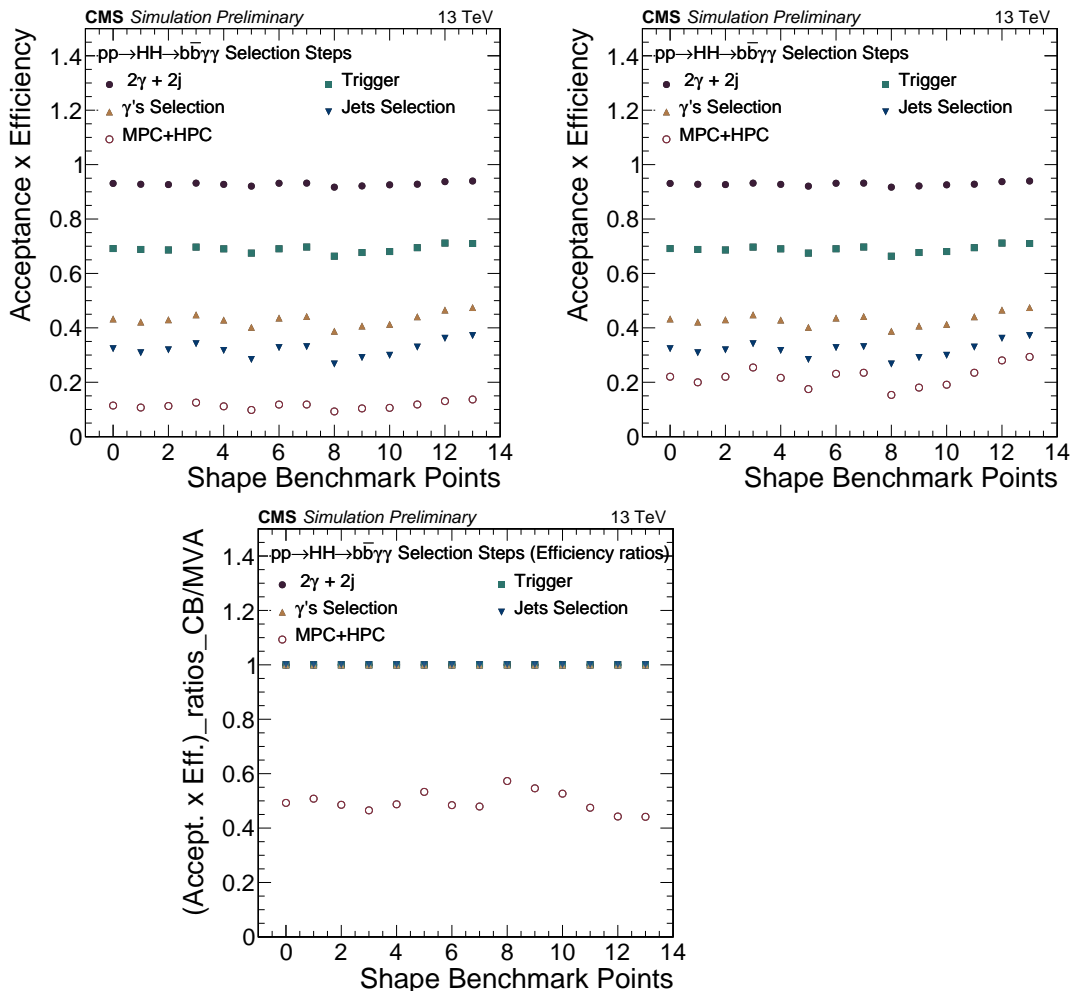


Figure 5.27: Non-resonant acceptance x efficiency. Cut based categorization on the top left, MVA based categorization on the top right (analysis version) and the ratio of the two on the bottom.

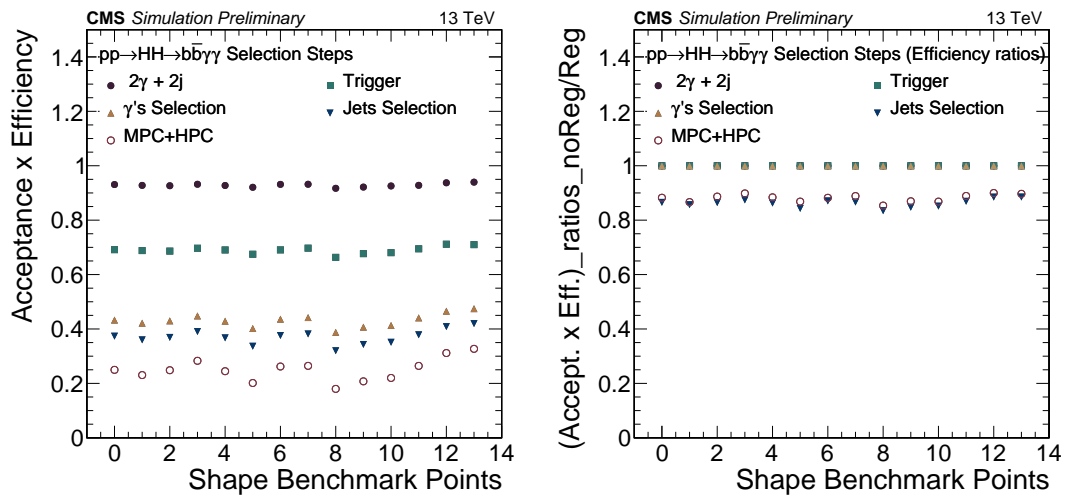


Figure 5.28: Non-resonant acceptance x efficiency. Jet energy regression applied in addition to MVA based categorization on the left, ratio (bjetReg.+MVA)/MVA on the right (analysis version).

5.7 Control Plots

In order to validate the Monte Carlo simulations, we produce data/Monte Carlo comparison plots (control plots) of the light jets control region (JCR, 0 medium b-tagged jets) and of the signal region (SR), both blinded in the $115 < M(\gamma\gamma) < 130$ GeV region. In order for background and data to match, the DiPhoton+Jets contribution has been scaled by a factor of 1.5, while the prompt-fake and fake-fake contributions from the GJets and QCD samples have been scaled to data. It should be stated that the background MC is not used at any time in this analysis. The signal in these plots is normalized for 500 fb.

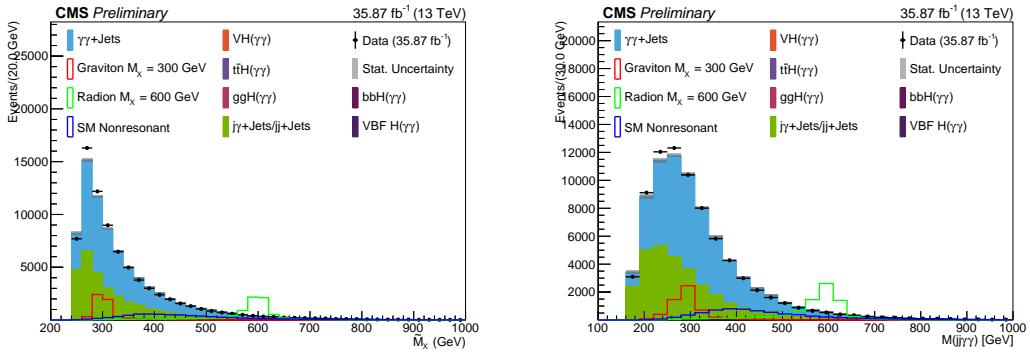


Figure 5.29: Distributions for the blinded signal region.

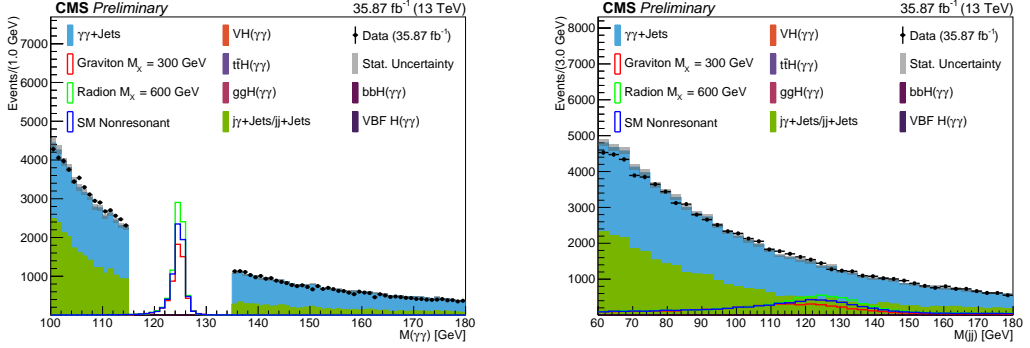


Figure 5.30: Distributions for the blinded signal region.

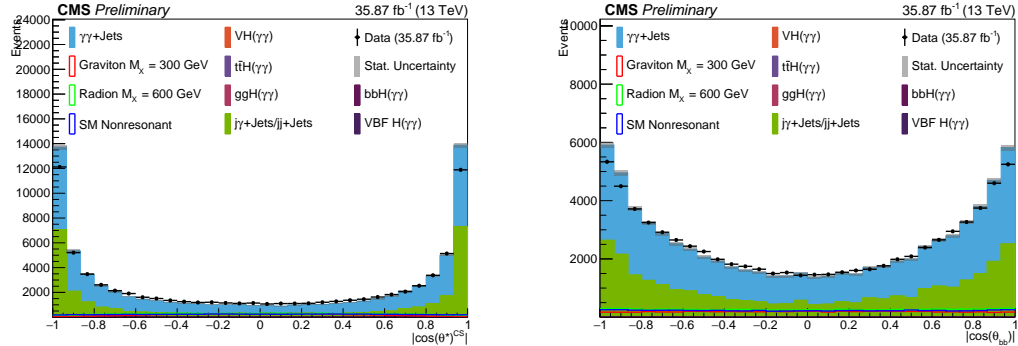


Figure 5.31: Distributions for the blinded signal region.

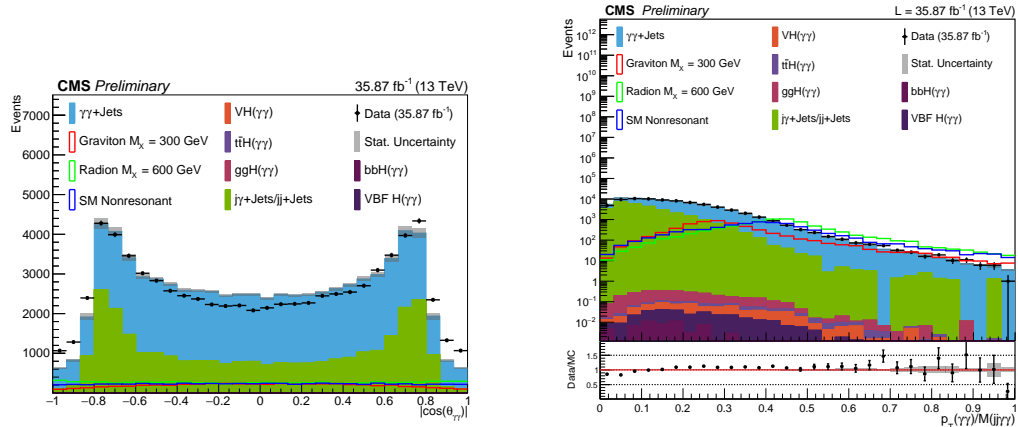


Figure 5.32: Distributions for the blinded signal region.

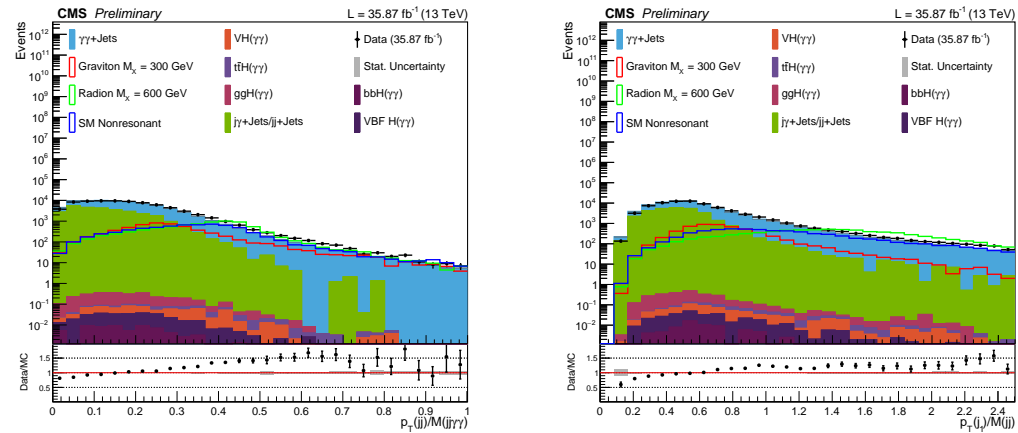


Figure 5.33: Distributions for the blinded signal region.

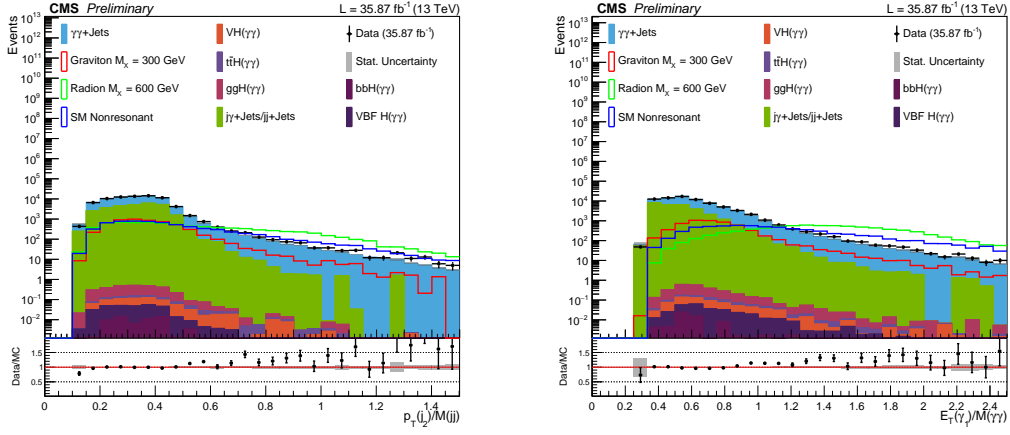


Figure 5.34: Distributions for the blinded signal region.

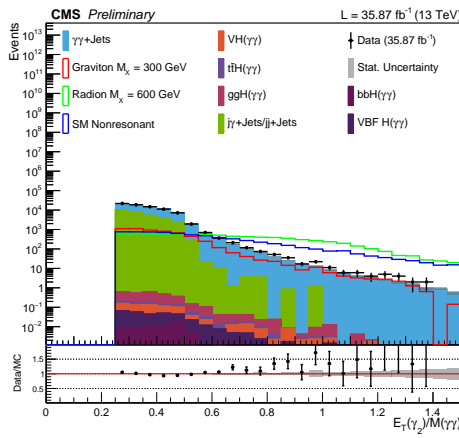


Figure 5.35: Distributions for the blinded signal region.

5.8 Statistical Modeling and Limit Extraction

The signal extraction and limit setting in this analysis is performed with a 2D fit on the $M(\gamma\gamma) : M(jj)$ plane, since we expect our signal to peak in both axes. For our background, they are expected to be uncorrelated given our statistical precision. With this last assumption, we can construct background function models as $f_\gamma(M(\gamma\gamma)) \times f_J(M(jj))$, where f_γ (f_J) are our functional choices to fit the diphoton (dijet) mass spectrum. A thorough explanation of the background uncorrelation hypothesis is given at the end of this section.

5.8.1 Signal Model

As a signal model in the limit extraction, we use parametric models fitted to the simulated samples after the full selection. Each fit is done in each different sample independently, i.e., for all resonance masses, spins and for all different non-resonant hypotheses. The choice of parametric model for $M(\gamma\gamma)$ and $M(jj)$ individually is a double sided Crystal-Ball function. The double sided Crystal-Ball function is defined as follows:

$$f(x; \mu, \sigma, \alpha_L, p_L, \alpha_R, p_R) = N \cdot \begin{cases} A_L \cdot \left(B_L - \frac{x-\mu}{\sigma} \right)^{-p_L}, & \text{for } \frac{x-\mu}{\sigma} > -\alpha_L \\ A_R \cdot \left(B_R + \frac{x-\mu}{\sigma} \right)^{-p_R}, & \text{for } \frac{x-\mu}{\sigma} > \alpha_R \\ e^{\frac{(x-\mu)^2}{\sigma^2}}, & \text{for } \frac{x-\mu}{\sigma} < -\alpha_L \text{ and } \frac{x-\mu}{\sigma} > \alpha_R \end{cases}, \quad (5.4)$$

where the A_L, A_R, B_L, B_R constants are defined by:

$$A_k = \left(\frac{p_k}{|\alpha_k|} \right)^{p_k} \cdot e^{-\frac{\alpha_k^2}{2}}, \quad (5.5)$$

$$B_k = \frac{p_k}{|\alpha_k|} - |\alpha_k|, \quad (5.6)$$

where k is either L or R . This definition is such that there are two independent tails, a left tail (L) and a right tail (R), and a gaussian core. This signal model is enough to model both the high mass resolution of $M(\gamma\gamma)$ and the lower resolution of $M(jj)$. With respect to the signal model chosen for previous versions of the analysis, such as the 2015 analysis, this choice is beneficial when comparing to a sum of a gaussian and a single sided Crystal-Ball because the left and right tails are made completely independent, while maintaining the same number of free parameters.

These signal fits can be seen in figures ??, ??, ??, ?? and ?? for the 250, 300, 400, 600 and 900 GeV Radion signals, and in figures 5.42 and ?? the signal fits

for the non-resonant SM HH production in the high mass and low mass categories, respectively.

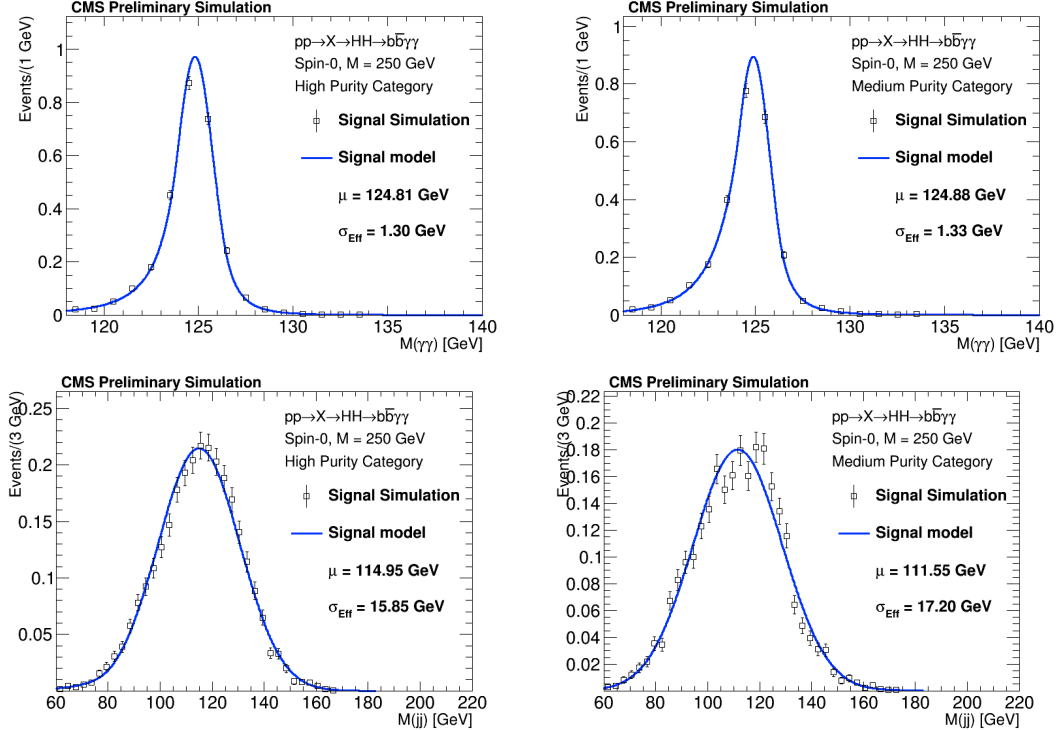


Figure 5.36: Signal fits for the Radion 250 GeV sample after full analysis selection, in High and Medium purity categories.

5.8.1.1 Correlation Studies

The choice of parametric signal model makes the assumption that the full 2D distribution can be modeled by a product of PDFs. This choice is not the most general one, as it does not model correlations between $M(jj)$ and $M(\gamma\gamma)$. One important question, therefore, is whether the analysis is sensitive to correlations that are not modeled by our choice of signal model. To study this, we study the differences between the MC signal simulation and the 2D fitted PDF via residues:

$$R_{ij} = \frac{N_{ij}^{\text{PDF}} - N_{ij}^{\text{MC}}}{\sigma_{N_{ij}^{\text{PDF}}}^{\text{Poisson}}}, \quad (5.7)$$

where ij refers to bin i in $M(\gamma\gamma)$ and bin j in $M(jj)$, and $\sigma_{N_{ij}^{\text{PDF}}}^{\text{Poisson}}$ is the Poissonian error of the expected (PDF) and observed (MC). These residuals are shown in Figures 5.43, 5.44, 5.45 and 5.46. The signal MC normalization for these plots are to 1/fb signal cross section. We see no structures in the residual plots in the region where

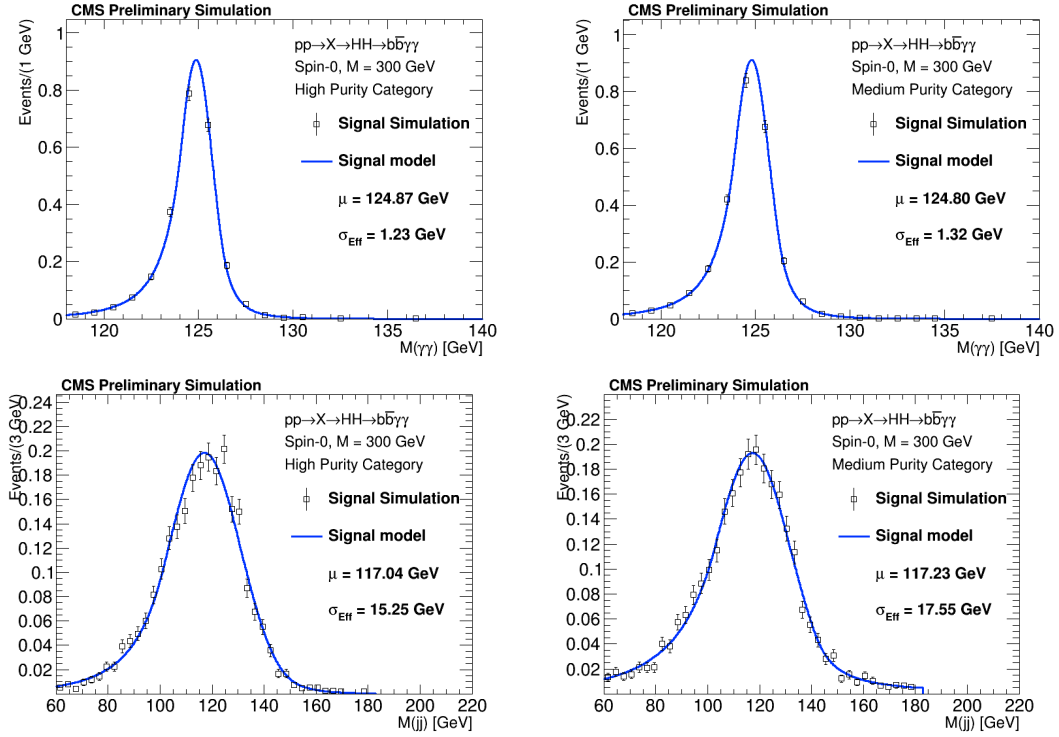


Figure 5.37: Signal fits for the Radion 300 GeV sample after full analysis selection, in High and Medium purity categories.

the signal is expected, therefore, we assume that the PDF product modeling is good enough given the statistical precision we have.

5.8.2 Background Model

To study the background fits, we use the fake photon control region (one photon in the diphoton candidate fails the identification requirements). From this control region, we randomly pick the number of events that is expected from the signal region under study according to the reweighted control sample described in section .

The functional choice to model the background in both fitting variables is the Bernstein family of polynomials. We also assume that the same order of polynomial is to be used in both variables. This comes from the fact that the order of the polynomial is related to the precision of the fit (degrees of freedom), which, in turn, is related to the number of events being fitted.

The first study performed is the order fixing. We fit consecutive orders of the three families of functions and check the $2\Delta NLL$ between the two consecutive fits. This $2\Delta NLL$ should be distributed as a $\chi^2(\alpha)$ distribution with the number of degrees of freedom equal to the difference in number of free parameters between the two

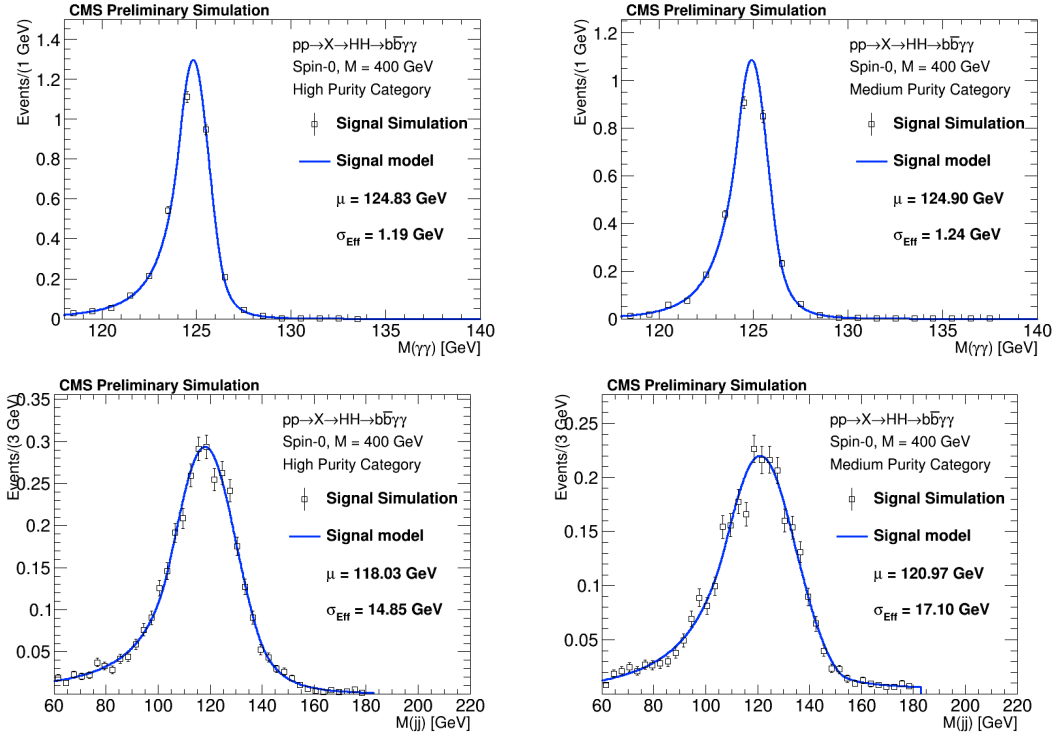


Figure 5.38: Signal fits for the Radion 400 GeV sample after full analysis selection, in High and Medium purity categories.

consecutive orders (α). We then calculate the p-value of having a $2\Delta NLL$ higher than the one calculated before, given the $\chi^2(\alpha)$ distribution. If this p-value is lower than 0.05, we accept the higher order function, and continue the procedure for the next order. If this p-value is higher than 0.05, the higher order function is assumed to be too flexible given the data and the procedure terminates having found the highest order suitable function.

Due to the different regimes of our signal regions after the mass window requirements and of the non-resonant selection, it is expected that our fits will involve very different background yields. For that, we perform the $2\Delta NLL$ test in all different signal regions. The result of this test are regions of validity in number of background events to be fit. This means that the choice of Bernstein order will depend on the number of events being fitted in a given signal region. The results of the study show that, for fits with less than 15 events, a 1st Order Bernstein passes the $2\Delta NLL$ test. For fits with 25 or more events, but less than 200, a 2nd Order Bernstein passes the $2\Delta NLL$ test. For fits with 200 or more events, a 3rd Order Bernstein passes the $2\Delta NLL$ test.

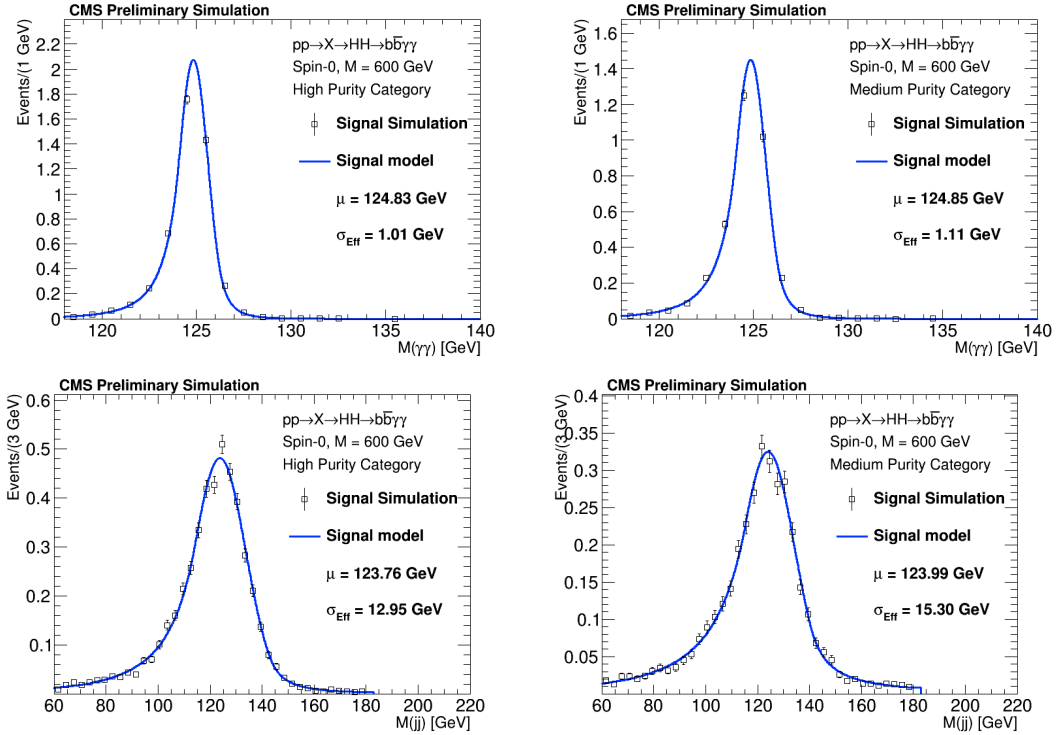


Figure 5.39: Signal fits for the Radion 600 GeV sample after full analysis selection, in High and Medium purity categories.

5.8.2.1 Bias Studies

After the order fixing, we must ensure that the functional form chosen does not bias a possible signal strength measurement in the analysis. This can happen because the real background shape that is being fitted might not be exactly the chosen functional form. Since we have no way of defining what this true shape is, we compare the signal strength measured (μ) from the background models with respect to different background shape hypotheses, as produced by toy Monte Carlo.

The goal is to find at least one background model that can fit other background shapes without a statistically significant bias in the signal strength reconstruction. The goal of having a background model with a bias less than 0.14 for all assumed shapes is set. This is justified by investigating the effect that a signal strength bias can be correct by increasing the uncertainty on μ until the true value is within the 1σ coverage of μ CITE JOSH.

We compare our 2D Bernstein model to models constructed with a Laurent series for both $M(\gamma\gamma)$ and $M(jj)$, and with sums of exponentials for both $M(\gamma\gamma)$ and $M(jj)$. We construct models with different Laurent and Exponential sum orders.

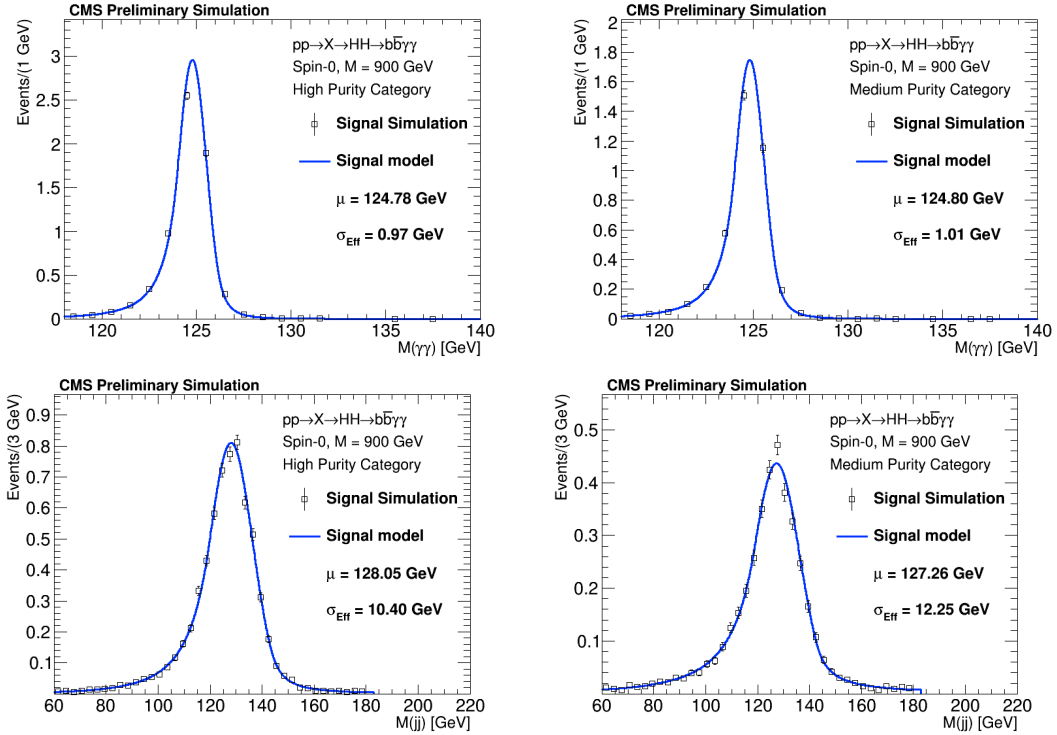


Figure 5.40: Signal fits for the Radion 900 GeV sample after full analysis selection, in High and Medium purity categories.

The first step in the bias studies is to get pre-fit shapes of all background models. This is done in the same datasets used for the order fixing procedure: fake photon control region scaled to match the statistics found in different data signal regions.

After the pre-fit shapes are constructed, toy Monte Carlo events are generated based on the pre-fitted background models. Batches of 2000 toy datasets are thrown for each background model. These toys are thrown injecting also signal events, according to the signal yields expected in each category. For that, we assume a signal cross section of 1 fb, for all resonant mass points and non-resonant benchmark points. Finally, the third step is fitting the 9 batches of toy datasets with the same background models and extracting the μ from each of the 2000 toy datasets. Both the toy generation and the fitting steps are done with the CMS combine tool CITE COMBINE.

5.8.2.2 Goodness of Fit

To check how well the background model fits the data, we perform a goodness of fit test in our blinded signal region. The Kolmogorov-Smirnov (KS) test was chosen for its good performance on unbinned datasets, which is the case of this analysis.

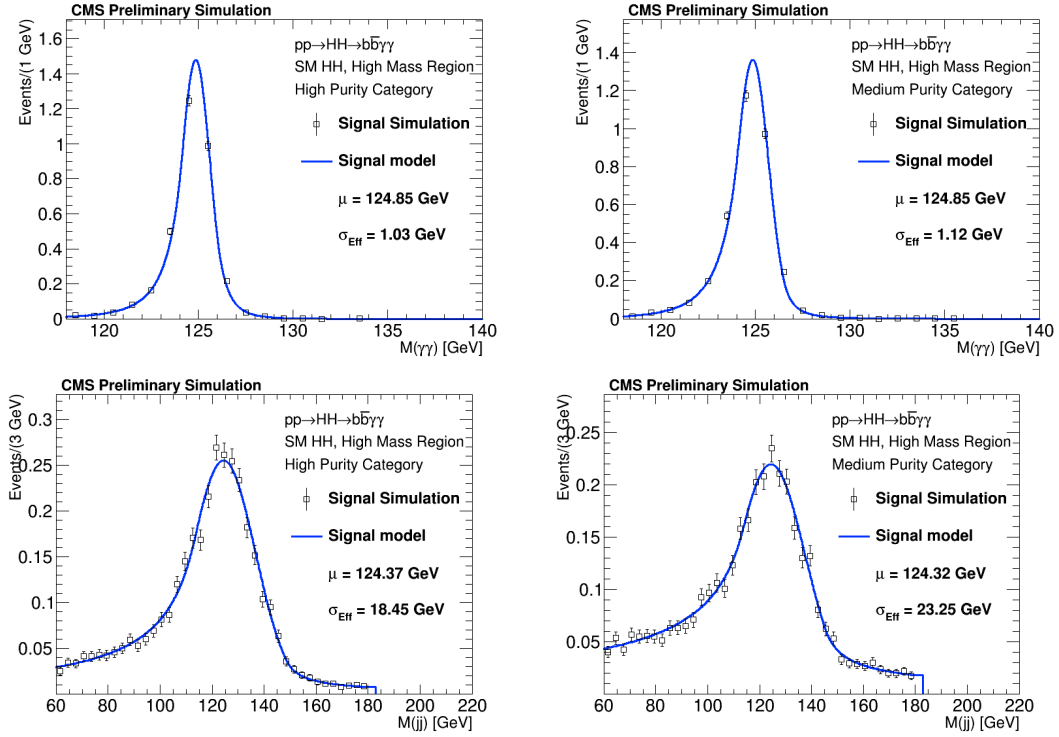


Figure 5.41: Signal fits for the SM HH non-resonant sample after full analysis selection, in categories 0 and 1, for high mass category.

Unfortunately, no 2-dimension unbinned KS tests are available with the current tools used in CMS. The procedure taken was, then, to bin the 2D distribution with the analysis binning (40 bins in $M(jj)$ and 60 bins in $M(\gamma\gamma)$), making sure that the number of bins is much larger than the expected number of events (2400 bins is the case). For the blinding procedure, we set the bins of the 2D histograms to 0 in the blinding region ($120 < M(\gamma\gamma) < 130$ GeV). The requirement of the KS goodness of fit test is that the KS probability is $\gg 0.05$, which is achieved for all the categories and signal regions (all KS probabilities larger than 0.45).

5.8.2.3 Correlation Studies

Assuming that the overall 2D shape can be modeled by a 2D second order polynomial, the most general function can be constructed as:

$$f(x, y) = \sum_{i=0}^{i=2} \sum_{k=0}^{k=2} c_{ik} x^i y^k, \quad (5.8)$$

where, in our case, $x = M(\gamma\gamma)$ and $y = M(jj)$ or vice-versa. However, in our modeling, we assume $M(\gamma\gamma)$ and $M(jj)$ to be independent, therefore, our choice of

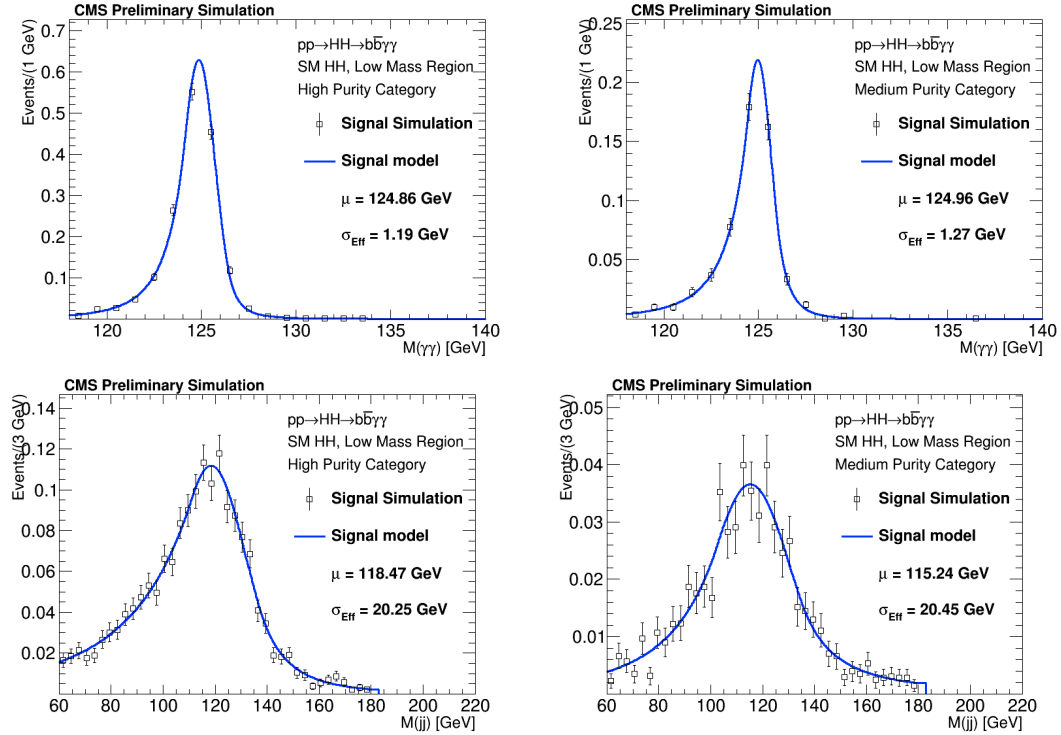


Figure 5.42: Signal fits for the SM HH non-resonant sample after full analysis selection, in categories 0 and 1, for low mass category.

model takes the form of:

$$g(x, y) = \left(\sum_{i=0}^{i=2} a_i x^i \right) \left(\sum_{k=0}^{k=2} a_k y^k \right). \quad (5.9)$$

While the first equation has 9 degrees of freedom, the second only has 6. Therefore, by assuming our two parameters of interest to be independent, we lose three degrees of freedom in our model PDF. To study our sensitivity to these missing degrees of

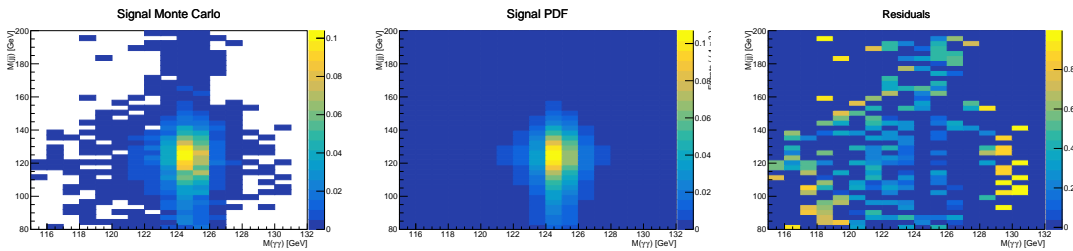


Figure 5.43: 2D distributions of the signal MC (left), fitted PDF model (center) and 2D residuals (right) for the High Mass-High Purity Category non-resonant selection.

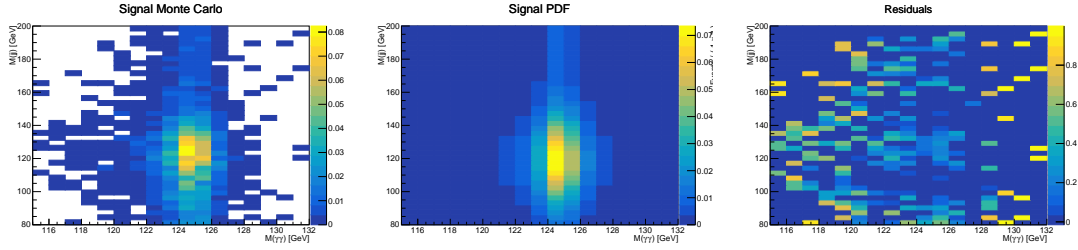


Figure 5.44: 2D distributions of the signal MC (left), fitted PDF model (center) and 2D residuals (right) for the High Mass-Medium Purity Category non-resonant selection.

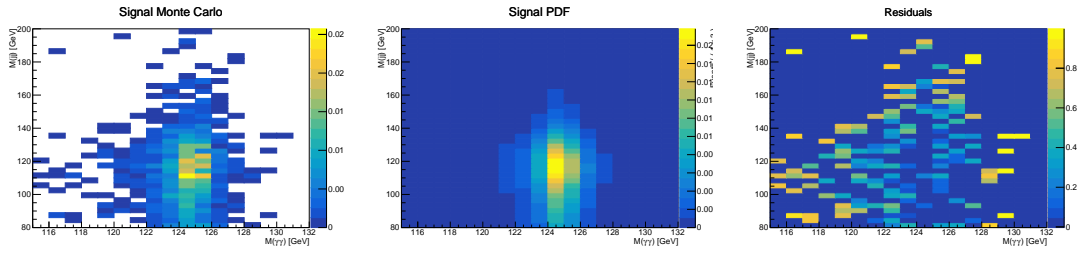


Figure 5.45: 2D distributions of the signal MC (left), fitted PDF model (center) and 2D residuals (right) for the Low Mass-High Purity Category non-resonant selection.

freedom, we construct a new PDF adding back three new parameters, namely:

$$g_{corr}(x, y) = \left(\sum_{i=0}^{i=2} a_i x^i \right) \left(\sum_{k=0}^{k=2} a_k y^k \right) + \alpha \cdot M(\gamma\gamma) \cdot M(jj) + \beta \cdot M(\gamma\gamma)^2 \cdot M(jj) + \omega \cdot M(\gamma\gamma) \cdot M(jj)^2. \quad (5.10)$$

We perform two tests with this PDF:

- We generate Asimov datasets with $g_{corr}(x, y)$ for varying (α, β, ω) and then fit it with $g(x, y)$. Then we check the residuals comparing $g_{corr}(x, y)$ and $g(x, y)$ assuming different normalizations (i.e., different number of expected background events).

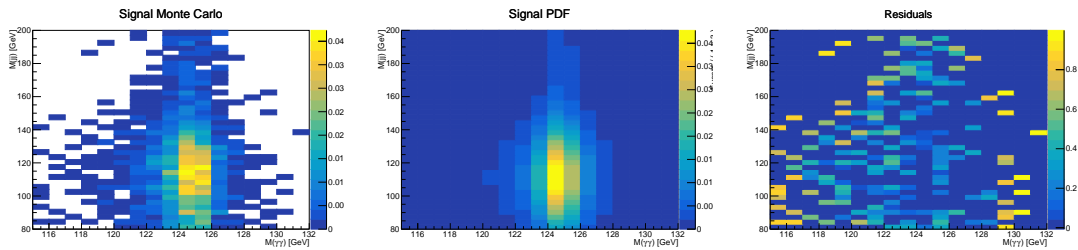


Figure 5.46: 2D distributions of the signal MC (left), fitted PDF model (center) and 2D residuals (right) for the Low Mass-Medium Purity Category non-resonant selection.

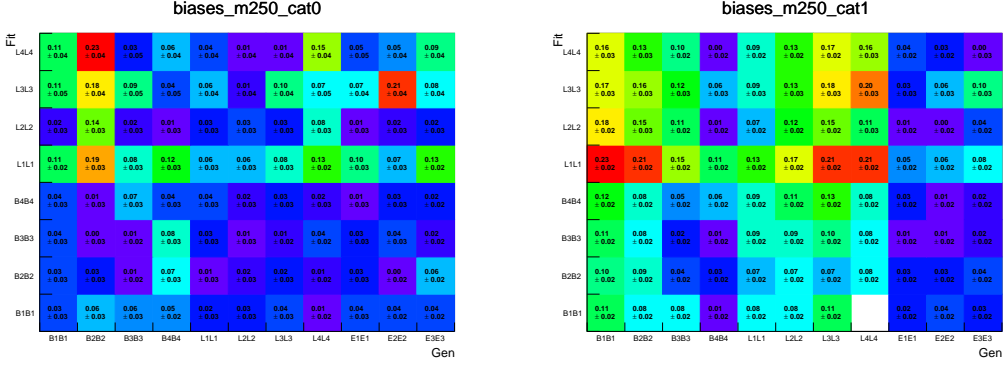


Figure 5.47: Signal fits for the SM HH non-resonant sample after full analysis selection, in categories 0 and 1, for high mass category.

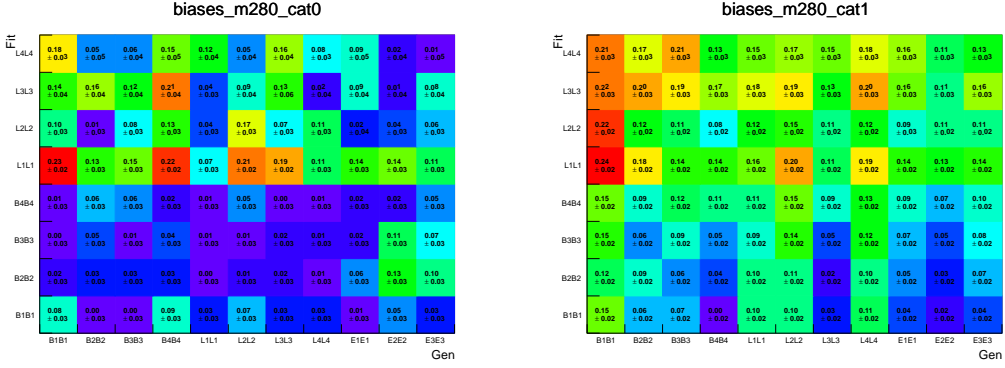


Figure 5.48: Signal fits for the SM HH non-resonant sample after full analysis selection, in categories 0 and 1, for high mass category.

- We generate toy datasets with $g_{corr}(x, y)$ for varying (α, β, ω) , with different values for the expected number of background events, with injected signal. Then we measure back the signal strength by using $g(x, y)$ and check the bias ($B = (\mu_{measured} - \mu_{true})/\sigma_\mu$)

In Figure 5.51, the 2D distributions of $g_{corr}(x, y)$ for different values of α , where the change in correlation between x and y can be seen. In Figure 5.52, the 2D distributions of $g(x, y)$ fitted to the Asimov datasets produced with $g_{corr}(x, y)$ with different values of α , where the change in correlation between x and y can be also be seen, albeit different from $g_{corr}(x, y)$. Therefore, we need to measure how sensitive we are to that difference. The first check is to calculate the 2D residuals, as was done for the signal correlation tests, between these two hypotheses, for different background normalizations. The residuals with the background normalized to 200 events can be seen in Figure 5.53, and for 100000 events in Figure 5.54. While very little statistically significant deviation is seen for 200 background events, structures do start to appear

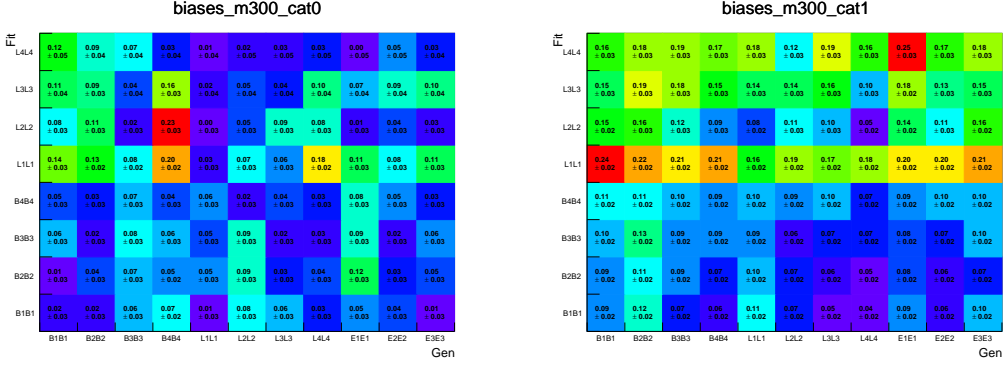


Figure 5.49: Signal fits for the SM HH non-resonant sample after full analysis selection, in categories 0 and 1, for high mass category.

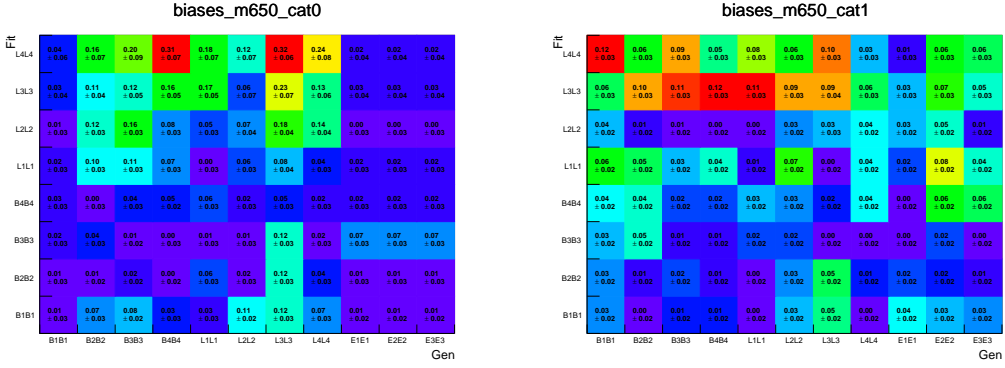


Figure 5.50: Signal fits for the SM HH non-resonant sample after full analysis selection, in categories 0 and 1, for high mass category.

with 100k background events, which is an expected behavior. This test was further performed with 10, 100, 500, 1000, 5000 background events, with conclusions similar to the 200 case. The test was also performed with varying β and ω with similar conclusions.

For the second test, instead of generating Asimov datasets, we generate toy MC for the different normalizations and (α, β, ω) hypotheses. We then show the bias measurement for these different cases, in the hypothesis of varying α , in Figure 5.55. Since no bias larger than 14% is seen, we don't include any systematics on the signal strength due to possible background correlations that are not modeled by our choice of PDF.

5.8.3 Single Higgs Background Modeling

Apart from the smoothly-falling background expected, depending on the integrated luminosity with which it is performed, the non-resonant analysis is also sensitive to

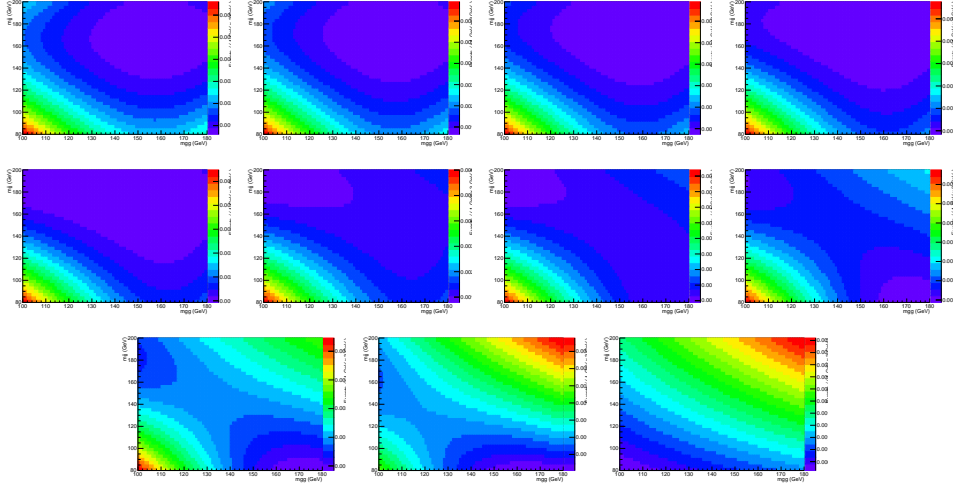


Figure 5.51: 2D distributions of $g_{corr}(x, y)$ with α from 0 to 1, from top to bottom, left to right.

the SM single Higgs production background. In the resonant case, the mass window requirement reduces the single Higgs contributions to negligible levels, and therefore is not considered.

The SM single Higgs background consists on the Higgs resonance in $M(\gamma\gamma)$ and a $M(jj)$ shape that depends on the production mechanism. For single Higgs produced via gluon fusion and vector boson fusion, the two extra jets will constitute a smoothly falling background, therefore, we model this contribution in the 2D $M(\gamma\gamma) : M(jj)$ plane with a product of a double sided Crystal-Ball (similar to our signal model) and a second order Bernstein. For single Higgs produced in association with top quarks, bottom quarks and a vector boson, we are also able to model $M(jj)$ with a double sided Crystal-Ball, given the kinematic turn on present in the first two cases, and the $V \rightarrow jj$ resonance in the latter. The Higgs model fits are shown in Figures 5.56, 5.57, 5.58, 5.59 and 5.60. The cross sections used for the SM single Higgs estimations are listed in table 5.5, along with their efficiencies in the four different non-resonant analysis categories.

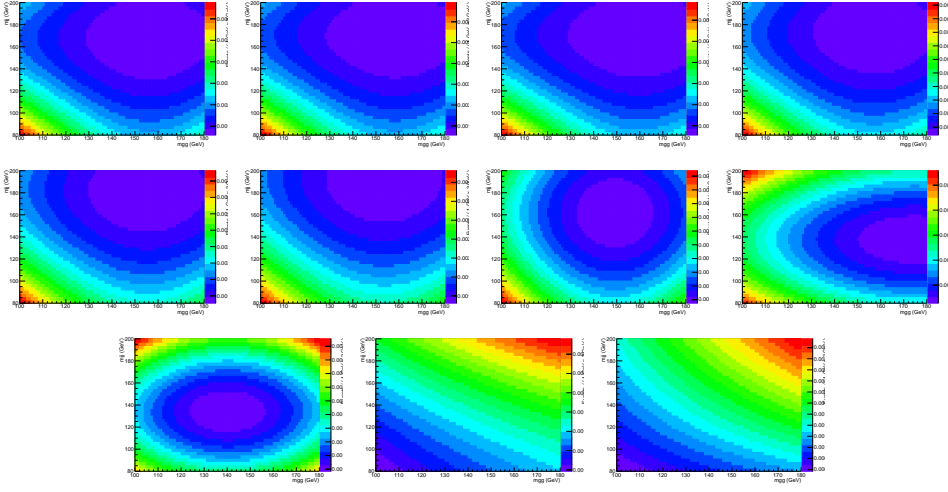


Figure 5.52: 2D distributions of $g(x, y)$ fitted to the Asimov datasets produced with $g_{corr}(x, y)$ with α from 0 to 1, from top to bottom, left to right.

	Cross section (pb)	HM-HPC (%)	HM-MPC (%)	LM-HPC (%)	LM-MPC (%)
ggH	44.14	0.029 ± 0.0017	0.148 ± 0.0038	0.033 ± 0.0018	0.151 ± 0.0039
VBF	3.7820	0.038 ± 0.001	0.239 ± 0.0025	0.048 ± 0.0011	0.242 ± 0.0025
VH	2.257	0.271 ± 0.0038	0.748 ± 0.0063	0.367 ± 0.0044	0.962 ± 0.0071
$b\bar{b}H$	0.488	0.0297 ± 0.0035	0.262 ± 0.010	1.02 ± 0.020	2.59 ± 0.032
$t\bar{t}H$	0.5071	3.41 ± 0.027	3.69 ± 0.029	8.38 ± 0.042	8.17 ± 0.042

Table 5.5: Standard Model single Higgs cross sections at 13 TeV with their respective selection efficiencies for the four different non-resonant analysis categories: High Mass-High Purity, High Mass-Medium Purity, Low Mass-High Purity and Low Mass-Medium Purity categories.

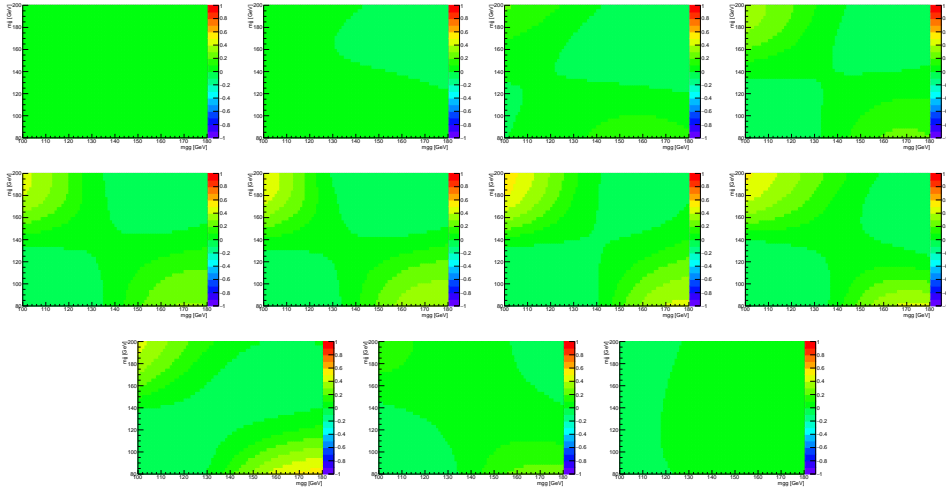


Figure 5.53: 2D residuals comparing distributions of $g(x, y)$ fitted to the Asimov datasets produced with $g_{corr}(x, y)$ with α from 0 to 1 and the dataset , from top to bottom, left to right. The background normalization is 200 events.

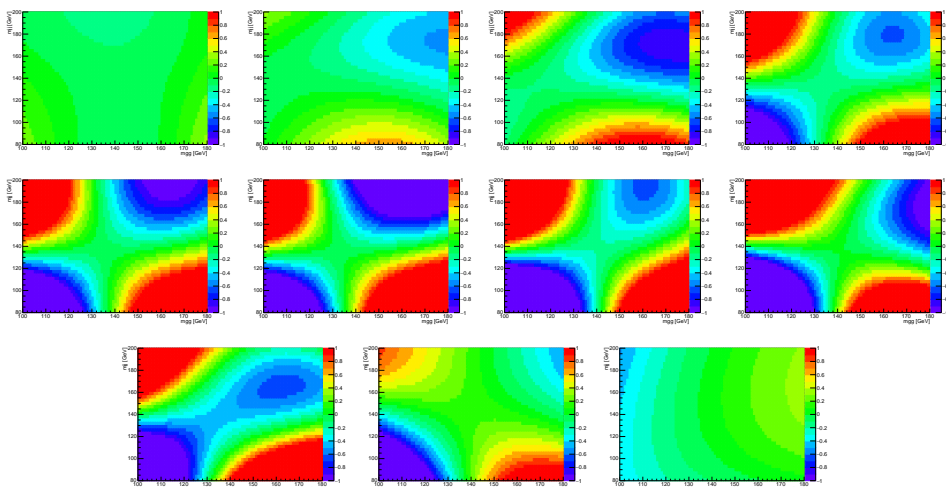


Figure 5.54: 2D residuals comparing distributions of $g(x, y)$ fitted to the Asimov datasets produced with $g_{corr}(x, y)$ with α from 0 to 1 and the dataset , from top to bottom, left to right. The background normalization is 100k events.

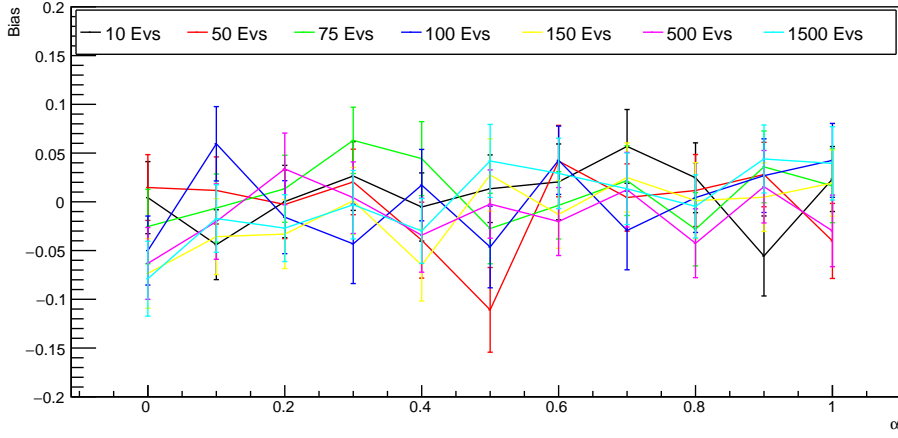


Figure 5.55: Relative bias on measuring the signal with $g(x, y)$ on toys created with $g_{corr}(x, y)$ with α from 0 to 1, for different background normalization hypotheses.

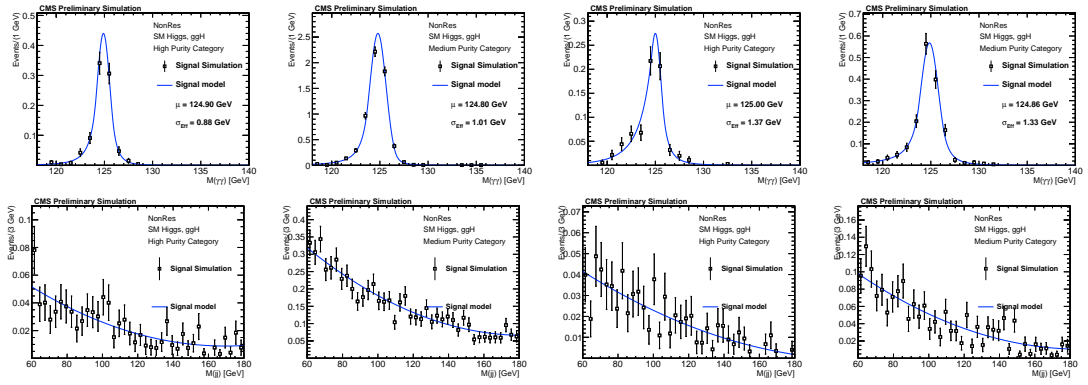


Figure 5.56: Higgs model fit to Higgs Monte Carlo (ggH).

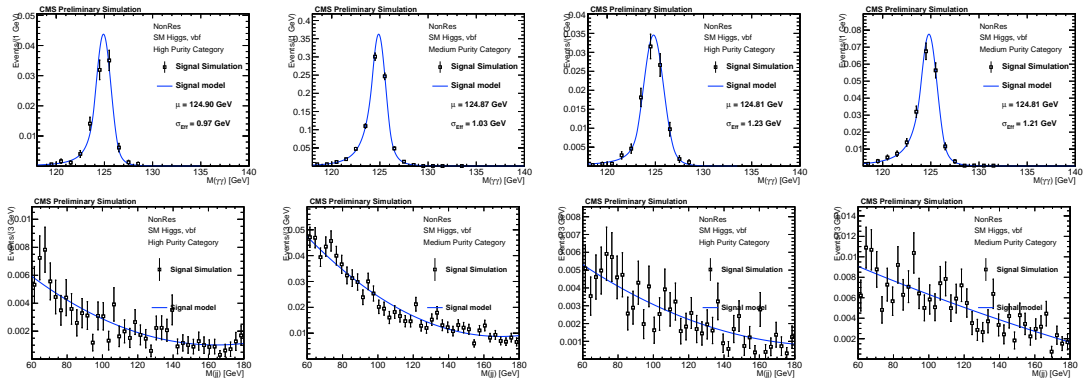


Figure 5.57: Higgs model fit to Higgs Monte Carlo (VBF).

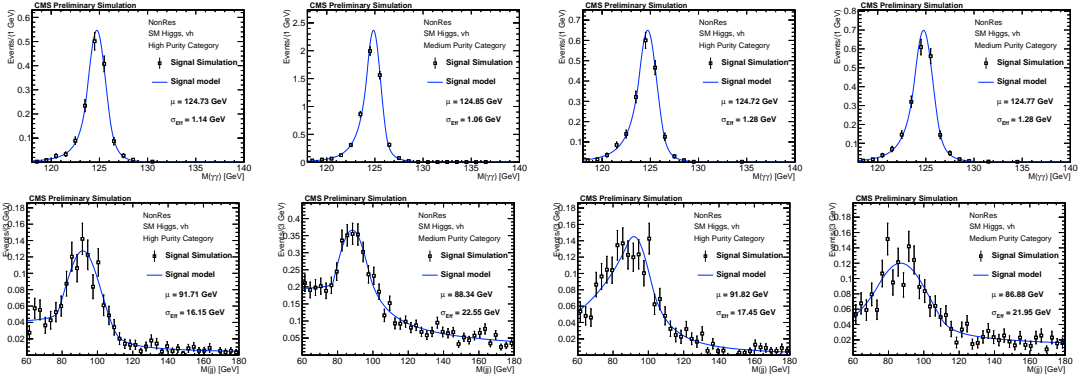


Figure 5.58: Higgs model fit to Higgs Monte Carlo (VH).

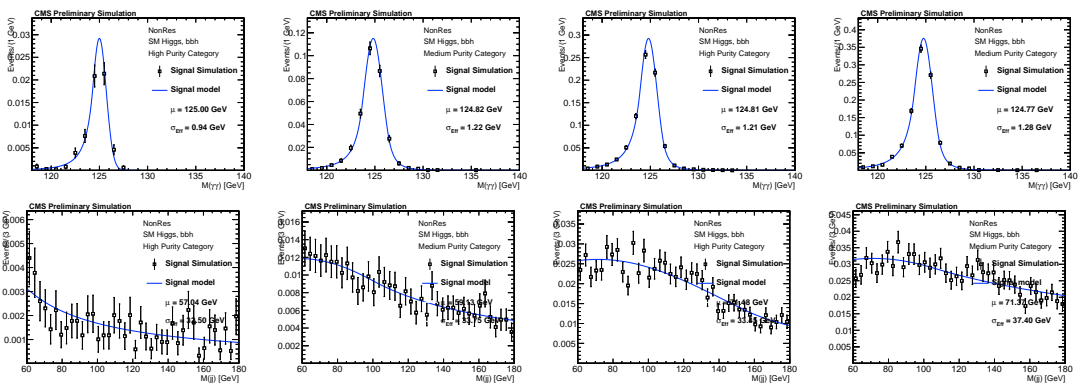


Figure 5.59: Higgs model fit to Higgs Monte Carlo (bbH).

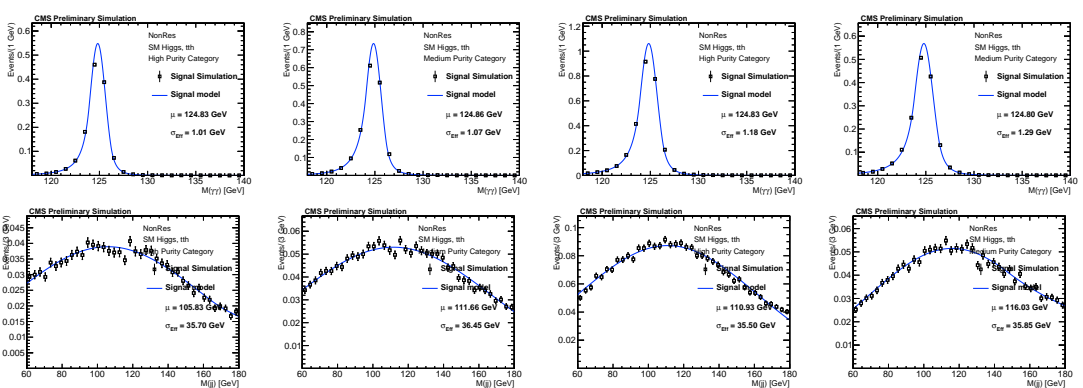


Figure 5.60: Higgs model fit to Higgs Monte Carlo (ttH).

5.9 Systematics

The expected number of signal events in this analysis is projected with Monte Carlo simulation. Possible differences between data reconstruction and Monte Carlo reconstruction are usually corrected with data/Monte Carlo scale factors. In this analysis, the systematics related to those differences come in two possible categories: normalization uncertainties and shape uncertainties. The normalization systematics are related to the uncertainty in the expected number of signal events. This is due to different efficiencies of the analysis selections in data and Monte Carlo reconstructions. Shape systematics are important in this analysis because the signal shapes enter the signal extraction procedure in the parametric fits. Therefore, uncertainties in the shape of $M(\gamma\gamma)$ and $M(jj)$ distributions must be included as systematics.

Both normalization and shape uncertainties come from photons and jets. Since the photons in this analysis are selected with the same selection criteria as the SM $H \rightarrow \gamma\gamma$ analysis, we take the photon related systematics from that. This includes the photon energy scale (PES) and photon energy resolution (PER). These two uncertainties are translated into two shape systematics ($\Delta M(\gamma\gamma)/M(\gamma\gamma)$ and $\Delta\sigma_{M(\gamma\gamma)}/\sigma_{M(\gamma\gamma)}$), and into the photon selection selection acceptance uncertainty (which includes the trigger pre-selection requirements). The PES has to cover as well effects of linearity in the energy scale for high E_T . For this, $\Delta M(\gamma\gamma)/M(\gamma\gamma)$ is kept at 0.7% (cite diphoton high mass moriond PAS) for 2015 and 0.05% for 2016 (cite Hgg presentation on Higgs recap).

For jets, the jet energy scale (JES) and jet energy resolution (JER) are important ingredients in the list of systematics. As for photons, they enter in the analysis in two shape systematics ($\Delta M(jj)/M(jj)$ and $\Delta\sigma_{M(jj)}/\sigma_{M(jj)}$), and in the jet selection acceptance uncertainty (related to the jet kinematic requirements). An extra jet related systematic is related to the b-tagging requirements. The analysis has defined four b-tagging regions in total (two for resonant and two for non-resonant); for each one, the uncertainty of the b-tagging efficiency must be taken into account.

An extra set of normalization systematics are needed because of the mass window requirement in the resonant analysis. This systematic is related to the change in signal efficiency after variations of PES/PER/JES/JER.

A systematic due to the uncertainty in the integrated luminosity measurement in CMS is included.

No theory systematics are applied to our BSM signals.

The values of those quantities are shown in table 5.6 for 2015 data and will be updated with 2016 values.

Sources of Systematical Uncertainties	Type	Value
General uncertainties		
Integrated luminosity	Normalization	2.7%
Photon related uncertainties		
Photon energy scale ($\frac{\Delta M(\gamma\gamma)}{M(\gamma\gamma)}$)	Shape	1.0%
Photon energy resolution ($\frac{\Delta \sigma_{\gamma\gamma}}{\sigma_{\gamma\gamma}}$)	Shape	1.0%
Diphoton pre-selection (with trigger uncertainties)	Normalization	2.0%
Photon Identification	Normalization	1.0%
Jet related uncertainties		
Jet energy scale ($\frac{\Delta M(jj)}{M(jj)}$)	Shape	2.0%
Jet energy resolution ($\frac{\Delta \sigma_{jj}}{\sigma_{jj}}$)	Shape	8.0%
Resonant specific uncertainties		
Mass window selection (with jet selection uncertainty)	Normalization	5.0%
b tagging efficiency (Low Mass, high purity)	Normalization	2.5%
b tagging efficiency (Low Mass, medium purity)	Normalization	1.0%
b tagging efficiency (High Mass)	Normalization	1.0%
Nonresonant specific uncertainties		
Jet Selection plus $\tilde{M}_X > 350$ GeV	Normalization	3.0%
b tagging efficiency (high purity)	Normalization	4.5%
b tagging efficiency (medium purity)	Normalization	1.0%

Table 5.6: Summary of systematic uncertainties. The uncertainty in the b tagging efficiency is anticorrelated between the b tag categories.

5.9.1 Signal shape smearings

One important ingredient when applying the analysis systematics is the smearing of the signal shapes. After the signal model is fitted to the signal simulation, all PDF parameters are fixed. Following, the signal mean and width are then multiplied by smearing factors related to scale and resolution uncertainties, respectively. While this is clearly un-problematic for the mean, since it merely causes a scaling of the x axis, this might not be the case for the resolution smearing. In the latter case, the tail parameters of the signal modeling can be affected by the smearing and not correspond to the frozen parameters from the pre-smearing fit. To test this, we fit the smeared MC (MC with photon and jet energy resolution smearing uncertainty values applied) with the signal PDF with the tails fixed to their values from the un-smeared MC (MC with central values of smearings) and we compare with the smeared MC fit with

the signal PDF without fixing the tail parameters - these different fits are shown in Figures 5.61 and 5.62. We have also compared the 2D residuals (as defined in the Signal Model section) of the fixed tails PDF vs the smeared MC with the floating tails PDF vs the smeared MC, shown in Figure 5.63. Additionally, we compare the fixed and floating fit shapes in Figure 5.64. Since no issue has been seen, we continue using the procedure described in the previous section for applying the signal smearing.

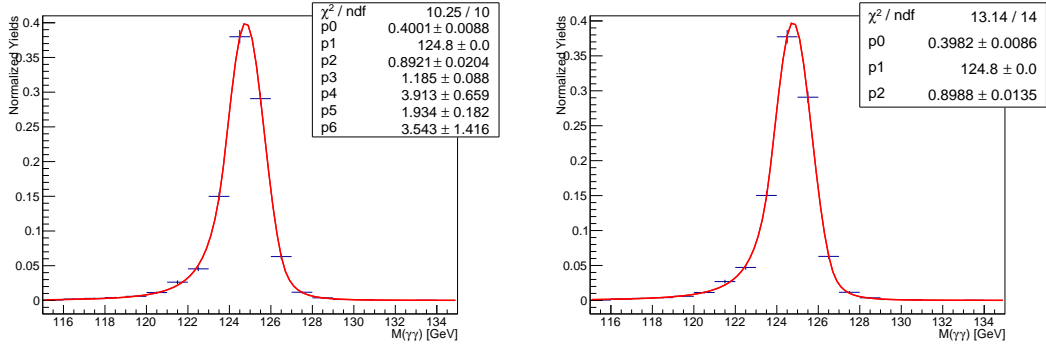


Figure 5.61: Signal fits for the High Mass Medium purity categories, in the un-smeared MC with floating tails (left) and on the smeared MC with fixed tails (right). The tail parameters on the right are fixed to their values on the left.

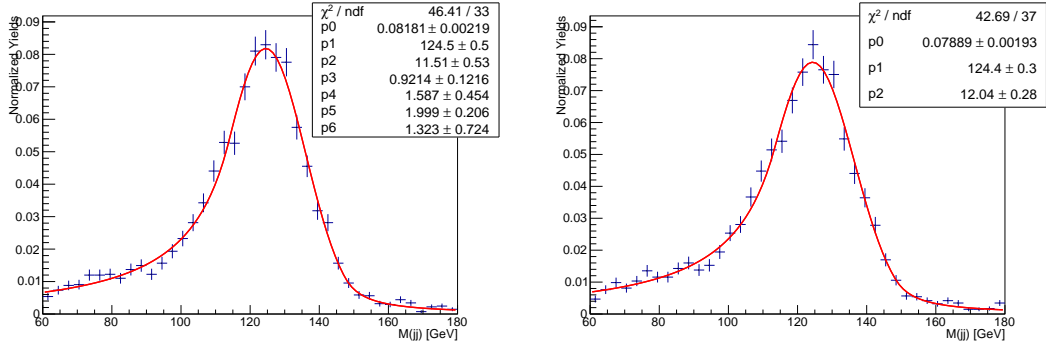


Figure 5.62: Signal fits for the High Mass Medium Purity category, in the un-smeared MC with floating tails (left) and on the smeared MC with fixed tails (right). The tail parameters on the right are fixed to their values on the left.

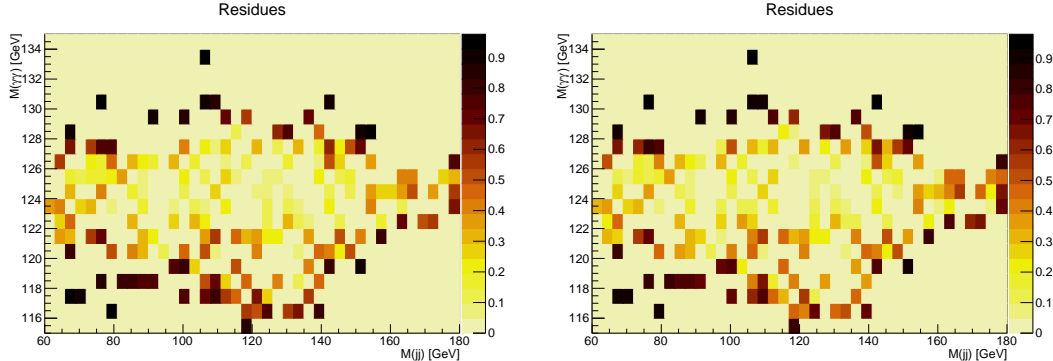


Figure 5.63: Residuais comparing the floating signal PDF fit to the smeared MC (left) and the fixed tails PDF fit to the smeared MC (right) in the High Mass Medium Purity category.

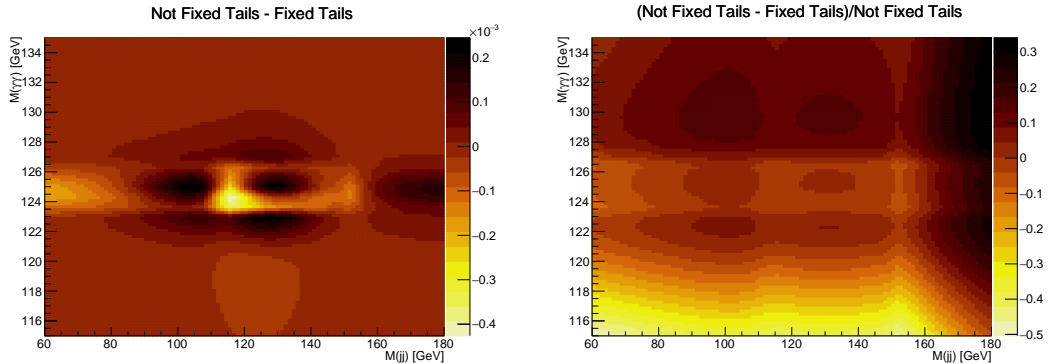


Figure 5.64: Comparison between fixed and floating PDF shapes when fitting the smeared MC.

5.10 Results

The limits shown in this section are obtained with the Higgs Combination tool, with the Asymptotic method. It has been noticed in the analysis that the central expected values can change by up to 15% when running the full CLs method. The full CLs method, however, takes considerably longer to run, therefore, the full CLs limits did not get ready for the freezing deadline.

Figure 5.65 shows the results on spin-0 resonances. Figure 5.66 shows the results on spin-2 resonances. Figures 5.67 (in fb) and 5.68 (normalized to SM cross section) show the SM-like non-resonant limit and its breakdown in the different analysis categories: LM (Low Mass), HM (High Mass), MPC (Medium Purity Category), and HPC (High Purity Category).

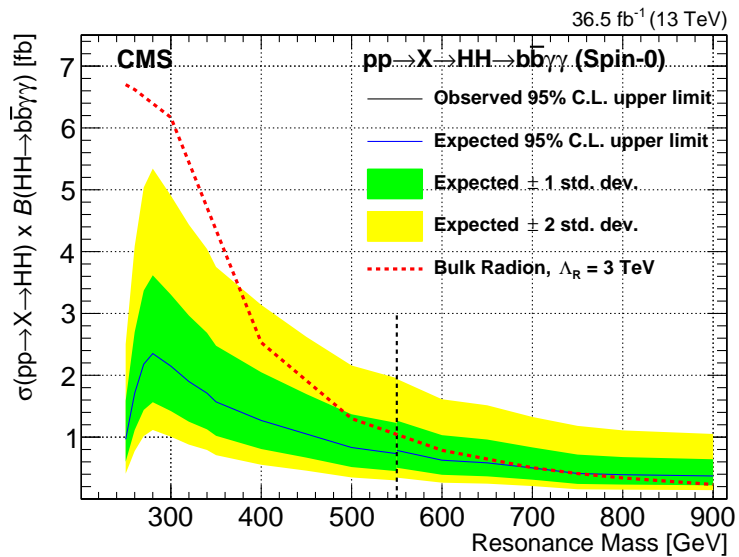


Figure 5.65: Limits on spin-0 resonances.

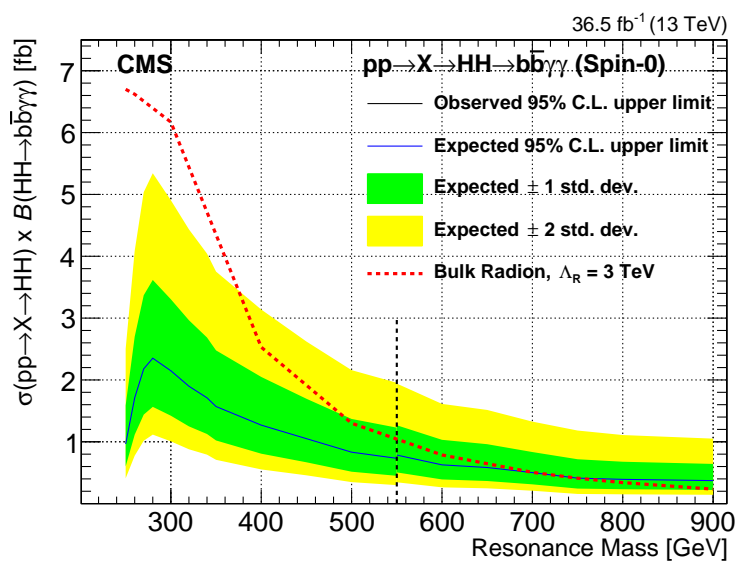


Figure 5.66: Limits on spin-2 resonances.

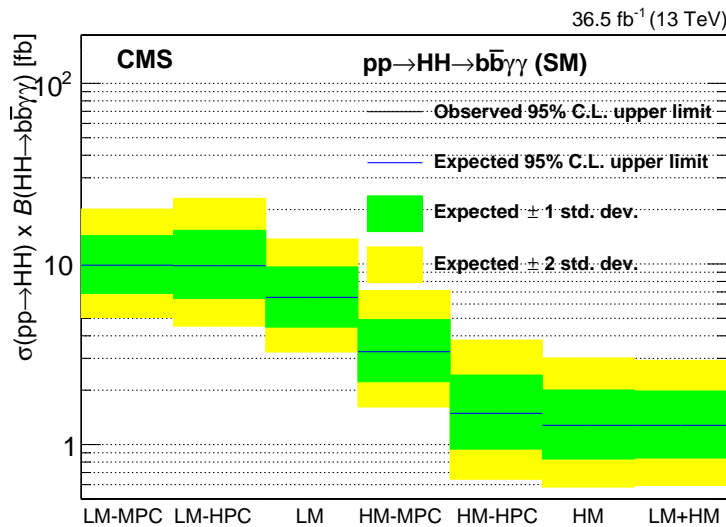


Figure 5.67: SM-like non-resonant limits.

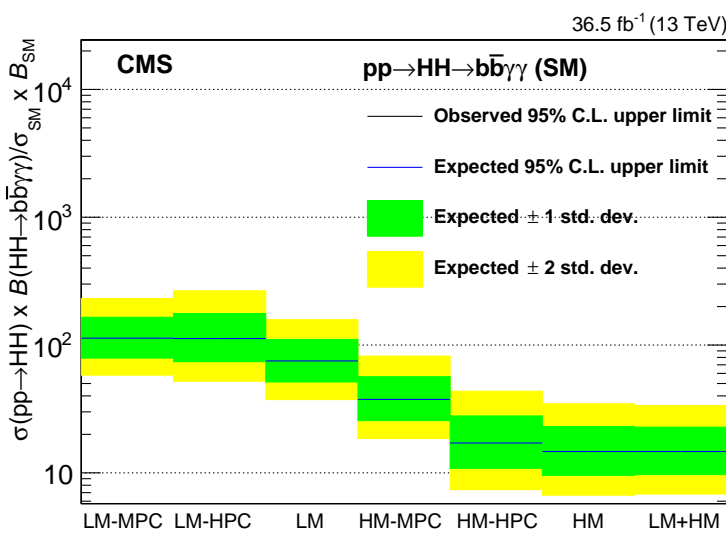


Figure 5.68: SM-like non-resonant limits normalized to SM cross section.

5.11 BSM Nonresonant Results

In addition to determination of the limit on the SM process, we are able to provide the results for BSM couplings as described 5.2.2. For the non-resonant signal samples corresponding to combinations of five anomalous couplings (κ_λ , κ_t , c_2 , c_{2g} , and c_g) listed in Table 5.1 (these are also called "nodes"), the limits are shown on Fig. 5.69. The limits for the benchmarks listed in Table 5.2 and described in Sec. 5.2.2 are shown in Fig. 5.70. Figure 5.71 shows the "lambda-scan" - the upper limits for the assumption of changing κ_λ , while keeping other couplings fixed to their SM values. Figure 5.72 shows a scan over $\lambda - \kappa_t$ parameter space (this plot is for ICHEP dataset, NEEDS to be updated for 2016 data).

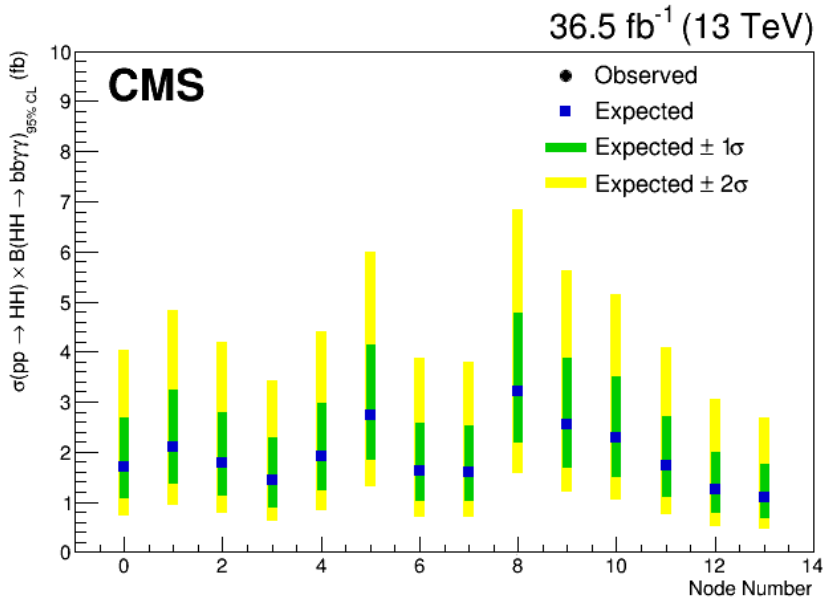


Figure 5.69: Limits for Nodes specified in Table 5.1.

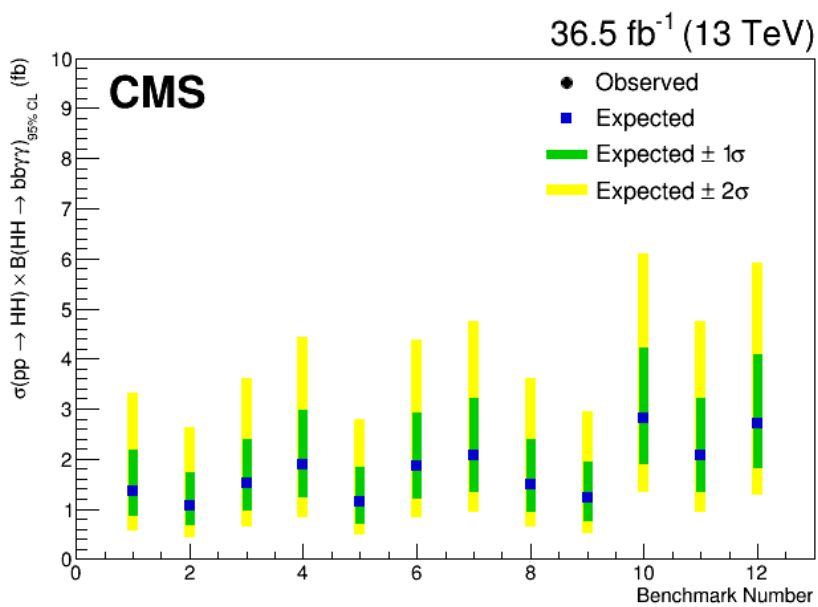


Figure 5.70: Limits for Benchmarks described in Sec. 5.2.2 in Table 5.2.

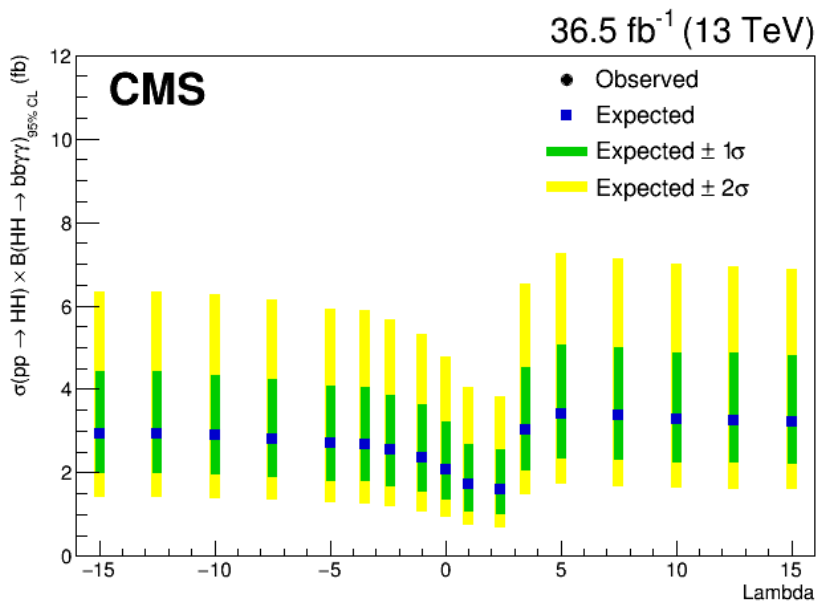


Figure 5.71: Upper limits for the BSM models with varying κ_λ parameter, while others fixed to their SM values.

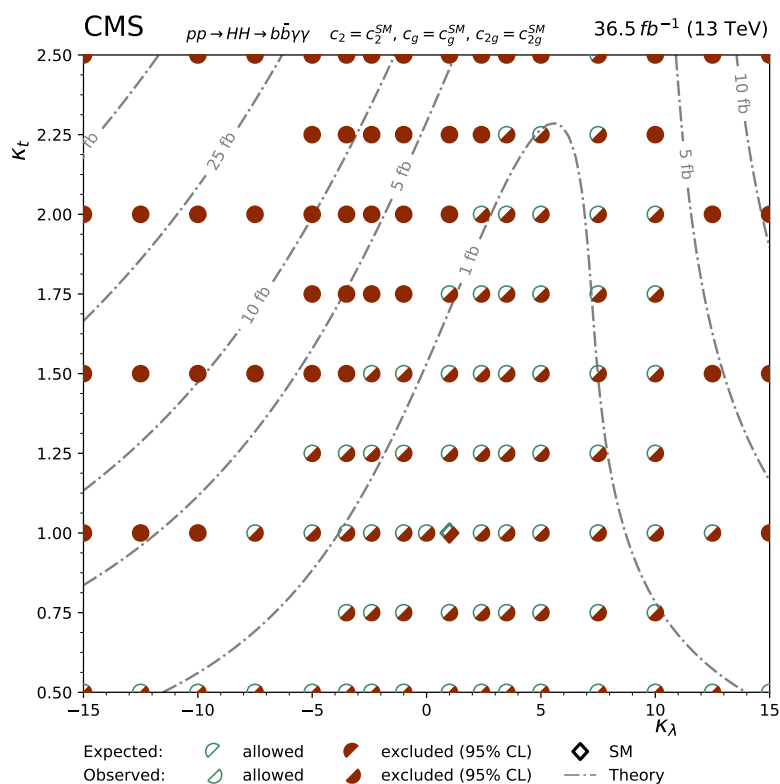


Figure 5.72: Upper limits for the BSM models with varying $\kappa_\lambda - \kappa_t$ parameters, while other parameters are fixed to their SM values.

5.12 Summary

Chapter 6

Conclusions

Lorem ipsum dolor sit amet, consectetur adipiscing elit, sed do eiusmod tempor incididunt ut labore et dolore magna aliqua. Ut enim ad minim veniam, quis nostrud exercitation ullamco laboris nisi ut aliquip ex ea commodo consequat. Duis aute irure dolor in reprehenderit in voluptate velit esse cillum dolore eu fugiat nulla pariatur. Excepteur sint occaecat cupidatat non proident, sunt in culpa qui officia deserunt mollit anim id est laborum.

Einstein's paper: [?]